Jet Transverse Energy Shape in $p\bar{p}$ Collisions at $\sqrt{s}$=1.8 TeV

A Thesis

Submitted to the Faculty

of

Purdue University

by

Braden K. Abbott

In Partial Fulfillment of the

Requirements for the Degree

of

Doctor of Philosophy

December 1994

To Kim, who showed me the true meaning of strength and courage.

ACKNOWLEDGEMENTS

In a collaboration the size of DØ it is impossible to thank all of the people who have helped me along the way. I have received invaluable help from many people and their contributions have made this thesis possible. In particular I would like to thank Kathy Streets, Jerry Blazey, and Rich Astur, along with the entire QCD group, for putting up with and answering my questions. I would like to thank Amber for patiently teaching me DØ software. A thanks to Bob Kehoe and the Notre Dame contingent for many discussions on a wide variety of topics. I would like to thank my advisor Dave Koltick for his support. Many thanks to Walter Giele for helping me with QCD theory. And a thank you to the entire DØ collaboration for their help and patience.

TABLE OF CONTENTS

Page

LIST OF FIGURES vi

LIST OF TABLES xii

ABSTRACT xv

1. Introduction 1

    1.1 History 1
    1.2 The Standard Model 3
    1.3 Jets 8
    1.4 Motivation 10

2. QCD Theory 15

    2.1 Lagrangian of QCD 15
    2.2 The running coupling constant 16
    2.3 Leading order and next-to-leading order calculations 20
    2.4 Parton Distribution Functions 21

3. Experimental Apparatus 24

    3.1 Fermilab 24
    3.2 The DØ Detector 27
    3.3 Tracking Chambers 29
        3.3.1 Vertex Chamber 29
        3.3.2 Central Drift Chamber 31
        3.3.3 Forward Drift Chambers 32
    3.4 Calorimeter 32
        3.4.1 Central Calorimeter 38
        3.4.2 Central Electromagnetic Calorimeter 38
        3.4.3 Central Hadronic Calorimeter 40
        3.4.4 End Calorimeters 41
        3.4.5 End Calorimeter Electromagnetic Layer 42
        3.4.6 End Calorimeter Inner Hadronic Layer 42
        3.4.7 End Calorimeter Middle Hadronic Layer 42
        3.4.8 End Calorimeter Outer Hadronic Layer 43
    3.5 Triggers and Data Acquisition 43

Page

3.5.1 Level 0 43
3.5.2 Level 1 44
3.5.3 Level 2 45

4. Data Analysis 47

4.1 Experimental Definition of Jets 47
4.2 Experimental Measurement of Jet Shape 49
4.3 Triggers 50
4.4 Data Sample and Cuts 51
4.4.1 Trigger Cuts 52
4.4.2 Vertex and Missing E_T cut 54
4.4.3 Jet Quality Cuts 55
4.4.4 η cuts 56
4.5 Corrections to the Data 58
4.6 Systematic Errors 69
4.6.1 Out of Cone Effects 71
4.7 Effects of the Calorimeter 72

5. Experimental Results and Comparisons to Theoretical Predictions 84

5.1 Experimentally Measured Jet Shapes 85
5.2 Comparison to Theoretical Predictions 89

6. Conclusions 106

BIBLIOGRAPHY 109

APPENDICES

Appendix A: Correction Factors 111
Appendix B: Alternative Definitions of the Jet Shape 115
Appendix C: Merged and Split Jets 124
Appendix D: Leading and Non-Leading Jets 131

VITA 138

LIST OF FIGURES

Figure Page

1.1 A comparison between the experimentally measured jet shape and a theoretical prediction using three different values of μ for centrally located jets. 14

1.2 A comparison between the experimentally measured jet shape and a theoretical prediction using three different values of μ for jets located in the forward region. 14

2.1 Schematic diagram indicating the renormalization scale dependence on a typical cross section. 19

2.2 Feynman diagrams contributing to lowest order parton-parton scattering. 22

2.3 Feynman diagrams contributing to next-to-leading order parton-parton scattering. 23

3.1 A schematic view of Fermilab. 24

3.2 The DØ Detector. 28

3.3 Tracking Volume 30

3.4 Calorimeter 33

3.5 Section of calorimeter module showing absorber plates, liquid argon and signal boards. (not to scale) 34

3.6 Side view of the DØ calorimeter. Calorimeter cells are shown as alternate colors of grey and white within a projective tower. Superimposed above the calorimeter is the η position of each tower assuming a nominal vertex of z=0. 34

3.7 a) Pulse height spectrum of 25 GeV electrons. b) Pulse height spectrum of 25 GeV hadrons/muons. 36

Figure Page

3.8 Calorimeter response to pions and electrons for 2 through 150 GeV/c. 40

3.9 Schematic of the trigger system. 46

4.1 The transverse energy contained within the cells of a jet divided by the jet E_T for events within $\pm$ 30 cm of the detector's center. 51

4.2 The difference $\rho(r)_{Jet\ Low} - \rho(r)_{Jet\ Medium}$ 54

4.3 The missing E_T in an event divided the leading jet E_T. The shaded region is due to events with hot cells. 55

4.4 Comparing η and $\eta_{detector}$ for centrally located jets. 57

4.5 Comparing η and $\eta_{detector}$ for jets located in the forward region. . . . 58

4.6 The difference in jet shape when cutting on $\eta_{detector}$ and η. 59

4.7 A, B and C represent the three different response curves studied within Herwig and the circles are the measured calorimeter response from test beam. 62

4.8 The effects on the jet shape for the three different response curves simulated in Herwig. The points are separated along the x-axis to allow the response effects to be seen. 63

4.9 Energy distribution of calorimeter cells for a sample of minimum bias events. The 2σ region has been set to zero in hardware before being readout. 65

4.10 The fraction of cells within a cone radius $R_{\eta\phi} = 1.0$ with non-zero energy outside the hardware suppression value for a sample of minimum bias data vs η. 68

4.11 The fraction of cells within a cone radius $R_{\eta\phi} = 1.0$ with non-zero energy outside the hardware suppression value for jets between 105 and 140 GeV vs η. 68

4.12 The fraction of cells with non-zero energy outside the hardware suppression value for jets between 105 and 140 GeV vs subcone radius. . 69

Figure Page

4.13 The transverse energy density, $\frac{dE_T}{d\eta d\phi}$, for central jets with transverse energy between 45 and 70 GeV. 72

4.14 The transverse energy density, $\frac{dE_T}{d\eta d\phi}$, for forward jets with transverse energy between 45 and 70 GeV. 73

4.15 The average energy of particles within each subcone vs subcone radius. 73

4.16 Comparing data to three different Monte Carlo simulations in the central region for jets with transverse energy between 45 and 70 GeV. . 77

4.17 Comparing data to three different Monte Carlo simulations in the central region for jets with transverse energy between 70 and 105 GeV. . 77

4.18 Comparing data to three different Monte Carlo simulations in the central region for jets with transverse energy between 105 and 140 GeV. 78

4.19 Comparing data to three different Monte Carlo simulations in the central region for jets with transverse energy greater than 300 GeV. . . 78

4.20 Comparing data to two different Monte Carlo simulations in the forward region for jets with transverse energy between 45 and 70 GeV. 79

4.21 Comparing data to two different Monte Carlo simulations in the forward region for jets with transverse energy between 70 and 105 GeV. 79

4.22 The particle level jet shape before and after calorimeter biases for central jets. 80

4.23 The particle level jet shape before and after calorimeter biases for forward jets. 81

4.24 Difference in additive correction factors between modelling the calorimeter using the full plate level geometry and the mixture level geometry in GEANT. 82

5.1 The jet shape in the central region for different E_T regions. 86

5.2 The jet shape in the central region for different merge/split classifications. 87

5.3 The jet shape in the central region for leading jets and non-leading jets. 88

5.4 The jet shape at DØ and CDF. 90

Figure Page

5.5 Comparing the jet shape in the central region and the forward region after the effects of the calorimeter have been removed for jets with transverse energy between 45 and 70 GeV. 91

5.6 Comparing the jet shape in the central region and the forward region after the effects of the calorimeter have been removed for jets with transverse energy between 70 and 105 GeV. 92

5.7 Comparing data to NLO theory in the central region for jets with transverse energy between 45 and 70 GeV. 96

5.8 Comparing data to NLO theory in the central region for jets with transverse energy between 70 and 105 GeV. 97

5.9 Comparing data to NLO theory in the central region for jets with transverse energy between 105 and 140 GeV. 98

5.10 Comparing data to NLO theory in the central region for jets with transverse energy greater than 140 GeV. 99

5.11 Comparing data to NLO theory in the forward region for jets with transverse energy between 45 and 70 GeV. 100

5.12 Comparing data to NLO theory in the forward region for jets with transverse energy between 70 and 105 GeV. 101

5.13 Effects on $\rho(r)$ due to changing the algorithm used to calculate η_{jet} and ϕ_{jet} in Jetrad for jets located at $|\eta| < 0.2$. 103

5.14 Effects on $\rho(r)$ due to the algorithm used to calculate η_{jet} and ϕ_{jet} in Jetrad for jets located at $2.5 < |\eta| < 3.0$. 103

5.15 Effects on $\rho(r)$ due to changing the algorithm used to calculate η_{jet} and ϕ_{jet} in Herwig for jets located at $|\eta| < 0.2$. 105

5.16 Effects on $\rho(r)$ due to changing the algorithm used to calculate η_{jet} and ϕ_{jet} in Herwig for jets located at $2.5 < |\eta| < 3.0$. 105

Appendix
Figure

B.1 The jet shape defined as $\frac{dE_T}{E_T}$ for jets located at $|\eta| < 0.2$. 116

Figure Page

B.2 The jet shape defined as $\frac{dE_T}{E_T}$ for jets located at $2.5 < |\eta| < 3.0$. . . . 116

B.3 The jet shape defined as $\frac{1}{E_T}\frac{dE_T}{d\eta d\phi}$ for jets located at $|\eta| < 0.2$. 117

B.4 The jet shape defined as $\frac{1}{E_T}\frac{dE_T}{d\eta d\phi}$ for jets located at $2.5 < |\eta| < 3.0$. . . 118

B.5 The jet shape defined as $\frac{dE_T}{d\eta d\phi}$ for jets located at $|\eta| < 0.2$ with transverse energy between 45 and 70 GeV. 119

B.6 The jet shape defined as $\frac{dE_T}{d\eta d\phi}$ for jets located at $|\eta| < 0.2$ with transverse energy between 70 and 105 GeV. 120

B.7 The jet shape defined as $\frac{dE_T}{d\eta d\phi}$ for jets located at $|\eta| < 0.2$ with transverse energy between 105 and 140 GeV. 120

B.8 The jet shape defined as $\frac{dE_T}{d\eta d\phi}$ for jets located at $|\eta| < 0.2$ with transverse energy greater than 140 GeV. 121

B.9 The jet shape defined as $\frac{dE_T}{d\eta d\phi}$ for jets located at $2.5 < |\eta| < 3.0$ with transverse energy between 45 and 70 GeV. 122

B.10 The jet shape defined as $\frac{dE_T}{d\eta d\phi}$ for jets located at $2.5 < |\eta| < 3.0$ with transverse energy between 70 and 105 GeV. 122

C.1 The jet shape for different merge/split parameters for jets with transverse energy between 45 and 70 GeV located at $|\eta| < 0.2$. Errors are statistical only. 125

C.2 The jet shape for different merge/split parameters for jets with transverse energy between 70 and 105 GeV located at $|\eta| < 0.2$. Errors are statistical only. 125

C.3 The jet shape for different merge/split parameters for jets with transverse energy between 105 and 140 GeV located at $|\eta| < 0.2$. Errors are statistical only. 126

C.4 The jet shape for different merge/split parameters for jets with transverse energy greater than 140 located at $|\eta| < 0.2$. Errors are statistical only. 127

Figure Page

C.5 The jet shape for different merge/split parameters for jets with transverse energy between 45 and 70 GeV located at $2.5 < |\eta| < 3.0$. Errors are statistical only. 128

C.6 The jet shape for different merge/split parameters for jets with transverse energy between 70 and 105 GeV located at $2.5 < |\eta| < 3.0$. Errors are statistical only. 129

D.1 The jet shape for leading and non-leading jets for jets located at $\eta < 0.2$ with transverse energy between 45 and 70 GeV. Errors are statistical only. 132

D.2 The jet shape for leading and non-leading jets for jets located at $\eta < 0.2$ with transverse energy between 70 and 105 GeV. Errors are statistical only. 132

D.3 The jet shape for leading and non-leading jets for jets located at $\eta < 0.2$ with transverse energy between 105 and 140 GeV. Errors are statistical only. 133

D.4 The jet shape for leading and non-leading jets for jets located at $\eta < 0.2$ with transverse energy greater than 140 GeV. Errors are statistical only. 134

D.5 The jet shape for leading and non-leading jets for jets located at $2.5 < \eta < 3.0$ with transverse energy between 45 and 70 GeV. Errors are statistical only. 135

D.6 The jet shape for leading and non-leading jets for jets located at $2.5 < \eta < 3.0$ with transverse energy between 70 and 105 GeV. Errors are statistical only. 136

LIST OF TABLES

Table Page

1.1 The six fundamental leptons 3

1.2 The six fundamental quarks 4

1.3 The four fundamental forces 4

1.4 The six carriers of force 4

3.1 Central Calorimeter Characteristics 39

3.2 End Calorimeters Characteristics 41

4.1 Triggers Used in Jet Shape Analysis 52

5.1 Energy Flow values at the particle level for jets located at $|\eta| < 0.2$ . . 93

5.2 Energy Flow values at the particle level for jets located at $2.5 < |\eta| < 3.0$ 93

Appendix
Table

A.1 Additive corrections for jets located at $|\eta| < 0.2$ with transverse energy between 45 and 70 GeV. 111

A.2 Additive corrections for jets located at $|\eta| < 0.2$ with transverse energy between 70 and 105 GeV. 112

A.3 Additive corrections for jets located at $|\eta| < 0.2$ with transverse energy between 105 and 140 GeV. 112

A.4 Additive corrections for jets located at $|\eta| < 0.2$ with transverse energy greater than 140 GeV. 113

A.5 Additive corrections for jets located at $2.5 < |\eta| < 3.0$ with transverse energy between 45 and 70 GeV. 113

Table Page

A.6 Additive corrections for jets located at $2.5 < |\eta| < 3.0$ with transverse energy between 70 and 105 GeV. 114

B.1 The jet shape defined as $\frac{dE_T}{E_T}$ for jets located at $|\eta| < 0.2$. 115

B.2 The jet shape defined as $\frac{dE_T}{E_T}$ for jets located at $2.5 < |\eta| < 3.0$. . . . 117

B.3 The jet shape defined as $\frac{1}{E_T}\frac{dE_T}{d\eta d\phi}$ for jets located at $|\eta| < 0.2$. 118

B.4 The jet shape defined as $\frac{1}{E_T}\frac{dE_T}{d\eta d\phi}$ for jets located at $2.5 < |\eta| < 3.0$. . . 119

B.5 The jet shape defined as $\frac{dE_T}{d\eta d\phi}$ for jets located at $|\eta| < 0.2$. 121

B.6 The jet shape defined as $\frac{dE_T}{d\eta d\phi}$ for jets located at $2.5 < |\eta| < 3.0$. . . . 123

C.1 Energy Flow values for different merge/split parameters for jets with transverse energy between 45 and 70 GeV located at $|\eta| < 0.2$. Errors are statistical only. 124

C.2 Energy Flow values for different merge/split parameters for jets with transverse energy between 70 and 105 GeV located at $|\eta| < 0.2$. Errors are statistical only. 126

C.3 Energy Flow values for different merge/split parameters for jets with transverse energy between 105 and 140 GeV located at $|\eta| < 0.2$. Errors are statistical only. 127

C.4 Energy Flow values for different merge/split parameters for jets with transverse energy greater than 140 GeV located at $|\eta| < 0.2$. Errors are statistical only. 128

C.5 Energy Flow values for different merge/split parameters for jets with transverse energy between 45 and 70 GeV located at $2.5 < |\eta| < 3.0$. Errors are statistical only. 129

C.6 Energy Flow values for different merge/split parameters for jets with transverse energy between 70 and 105 GeV located at $2.5 < |\eta| < 3.0$. Errors are statistical only. 130

Table Page

D.1 The jet shape for leading and non-leading jets for jets located at $\eta < 0.2$ with transverse energy between 45 and 70 GeV. Errors are statistical only. 131

D.2 The jet shape for leading and non-leading jets for jets located at $\eta < 0.2$ with transverse energy between 70 and 105 GeV. Errors are statistical only. 133

D.3 The jet shape for leading and non-leading jets for jets located at $\eta < 0.2$ with transverse energy between 105 and 140 GeV. Errors are statistical only. 134

D.4 The jet shape for leading and non-leading jets for jets located at $\eta < 0.2$ with transverse energy greater than 140 GeV. Errors are statistical only. 135

D.5 The jet shape for leading and non-leading jets for jets located at $2.5 < \eta < 3.0$ with transverse energy between 45 and 70 GeV. Errors are statistical only. 136

D.6 The jet shape for leading and non-leading jets for jets located at $2.5 < \eta < 3.0$ with transverse energy between 70 and 105 GeV. Errors are statistical only. (Note only two jets comprise the leading jet measurement.) 137

ABSTRACT

Abbott, Braden K. Ph.D., Purdue University, December 1994. Jet Transverse Energy Shape in $p\bar{p}$ Collisions at $\sqrt{s}$=1.8 TeV. Major Professor: David S. Koltick.

The distribution of the transverse energy flow in hadronic jets has been measured in $p\bar{p}$ collisions at $\sqrt{s} = 1.8$ TeV at the Fermilab collider using the DØ detector. These measurements of jet shape are made in two regions of pseudo-rapidity centered at $|\eta| \sim 0$ and $|\eta| \sim 2.7$ as a function of jet transverse energy. Comparisons are made with phenomenological Monte Carlo simulations and next-to-leading-order QCD calculations without parton fragmentation.

1. Introduction

1.1 History

This thesis studies the interactions of high energy quarks and gluons and their manifestation in our world as a cone of hadronic matter. Today, it is believed that quarks and gluons are some of the most fundamental particles, the smallest building blocks of matter. This realization is based upon a multitude of ideas and experimental results obtained over many years. As long ago as 460 B.C., Democritus of Greece believed that the world was made up of tiny particles called atoms. Later, it was found that indeed the world is made up of small structures. The name "atom" was given to what is known today as the electronic structure of matter.

Atoms do form the structure of matter; however, the atom is not a fundamental particle, since the atom itself is composed of smaller particles, namely the electron, the proton and the neutron. The electron was first discovered just prior to 1897. J.J. Thompson, using equipment that operated at a few electron volts, showed the existence of a very low mass particle that was common to all atoms, the electron. Next, the proton was deduced in an experiment by Rutherford. Using a radioactive element that emitted α particles at a few MeV, he measured their angle of deflection after they passed through a thin gold foil. The observation of α particles with ex-

tremely high angles of deflection implied the existence of a small positively charged nucleus within the atom. Finally, in the 1930's, a neutral particle similar in mass to the proton was discovered by Chadwick, the neutron.

In an effort to further probe the atom, accelerators were designed to increase the energies of the probing particles. Small distances can only be investigated with radiation of a comparably small wavelength. The higher the energy, the smaller the wavelength, $\Delta\lambda \sim \frac{\hbar}{E}$. By accelerating particles to higher energies, it was hoped that structure within the protons and neutrons would be seen. However, higher energy collisions produced a proliferation of particles. Today, hundreds of distinct particles have been identified and their properties measured. Particles called pions, kaons, Λ's and Ω's, to mention a few, were copiously created in these high energy collisions. It seemed that the world was not a simple structure consisting only of protons, neutrons and electrons. Accelerators instead were creating a "zoo" of particles with no end in sight.

It was found that hadronic particles of similar mass could be grouped into isospin* multiplets, and conserved quantities such as hypercharge† could be assigned to each particle undergoing a hadronic interaction. The isospin and hypercharge symmetries can be combined into an SU(2) symmetry. A deeper interpolation of the SU(2) relationship between the hadrons hypothesized the existence of quarks and gluons, and the beginnings of the Standard Model were born.

---

*Neutrons and protons form a doublet with isospin=1/2.

†Hypercharge=baryon number + strangeness.

Table 1.1

The six fundamental leptons

Particle Name	Symbol	Generation	Rest Mass (MeV)	Charge
Electron Neutrino	ν_e	1	≤ 0.007	0
Electron	e^-		0.511	-1
Muon Neutrino	ν_μ	2	≤ 0.27	0
Muon	μ^-		106.6	-1
Tau Neutrino	ν_τ	3	≤ 31	0
Tau	τ^-		1784	-1

1.2 The Standard Model

Quarks and gluons are members in the larger family of fundamental particles. The Standard Model separates fermions, spin=1/2 particles, into two distinct groups, quarks and leptons. The quarks and leptons are considered fundamental particles, lacking substructure*, and having a pointlike behavior in calculations. Tables 1.1 and 1.2 list the six distinct types, or flavors of leptons and quarks.

Fermions interact with one another through forces. Currently there are four known forces. In order of strength, they are the strong, electromagnetic, weak and gravitational force and their properties are shown in Table 1.3. Each force interacts via propagators shown in Table 1.4.

Leptons are not carriers of the strong force. Three of the leptons have charge and are called the electron, the muon and the tau. All three of these leptons have charge -1 but differ substantially in mass. The other three leptons, the electron neutrino,

*Searches for substructure to quarks and leptons have revealed none [1].

Table 1.2

The six fundamental quarks

Particle Name	Symbol	Generation	Rest Mass	Charge
up	u	1	$\sim$ 5.6 MeV	2/3
down	d		$\sim$ 9.9 MeV	-1/3
charm	c	2	$\sim$ 1.35 GeV	2/3
strange	s		$\sim$ 199 MeV	-1/3
top	t	3	$\geq$131 GeV	2/3
bottom	b		$\sim$ 4.7 GeV	-1/3

Table 1.3

The four fundamental forces

Force	Range (cm)	Relative Strength
Strong	10^{-13}	1
Electromagnetic	infinite	10^{-2}
Weak	10^{-16}	10^{-6}
Gravity	infinite	10^{-40}

Table 1.4

The six carriers of force

Force	Carrier	Rest Mass (GeV)	Spin	Charge
Strong	Gluons	0	1	0
Electromagnetic	Photon	0	1	0
Weak	W^+	80.2	1	+1
	W^-	80.2	1	-1
	Z^o	91.2	1	0
Gravity	Graviton	0	2	0

the muon neutrino and the tau neutrino are neutral particles and are believed to be massless.

The strong force, with coupling α_s, is responsible for binding the quarks together inside hadronic particles. The strong force carriers are the gluons, which obey an SU(3) symmetry with 3^2-1 =8 different color combinations, $R\bar{G}$, $R\bar{B}$, $G\bar{R}$, $G\bar{B}$, $B\bar{R}$, $B\bar{G}$, $\sqrt{1/2}(R\bar{R} - G\bar{G})$, and $\sqrt{1/6}(R\bar{R} + G\bar{G} - 2B\bar{B})$.

Quarks can interact with all of the known forces. Their dominant interaction is with the strong force. Quarks interact through the strong force by exchanging gluons. Although there are believed to be 6 flavors* or types of quarks, only 5 have been identified. These are the up (u), down (d), strange (s), charm (c) and bottom (b). The sixth quark, the top quark (t), has yet to be found [2]. The quarks carry fractional charge; the d, s, and b quarks have charge -1/3, while the u, c and theorized t have charge 2/3.

Both the leptons and quarks can be grouped into three sets of two members called generations. The generations of leptons do not make transitions from one to another, so a conservation law must exist separately for each generation. This leads to assigning a lepton number to each lepton weak isospin multiplet which must be conserved in all interactions. Baryons, like the proton and neutron, are assigned a baryon number=1. Since each is a bound state of three quarks, the quarks each are assigned a baryon number=1/3. While the weak interaction causes quarks to mix

*Flavor is a conserved quantum number for the strong and electromagnetic forces.

across generations, it has been found experimentally that baryon number, like lepton number is also conserved in all interactions.

Not only are there leptons and quarks but antileptons and antiquarks as well. For each lepton and quark there is a corresponding antilepton and antiquark which has the same spin, mass and lifetime as its corresponding anti-partner but carries opposite charge and lepton or baryon number.

The quark model is a powerful tool in which to explain the abundance of particles. All of the known hadrons can be classified by different combinations of quarks. Mesons (pions, kaons..) are composed of quark-antiquark pairs while baryons (protons, neutrons..) are quark-quark-quark composites.

When using the quark model to understand baryons, a problem arises. The neutron consists of two d quarks and one u quark each in the ground state. The proton consists of two u quarks and one d quark, similarly in the ground state. Continuing this progression results in a baryon consisting of three u quarks, namely the Δ^{++}.

$$\text{Neutron}=udd$$

$$\text{Proton}=uud$$

$$\Delta^{++}=uuu.$$

The Δ^{++} has a spin=3/2. It can only be formed by combining three spin=1/2 quarks in their ground state. However, this would be impossible if the Pauli exclusion principle is operational for quarks, as it is for all the other half integral spin particles. This principle states that no two identical fermions can be in the same quantum state. The Δ^{++} would consists of 3 u quarks, all in the same quantum state. A

second problem arises from the quark model, namely no qq or $\bar{q}\bar{q}$ states have been found. Both of these problems have been resolved by introducing another quantum number called color. Instead of a single up quark there are three up quarks with color charge red (R), blue (B) and green (G). Anticolors also exist, called anti-red ($\bar{R}$), anti-blue ($\bar{B}$) and anti-green ($\bar{G}$). This explains why the Δ^{++} can exist, the three quarks are distinguished by their color charge and the Pauli exclusion principle is satisfied ($\Delta^{++}=u_R u_B u_G$). The color factor has been verified experimentally because it effects cross sections and particle decay rates.

In nature, all the mesons and baryons are colorless, meaning they have equal amounts of color and anticolor or an equal mixture of red, blue and green. A single quark has never been observed. Quarks have only been observed in hadrons due to a property called infrared slavery. Unlike an electron in which the force is reduced as it moves away from another charged particle, a quark behaves very differently as it moves away from another color charge. The force between two quarks is directly proportional to the distance between them. As two quarks are pulled further and further apart, the energy density in the field becomes so great that other quark pairs can form from the vacuum. This phenomenon occurs at a distance of $\sim 10^{-13}$m, approximately the size of a hadron.

The reason that no single quarks have been observed is due to the quark's color charge. We can think of any charged particle as a bare charge surrounded by a cloud of oppositely charged virtual pairs. Therefore, an electron can be thought of as a bare electron surrounded by a cloud of charges. Because opposite charges attract,

the positive charges within the cloud will be nearer to the bare electron, screening the negative charge of the electron. In other words, the vacuum acts as a classical dielectric, reducing the observed charge. As a test charge is moved farther from the electron, less of the electron's unscreened or bare charge is measured, weakening the coupling with distance.

A colored object, on the other hand, is also surrounded by a cloud of colored objects. The situation would be identical to electric charge screening if not for the fact that gluons can emit gluons. This self-coupling causes a color charge to be surrounded more closely by the same color objects within the cloud, resulting in anti-screening. As a color probe moves farther from a quark, the amount of color charge measured is increased, increasing the coupling with increasing distance. It is this property which leads to infrared slavery.

1.3 Jets

Due to infrared slavery, individual quarks and gluons, collectively called partons, cannot be directly measured. Instead, we measure the particles that these partons produce. At high energies, when two colorless hadrons collide, the most likely interaction is that a parton in one hadron interacts with a parton in the other hadron which destroys the hadron structure. The quarks and gluons not involved in the hard scatter, termed the spectators, continue approximately in the beam direction and carry off very little transverse momentum. The two objects participating in the hard scatter can obtain large amounts of transverse momenta. Since the colored objects

cannot break free, pairs will be created and bound colorless hadrons will emerge, a process known as hadronization or fragmentation. These hadrons emerge with large transverse momenta, travelling approximately in the same direction as the scattered quark or gluon. This collimated spray of particles is known as a jet. By measuring the properties of a jet, we hope to determine the properties of its parent partons.

The partons within two colliding beams have a wide range of longitudinal momentum determined by the parton distribution functions. The center of mass of the parton-parton collision is usually in motion or boosted with respect to the center of mass of the colliding hadrons. Therefore variables are used to describe jets which are invariant under longitudinal boosts; the rapidity y, the transverse momentum p_T and the azimuthal angle ϕ. The four-momentum p^μ of a particle with mass, m, can be written as

$$p^\mu = (\sqrt{p_T^2 + m^2} cosh(y), p_T sin\phi, p_T cos\phi, \sqrt{p_T^2 + m^2} sinh(y)) \tag{1.1}$$

where the rapidity y is defined as

$$y = \frac{1}{2} ln(\frac{E + p_Z}{E - p_Z}). \tag{1.2}$$

The rapidity is additive under Lorentz transformations corresponding to boosts along the z direction. Rapidity differences are a Lorentz invariant. Since the mass of the particle is unknown, but is most likely to be m_π, a more easily measured variable is the pseudo-rapidity, η, which is straight forward to derive,

$$y \approx -ln\ tan\ \theta/2\ \equiv\ \eta.$$

Where the particle mass has been set to zero in comparison to its momentum.

The pseudo-rapidity is simple to measure experimentally because of its relation to the polar angle θ. Because DØ has no magnetic field, the transverse energy of a particle, that is its energy transverse to the beam axis, is measured instead of its transverse momentum. In the limit that $|P| \gg m$, $P_\perp \sim E_T$, which is a valid approximation at DØ. Hence the variables used in analyses are η, E_T, and ϕ for both the measurement of individual particles and the energy within a jet.

1.4 Motivation

The current theory which describes the interactions of quarks and gluons is known as Quantum Chromodynamics or QCD. This theory uses a perturbative approach in order to calculate measurable quantities by calculating processes at different orders in α_s. The first order calculation is known as leading order (LO) and the next order is known as next-to-leading order (NLO). Leading order processes consist of only two jets and are the simplest processes to calculate. At next-to-leading order, calculations become more complex since three final state jets are possible.

Recent advances in the theoretical understanding of jet production at hadron colliders improve quantitative comparisons to experiment [3]. Present theoretical predictions allow theoretical ensembles of jets as a function of relativistically invariant variables to be compared to ensembles of physical jets. We compare our experimental data to a next-to-leading order calculation of the transverse energy flow in a jet.

One difficulty in interpreting as well as making these jet physics measurements

is how to define a jet. At the theoretical level, there are only partons, i.e., quarks and gluons in a jet. QCD theory currently is incapable of calculating the low energy fragmentation process and is only able to calculate hard processes with large momentum transfers with reasonable precision. This simplification works well for many physical processes. Calculations at this level describe many experiments, including inclusive jet production and production of di-jets. However, these calculations treat the jets as having no structure. This theoretical picture of jets cannot be true since fragmentation within hadronic jets must cause structure. At this time, fragmentation can only be understood as a phenomenological process. However, the question must be asked; what dominates the internal structure of jets, the fragmentation process or the underlying simple partonic processes which are calculable up to NLO? This thesis tests the importance of fragmentation relative to partonic processes in hadronic jet shapes.

Leading order partonic processes consist of only two final state partons, which balance transverse momentum. In this case the shape of the energy flow is simply a delta function at the parton's coordinates since all of the jet's energy is located along its axis. At next-to-leading order, jet shapes become more realistic allowing three final state partons. Depending on the jet algorithm, one or two partons may reside in a final state jet. The energy within a theoretical jet can therefore be distributed around the jet axis, in the sense of an ensemble or probability distribution, allowing a theoretical jet shape to be calculated. This theoretical shape can then be compared to the experimental data in the same way, as an ensemble.

There are many features of jet physics which can be studied at the DØ detector. The first feature is the change in jet shape as the jet transverse energy, E_T, changes. A change is expected because the transverse momentum of a particle as measured from the jet axis changes slowly with energy while the parallel momentum of a particle within the jet changes approximately with energy. A second measurable feature is the change in jet shape as the jet η changes. Forward, or high η jets are expected to be narrower than central, or $\eta \sim 0$, jets at the same E_T. The cause of this is the theoretical prediction that quark and gluon jet production is η dependent with quark production dominating at high η. A simple explanation of this argument is that di-jet events with both jets at high η must have resulted from a collision of a parton with a low momentum fraction and a parton with a high momentum fraction. Gluons rarely have a high momentum fraction, so the gluon-gluon contribution at high η diminishes, giving an enhanced quark sample. Quark jets are expected to be narrower than gluon jets because gluons, carrying more color than quarks, emit gluons more readily, tending to widen the jet.

DØ is particularly well suited to study these jet features, due to the calorimeter's fine segmentation and large η coverage. Other experiments have measured the transverse energy flow [4] with tracking chambers, considering only the energy carried by charged particles. Typically, charged particles contain only about 2/3 of the energy of a jet and fluctuations can occur in the charged particle content. In our measurement, both neutral and charged particles contribute to the jet shape. By comparing our measurement to previous measurements, we can also determine the effects of the

neutral component within a jet. Due to the calorimeter's large η coverage, $|\eta| < 4$, DØ is also able to extend this measurement to the far forward region, a previously unexplored region.

In order to determine if fragmentation effects are important for determining the jet shape, we compare a theoretical prediction at the partonic level with no fragmentation effects (JETRAD [3]) to our experimental data. Figures 1.1 and 1.2 compare the experimentally measured jet shape in different η regions to the current theoretical predictions. Note the large effects due to the parameter μ, a non-physical theoretical parameter used to remove infinities introduced when calculating physical quantities. Differences in a range of values for μ give an estimate of the current theoretical uncertainties. For centrally located jets, theoretical predictions at NLO are able to describe the jet shape within the uncertainties resulting from the choice of renormalization scale. In the previously unmeasured forward region, however, NLO predictions are unable to describe the jet shape.

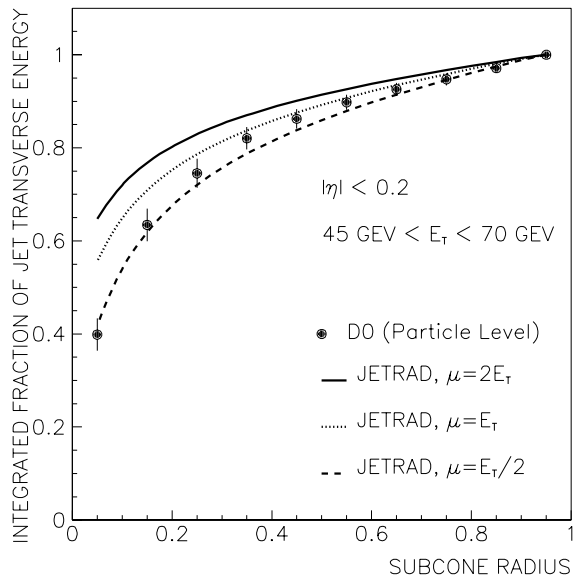

Figure 1.1

A comparison between the experimentally measured jet shape and a theoretical prediction using three different values of μ for centrally located jets.

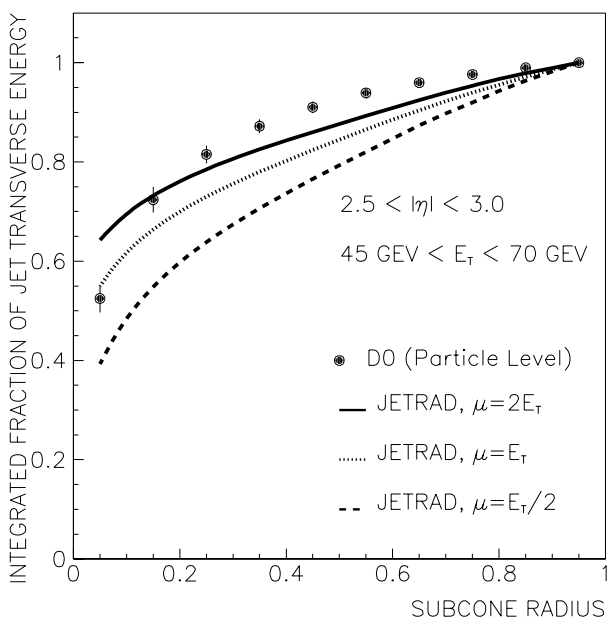

Figure 1.2

A comparison between the experimentally measured jet shape and a theoretical prediction using three different values of μ for jets located in the forward region.

2. QCD Theory

2.1 Lagrangian of QCD

Quantum Chromodynamics, an SU(3) gauge theory, arose with the introduction of colored quarks. The QCD Lagrangian density which describes the interaction of spin 1/2 quarks of mass m and spin=1 massless gluons is given by [5]

$$\mathcal{L} = -\frac{1}{4}F^A_{\alpha\beta}F^{\alpha\beta}_A + \sum_{flavors} \bar{q}_A(i\gamma^\mu D_\mu - m)_{AB}q_B + \mathcal{L}_{gauge-fixing} + \mathcal{L}_{ghost} \tag{2.1}$$

where $F^A_{\alpha\beta}$ is the field strength tensor which is found from the gluon field A^A_α,

$$F^A_{\alpha\beta} = \partial_\alpha A^A_\beta - \partial_\beta A^A_\alpha - gf^{ABC}A^B_\alpha A^C_\beta \tag{2.2}$$

The indices A, B, C run over the color degrees of freedom of the gluon field. The third term in equation 2.2 is a non-Abelian term which distinguishes QCD from QED. This is the term which gives rise to gluon tri-linear and quartic self-interactions, see Figure 2.3. The sum over flavors is a sum over the different flavors of quarks, u, d, s, ... The coupling constant, g, determines the strength of the interaction between colored partons, and f^{ABC} are the structure constants of the SU(3) color group. The quark fields q_A are in the triplet representation of the color group and D is the covariant derivative. It is impossible to use perturbation theory on a gauge invariant Lagrangian without choosing a specific gauge in which to calculate. The usual gauge-fixing term

is

$$\mathcal{L}_{gauge-fixing} = -\frac{1}{2\lambda}(\partial^\alpha A^A_\alpha)^2. \tag{2.3}$$

This choice fixes the class of covariant gauges with λ as the gauge parameter. Because QCD is non-Abelian, the gauge fixing term must be supplemented by a ghost Lagrangian.

$$\mathcal{L}_{ghost} = \partial_\alpha \eta^{A\dagger}(D^\alpha_{AB}\eta^B) \tag{2.4}$$

where η^A is a complex scalar field which obeys Fermi statistics. The ghost fields cancel unphysical degrees of freedom which arise due to using covariant gauges. This explains the complete Lagrangian shown in equation 2.1.

2.2 The running coupling constant

The fundamental picture we are working with consists of colored quarks and gluons interacting with coupling strength α_s. The coupling constant, α_s, however, is not a constant, it is a function of the momentum transferred in the interaction. Consider a dimensionless physical observable $\mathcal{R}$ which depends on an energy scale Q. Allow the scale Q to be much larger than all other parameters, such as the particle masses involved. With this assumption, all masses can be set to zero and since there is only one large single scale Q, $\mathcal{R}$ should be independent of Q.

However, this is not true in renormalizeable quantum field theory. When $\mathcal{R}$ is calculated as a perturbation series in α_s, the series requires renormalization to remove ultra-violet divergencies. This renormalization introduces a second mass scale μ, known as the renormalization parameter. This is the point at which the subtractions

to remove the divergencies are performed. Now, $\mathcal{R}$ depends on Q/μ and so it is no longer independent of Q, and α_s is now dependent upon the choice of renormalization parameter. This renormalization parameter is required in order to calculate physical quantities in QCD, but this renormalization point is arbitrary. Therefore, a physically measured quantity, $\mathcal{R}$, cannot depend on the choice of μ. This means

$$\mu^2 \frac{d}{d\mu^2}\mathcal{R}(\frac{Q^2}{\mu^2}, \alpha_s) = (\mu^2 \frac{\partial}{\partial \mu^2} + \mu^2 \frac{\partial \alpha_s}{\partial \mu^2}\frac{\partial}{\partial \alpha_s})\mathcal{R} = 0 \tag{2.5}$$

where we take the derivative with respect to μ^2 for convenience. To write equation 2.5 in a more compact form, define t and $\beta(\alpha_s)$ to be

$$t = ln(\frac{Q^2}{\mu^2}), \quad \beta(\alpha_s) = \mu^2 \frac{\partial \alpha_s}{\partial \mu^2} \tag{2.6}$$

Using the variables t and $\beta(\alpha_s)$, equation 2.5 can be rewritten as

$$(-\frac{\partial}{\partial t} + \beta(\alpha_s)\frac{\partial}{\partial \alpha_s})\mathcal{R} = 0 \tag{2.7}$$

This equation can be solved by defining a new function, $\alpha_s(Q)$ as

$$t(Q) = \int_{\alpha_s}^{\alpha_s(Q)} \frac{dx}{\beta(x)} \tag{2.8}$$

Differentiating equation 2.8 with respect to t and α_s separately yields

$$\frac{\partial \alpha_s(Q)}{\partial t} = \beta(\alpha_s(Q)), \quad \frac{\partial \alpha_s(Q)}{\partial \alpha_s} = \frac{\beta(\alpha_s(Q))}{\beta(\alpha_s)} \tag{2.9}$$

By setting $Q^2 = \mu^2$, we find that $\mathcal{R}(1, \alpha_s(Q))$ is a solution to equation 2.7. All of the scale dependence is in the running of the coupling constant α_s, making α_s a function of the scale Q. If the value of $\alpha_s(Q)$ is known at one point Q', it can be predicted at another point Q''.

The β function in QCD has a perturbative expansion given by

$$\beta(\alpha_s) = -b\alpha_s^2(1 + b' + O(\alpha_s^2)) \tag{2.10}$$

where $b = \frac{(33-2n_f)}{12\pi}$, $b' = \frac{(153-19n_f)}{2\pi(33-2n_f)}$ and n_f is the number of active light flavors. Therefore equation 2.9 may be written as

$$\frac{\partial\alpha_s(Q)}{\partial t} = -b\alpha_s^2(Q)[1 + b'\alpha_s(Q) + O(\alpha_s^2(Q))] \tag{2.11}$$

In the perturbative region, the first order solution of equation 2.10 is given by

$$\alpha_s(Q) = \frac{\alpha_s(\mu)}{1 + \alpha_s(\mu)bt}, \tag{2.12}$$

Note that as t becomes large, α_s approaches 0. In other words, as Q^2 increases $\alpha_s(Q)$ decreases, allowing the quarks to behave as free particles within the hadron, a property known as asymptotic freedom.

The renormalization scale is not a truly arbitrary parameter, it should be chosen to be on the order of the hard scale Q $\sim E_T$ because perturbation theory is only valid for a small range of values for μ. Figure 2.1 shows how a typical cross section changes with the choice of renormalization parameter. If the renormalization parameter becomes too small, μ less than $\sim E_T/2$, LO and NLO calculations differ greatly. This implies that higher order terms are not small so perturbation theory is not valid. For values of $\mu \sim E_T$, perturbation theory works well because the series can be expanded about a small value. LO and NLO calculations differ slightly, so a perturbative expansion is valid since adding an additional higher order term introduces only a small change.

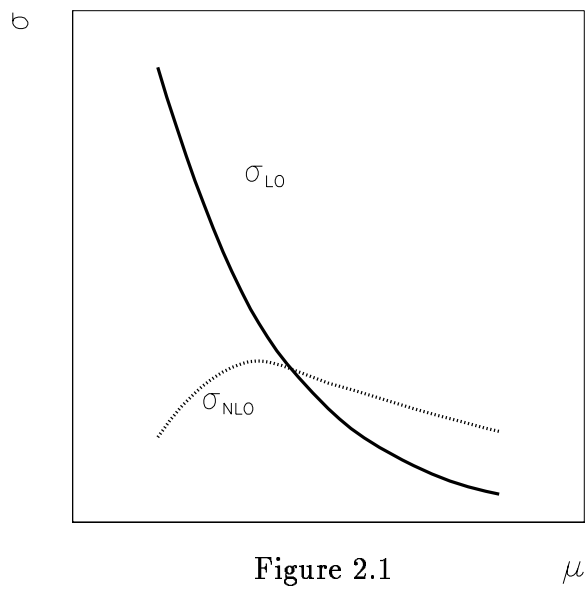

Figure 2.1

Schematic diagram indicating the renormalization scale dependence on a typical cross section.

For μ greater than $\sim 2E_T$, LO and NLO again begin to diverge causing perturbation theory to be no longer valid.

By using perturbative QCD, the change of the coupling constant with scale can be calculated, but it cannot give an absolute value for α_s. Therefore, a fundamental parameter can be chosen as some convenient reference scale which is large enough to be in the perturbative region. By convention this parameter is defined as Λ and is a constant of integration defined as

$$ln\frac{Q^2}{\Lambda^2} = -\int_{\alpha_s(Q)}^{\infty} \frac{dx}{\beta x} \tag{2.13}$$

Λ represents the scale at which $\alpha_s(Q)$ becomes strong. Using Λ, $\alpha_s(Q)$ can be written

as

$$\alpha_s(Q) = \frac{1}{bln(Q^2/\Lambda^2)} \tag{2.14}$$

2.3 Leading order and next-to-leading order calculations

A perturbative expansion in α_s is generally performed to calculate measurable quantities in QCD. Physical quantities are calculated by separating processes at different orders in α_s. At leading order only two jets can exist. Calculations at LO allow for only $gg \rightarrow gg$, $qq \rightarrow qq$, $qg \rightarrow qg$, $q\bar{q} \rightarrow q\bar{q}$, $q\bar{q} \rightarrow gg$, and $gg \rightarrow q\bar{q}$. Figure 2.2 shows some of the diagrams which contribute to leading order parton-parton scattering. Each vertex in these diagrams is proportional to α_s. Since each diagram at LO has two vertices, calculations can only be performed at order $O(\alpha_s^2)$. Typically leading order calculations depend heavily upon the choice of renormalization scale, leading to uncertainties in most LO calculations of about 30%. In order to reduce the theoretical uncertainties, higher order diagrams can be introduced. As more terms are included in the perturbative expansion, the dependence on μ decreases, reducing the theoretical uncertainties.

At next-to-leading order, calculations may include three jet events, because diagrams such as $gg \rightarrow ggg$ are now possible. NLO must also include a larger number of two jet diagrams arising from loops. Figure 2.3 shows some of the diagrams contributing to NLO parton-parton scattering. At NLO, each diagram has either three or four vertices, allowing calculations of order $O(\alpha_s^3)$ to be performed. Terms which are of order $O(\alpha_s^4)$ are ignored. NLO is much less sensitive to the renormalization

scale. Calculations at this order typically have errors of $\sim 10\%$.

Calculating quantities to all orders in α_s is the ultimate goal. However, it becomes increasingly difficult to calculate higher order processes. At NLO, calculations require over 100 separate diagrams. The number of diagrams necessary to calculate higher order corrections is large and the mathematics and computing time is foreboding. Currently only exact NLO calculations are available.

2.4 Parton Distribution Functions

In addition to needing a renormalization scale to calculate physical quantities in QCD, parton distribution functions are also required. Parton distribution functions parameterize the quark and gluon momentum distribution within the proton as a function of Q^2, where Q is the momentum transferred. They are measured by deep inelastic scattering experiments, in which a high energy lepton is scattered on a hadron target. By measuring the cross section of $lp \to lX$ and $\nu p \to lX$, the parton distribution functions can be found. Since parton distribution functions are an experimentally measured quantity, different parameterizations exist. For this study we use the most recent parameterizations.

Figure 2.2

Feynman diagrams contributing to lowest order parton-parton scattering.

Figure 2.3

Feynman diagrams contributing to next-to-leading order parton-parton scattering.

3. Experimental Apparatus

3.1 Fermilab

The DØ detector is one of the two major detectors currently operating with colliding beams at Fermilab in Batavia, Illinois. Fermilab has the world's highest energy $p\overline{p}$ collider, achieving a center of mass energy $\sqrt{s}$=1.8 trillion electron volts (1.8 TeV).

The two accelerator parameters most relevant to this study are the beam energy and the luminosity. The beam energy determines the percentage of quark and gluon jets within a selected rapidity region. As the beam energy is increased, the contribu-

Figure 3.1

A schematic view of Fermilab.

tion from gluons participating in a hard scatter is enhanced, increasing the number of gluon jets produced. Since quark and gluon jets are expected to have different jet shapes, the beam energy directly effects our measurement.

The luminosity is a measure of the number of interactions per second, so it directly determines the probability of a multiple interaction occurring within a single beam crossing. As the number of multiple interactions increases, the background energy within an interesting event due to spectator interactions also increases. This energy is due to low momentum transfer processes and cannot be determined using perturbative QCD calculations. The jet shape must therefore be corrected for this background in order to compare to theoretical predictions.

Figure 3.1 shows the layout of the Tevatron and the two main colliding beam detectors. In order for protons to achieve such a high energy, many stages of acceleration are needed. First, H^- ions are accelerated by a Cockcroft-Walton accelerator to an energy of 750 KeV. The H^- ion beam is then sent to a linear accelerator, the Linac, where it is further accelerated to an energy of 200 MeV. The H^- is then sent through a thin target which strips the 2 electrons, leaving H^+. This proton beam is guided into a booster where it is accelerated to 8 GeV. The 8 GeV protons are then sent clockwise into the 6.3 km main ring where they are accelerated to 150 GeV. Six bunches of protons are finally sent into the Tevatron where they are accelerated until they reach their final energy of 900 GeV.

The protons from the main ring are also used to generate anti-protons. Antiprotons are produced by sending 120 GeV protons into a copper and nickel target. For

every 10^6 protons that strike the target, only about 20 anti-protons are collected. The anti-protons that emerge from the target have a large angular divergence and momentum spread. It is necessary to store and stack the anti-protons until a sufficient number exist to start colliding. In order to store the anti-protons, the anti-proton beam is sent through a debuncher and the beam is stochastically cooled [6]. The debuncher reduces the energy spread by using the principle that $\Delta E \Delta t \sim$ constant. By increasing the time spread of the anti-protons, the energy spread is reduced. Cooling refers to bringing the anti-protons into orbits with a smaller range of momenta. In stochastic cooling, the average position of the anti-proton beam is determined. If the center of the beam has moved from nominal, a signal is sent to the opposite side of the cooling ring. Magnets move the center of the beam back to the nominal position. Some anti-protons are lost by this process, but the majority have their extraneous components of momenta reduced, cooling the beam. The cooled anti-protons are stored in a magnetic storage ring at 8 GeV until enough of them exist that they can be put into the main ring.

The stacking rate of anti-protons is approximately 3 x 10^{10} anti-protons/hour. A stack of $\sim 10^{12}$ anti-protons is not uncommon, so it can take many days of stacking before the number is sufficient for collisions. When the stack of anti-protons reaches a sufficiently high level, six bunches of anti-protons are sent counter clockwise into the main ring. Within the main ring, the anti-protons are accelerated to an energy of 150 GeV. Finally, they are sent to the Tevatron where they achieve their final energy of 900 GeV. Currently, six bunches of protons collide every 3.5 μs with six bunches

of anti-protons at 2 locations along the Tevatron. It is at these two locations, that the two major detectors (DØ and CDF) gather their data.

3.2 The DØ Detector

The DØ detector, shown in figure 3.2, is a general purpose detector with good electron and muon identification and excellent calorimetric energy and spatial resolution. The coordinate system used at DØ is a right handed coordinate system with the positive z-axis along the proton direction and the y-axis defined as vertical.

The DØ detector is described in detail elsewhere [7], [8], [9] and consists of three main detectors:

- Tracking System
    1. Inner Vertex Tracker (VTX)
    2. Transition Radiation Detector (TRD)
    3. Outer Drift Tracking Chambers
        (a) Central Drift Chamber (CDC)
        (b) 2 Forward Drift Chambers (FDC)
- Calorimetric System
    1. Central Calorimeter (CC)
    2. 2 Endcap Calorimeters (EC)
    3. InterCryostat Detector (ICD)
- Muon System
    1. Central Muon System

Figure 3.2

The DØ Detector.

2. Wide Angle Muon System (Wamus)

3. Small Angle Muon System (Samus)

Only the detector elements most relevant to this study will be discussed. The quantities relevant to this analysis are the measurement of the η, ϕ and E_T of a jet. The detectors used to determine these quantities are the tracking chambers and the calorimeter. The tracking chambers determine the vertex of the interaction accurately. The accuracy of both η and E_T are dependent upon measuring the vertex well. Without tracking chambers, the z vertex can be determined to within $\sim$ 3 cm [7]. A simple calculation reveals that the error in determining the jet η is $\Delta\eta_{jet} \sim \Delta z_{vertex}/2r$. A 3 cm vertex error causes $\Delta\eta_{jet} \sim 0.03$. This error is to be compared to the detector segmentation of $\Delta\eta = 0.1$.

The combination of the vertex chamber, central drift chamber and forward drift chambers, shown in figure 3.3, allow for a z vertex measurement of $\sim$ 6 mm [7]. A vertex mismeasurement of 6 mm causes an error of less than 0.007 in calculating the jet η, and an error in the jet E_T of less than 0.5%, more than sufficient for this analysis.

3.3 Tracking Chambers

3.3.1 Vertex Chamber

The tracking detector closest to the beam pipe is the vertex chamber [10] which extends from r = 3.7 cm to 16.2 cm and $|z| < 58$ cm. The walls of vertex chamber are made of carbon fiber in order to reduce radiation lengths to avoid photon conversions

Figure 3.3

Tracking Volume

and to minimize energy loss of particles before they reach the calorimeter.

The chamber consists of three mechanically independent layers with eight sense wires each. The wires within each layer are supported by G-10 bulkheads mounted on a carbon fiber tube. The sense wire spacing is 4.57 mm with a maximum drift distance of 16 mm. The sense wires are staggered $\pm$ 100 μm to resolve left-right ambiguities. The gas is dimethyl ether (95% CO_2, 5% Ethane) with a small admixture of H_2O at atmospheric pressure. A spatial resolution of 60μm was measured for drift distances over 2 mm [11].

3.3.2 Central Drift Chamber

The central drift chamber measures tracks for $|\eta| < 1.0$, extending from 49.5 cm to 74.5 cm in r and $|z| < 92$ cm. The central drift chamber consists of four superlayers separated by thin walls. Each superlayer is segmented by 32 independent supercells each separated by a thin foil. Within each supercell are two delay lines and seven sense wires in the plane ϕ=const. The sense wires are 6 mm apart and separated by potential wires to reduce crosstalk and to focus the drift field onto the sense wires. Sense wires are staggered by $\pm$200 μm to resolve the left-right ambiguity. The drift field is produced and shaped by conductive strips on the inner surface of each supercell. The maximum drift distance is 7 cm and the time between bunches is 3.5 μs, so a slower gas of argon-methane is used to enhance multiple track efficiency. Alternate radial supercells are rotated by 1/2 cell to minimize right-left ambiguities and to keep the ϕ cracks between supercells from overlapping. The chamber samples

at 28 locations along the trajectory and samples the delay coordinate at 8. The spatial resolution is $\sim 150\mu$m in the $r\phi$ plane [7].

3.3.3 Forward Drift Chambers

The forward drift chambers were designed to measure tracks for $|\eta| > 1.0$. They cover the pseudorapidity region $1.0 < |\eta| < 3.5$. The forward drift chambers consist of two types called θ chambers and ϕ chambers. Both are located between r = 11 to 62 cm. The θ modules run from $|z|$=104.8 to 111.2 cm and from $|z|$=128.8 to 135.2 cm while the ϕ modules run from $|z|$=113 to 127 cm. The ϕ chamber has 16 layers of radial sense wires. Each wire is 50 cm and the maximum drift distance is 5.3 cm. A standard gas is used, argon-methane, the same as in the central drift chamber. The ϕ chamber is located between two θ chambers. The two θ chambers each have 8 layers of sense wires. The two θ chambers are rotated 45° relative to each other. Sense wires for both the θ and ϕ modules are staggered by 200μm. The spatial resolution is $\sim 200\mu$m in the $r\phi$ plane [7].

3.4 Calorimeter

The calorimeter, shown in figure 3.4, is the detector most relevant for this study, because it measures the η, ϕ and energy within the jets. This analysis of jet shape depends heavily on the calorimeter being able to make these measurements accurately, therefore it will be discussed at some length.

The basic structure of the calorimeter is a projective tower ($\Delta\eta \times \Delta\phi = 0.1 \times 0.1$) pointing to the interaction vertex, containing 10-12 longitudinal layers of individual

Figure 3.4

Calorimeter

Figure 3.5

Section of calorimeter module showing absorber plates, liquid argon and signal boards. (not to scale)

Figure 3.6

Side view of the DØ calorimeter. Calorimeter cells are shown as alternate colors of grey and white within a projective tower. Superimposed above the calorimeter is the η position of each tower assuming a nominal vertex of z=0.

readout cells. A diagram showing the basic cell structure, indicating the location of the absorber plates and liquid argon gaps, is shown in figure 3.5. Figure 3.6 shows a side view of the calorimeter. The cell structure is shown as alternate colors of grey and white within the projective tower structure. The numbers above the calorimeter indicate the η position of each tower assuming a vertex of z=0.

The calorimeter was designed to provide good energy resolution for jets and electrons and to provide good energy containment. In order to keep the calorimeter compact, radiation hard and have uniform response for electrons and pions, uranium-liquid argon was used. The DØ calorimeter is a sampling calorimeter, meaning that the calorimeter does not measure all of the energy of a particle as it passes through the liquid argon, only a small fraction. The fraction of energy that a particle deposits in the liquid argon, the sampling fraction, was measured in a test beam, giving sampling fractions between $\sim$ 1% and $\sim$ 10% depending upon the cell's location in DØ. By multiplying the cells measured energy by its sampling fraction, the energy of a particle is measured. Because of large fluctuations in the electromagnetic component of hadronic showers, the resolution of hadronic calorimeters improves dramatically if the calorimeter is compensating. A compensating calorimeter means that the electronic response to electrons and hadrons of the same energy is the same, $\frac{E_e}{E_\pi}$=1. In general, the response to electrons is higher than for hadrons. When a hadron interacts with a nucleus, a large number of secondary particles can be produced. The energies of the secondary particles, such as neutrinos, muons, and protons, often cannot be measured, reducing the hadronic response. To achieve compensation either the hadronic

signal must be increased or the electromagnetic signal reduced. It was thought that using uranium as an absorber would increase the hadronic signal due to nuclear fission. However, measurements revealed that the hadronic energy gained through nuclear fission is not enough to achieve compensation. Compensation was achieved by exploiting the fact that electrons and hadrons interact differently depending on the atomic number of the absorber. By changing the ratio of the absorber thickness to the sampling material thickness, near compensation was achieved. Using uranium and liquid argon reduces the electromagnetic signal, bringing the $\frac{E_e}{E_\pi}$ ratio to $\sim$1.03 [12], see Figure 3.7 [13].

Figure 3.7

a) Pulse height spectrum of 25 GeV electrons. b) Pulse height spectrum of 25 GeV hadrons/muons.

In order to measure the energy of a jet well, it is important that all of the particles

within a jet deposit their energy within the calorimeter. Any energy leaking out the back of the calorimeter will degrade the energy measurement. Electromagnetic and hadronic particles interact differently so the calorimeter was designed to fully contain both.

Electrons primarily lose energy in matter through Bremsstrahlung at high energies and ionization at low energies. Photons primarily lose energy through pair production at high energies and Compton scattering at low energies. This energy loss of electromagnetic particles can be described in a material independent way using χ_o, the radiation length. The fraction of energy that a electromagnetic particle retains after traversing a distance, s, is given by

$$F(x) = e^{-\frac{s}{\chi_o}}. \tag{3.1}$$

Hadronic particles interact mostly through nuclear interactions, and the fraction of particles absorbed through nuclear interactions after traversing a distance s is given by

$$F(x) = e^{-\frac{s}{\Lambda}} \tag{3.2}$$

where Λ is the absorption length. At DØ the calorimeter is greater than $20\chi_o$ and 7Λ thick, therefore greater than 99% of a jet's energy is contained within the calorimeter, allowing for excellent energy measurements.

It is also important that the calorimeter have good energy resolution. Large fluctuations in the energy measurement will cause jet energies to be mismeasured, creating large errors in jet analyses.

The energy resolution, σ_E, for a calorimeter is generally expressed as

$$(\frac{\sigma_E}{E})^2 = C^2 + \frac{S^2}{E} + \frac{N^2}{E^2} \tag{3.3}$$

where E is the particle's energy. C is a constant error due to electronic calibration, inhomogeneities in the calorimeter and the fact that $\frac{E_e}{E_\pi} \neq 1.0$. S is due to sampling fluctuations of the showers in the liquid argon, and N is a noise term due to uranium and electronic noise. At low energies, the noise term dominates at DØ. As the energy is increased, the resolution improves and it is the sampling fluctuations which determine the resolution. At high energies, the constant term dominates, yielding the ultimate energy resolution of the calorimeter.

3.4.1 Central Calorimeter

The main purpose of the central calorimeter is to measure the energy and position of electrons and jets in the central region ($|\eta|$ <1.0). It extends from a radius of 84.5 cm $< r <$ 218 cm from the beam for 262 cm along the beam axis.

The central calorimeter is composed of 3 concentric cylindrical shells, the electromagnetic calorimeter, the fine hadronic calorimeter and the coarse hadronic calorimeter.

Some characteristics of the central calorimeter are shown in table 3.1

3.4.2 Central Electromagnetic Calorimeter

The first layer within the calorimeter is designed to measure the energy of elec-

Table 3.1

Central Calorimeter Characteristics

	EM	FH	CH
Absorber	Uranium	Uranium	Copper
Absorber thickness	0.3 cm	0.6 cm	4.65 cm
Total χ_o at η=0	20.5	96.0	32.9
Total Λ at η=0	0.76	3.2	3.2
Argon gap	0.23 cm	0.23 cm	0.23 cm
Number of modules	32	16	16
Sampling fraction	11.79%	6.79%	1.45%
Number of cells	10368	3000	1224

tromagnetic particles. The electromagnetic calorimeter is ~20.5 radiation lengths thick, so almost all of an EM particle's energy is contained within this layer. The energy resolution for electrons has been measured at a test beam giving values of C=0.003±.004, S=0.162±.011$\sqrt{GeV}$ and N=.140 GeV [12]. The linearity has also been measured in a test beam yielding deviations of less than 1% [12].

32 separate electromagnetic modules make up the central calorimeter's electromagnetic layer giving a total of approximately 10,400 channels. The segmentation of a standard calorimeter tower is $\Delta\eta \times \Delta\phi$ =0.1 × 0.1. However, in the third longitudinal layer the segmentation decreases to .05 × .05 to improve the position resolution, for this is where electromagnetic showers deposit most of their energy. The position resolution for electromagnetic showers is approximately given by

$$\frac{\sigma_{Pos}}{E} = \frac{8mm}{\sqrt{E}} \tag{3.4}$$

where the energy is measured in GeV.[7]

3.4.3 Central Hadronic Calorimeter

The electromagnetic layer corresponds to 0.76 interactions lengths, causing approximately 53% of hadrons to interact within this layer. To accurately measure the energy of the more penetrating particles such as pions, the hadronic section of the calorimeter is made up of two distinct layers. The first hadronic section of the calorimeter is known as the fine hadronic layer.

The fine hadronic layer is 3.2 absorption lengths thick causing approximately 96% of hadrons interact within this layer. The hadronic energy resolution can be expressed as in equation 3.3. In the fine hadronic layer, the energy resolution for pions has been measured in a test beam to be C=0.047±.005, S=0.439±.042$\sqrt{GeV}$ and N=1.28 GeV. and for electrons is C=0.010±.004, S=0.233±.010$\sqrt{GeV}$ and N=1.22 GeV [12]. The linearity for this layer has been measured to be about 2%, [12] see Figure 3.8.

Figure 3.8

Calorimeter response to pions and electrons for 2 through 150 GeV/c.

Table 3.2

End Calorimeters Characteristics

	EM	IFH	ICH	MFH	MCH	OH
Absorber	U	U	Steel	U	Steel	Steel
Absorber thickness (cm)	0.4	0.6	0.6	0.6	4.65	4.65
Total χ_o	20.5	121.84	32.78	115.5	37.95	65.07
Total Λ	0.949	4.91	3.57	4.05	4.08	7.01
Argon gap (cm)	0.23	0.21	0.21	0.22	0.22	0.22
Number of modules	1	1	1	16	16	16
Sampling fraction (%)	11.9	5.66	1.53	6.68	1.64	1.64
Number of cells	7488	5900		1664		960

Hadronic showers have large fluctuations in the location of maximum energy deposition. To avoid energy leaking out the back of the calorimeter, an additional 3.2 absorption length hadronic layer was built called the coarse hadronic calorimeter, which samples the end of the hadronic showers.

3.4.4 End Calorimeters

To measure the energies of particles above $|\eta|$ >1.1 the end calorimeters must be used [14], [15]. Some characteristics of the end calorimeters are shown in table 3.2*. Each end calorimeter consists of 4 separate layers, the electromagnetic, the inner hadronic, the middle hadronic, and the outer hadronic. The end calorimeters cover the region $1.1 < |\eta| < 4.0$. The standard tower size is $\Delta\eta \times \Delta\phi = 0.1 \times 0.1$, but near the beam axis this can increase to 0.3×0.3 at the inner radii due to the constraint

*In the Number of cells column, 5900 is the sum of IFH and ICH, and 1664 is the sum of MFH and MCH.

that the minimum pad size not be smaller than $2 \times 2\ cm^2$.

3.4.5 End Calorimeter Electromagnetic Layer

The outer radius varies between 84 cm and 104 cm while the inner radius is 5.7 cm. The energy resolution for electrons has been measured at a test beam giving values of C=0.003±.003, S=0.157±.006$\sqrt{GeV}$ and N=.29 GeV. [15] The position resolution is given by

$$\sigma(mm) = \frac{16.6}{E^{0.66}} \tag{3.5}$$

where the energy is measured in GeV.[15] The non-linear response has been measured to be less than 0.3% for electrons between 10 and 100 GeV.[15]

3.4.6 End Calorimeter Inner Hadronic Layer

This layer is cylindrical with an inner radius of 3.92 cm and an outer radius of 86.4 cm. It contains two separate hadronic layers called the fine hadronic and the coarse hadronic. Within the fine hadronic layer there are 4 readout sections with each section containing semicircular uranium plates of 1.1 Λ. The coarse hadronic section has a single readout layer containing stainless steel plates of 4.1 Λ.

3.4.7 End Calorimeter Middle Hadronic Layer

This layer also contains two separate layers, fine and coarse hadronic. The fine hadronic section has 4 separate uranium layers at 0.9 Λ each. The coarse hadronic section consists of a single layer of stainless steel and is 4.4 Λ.

The energy resolution has been measured to be C=0.010±.004, S=0.233±.010$\sqrt{GeV}$

and N=1.22 GeV for electrons and C=0.047±.005, S=0.439±.042$\sqrt{GeV}$ and N=1.28 GeV for pions.

3.4.8 End Calorimeter Outer Hadronic Layer

These modules use stainless steel plates inclined at an angle of 60° relative to the beam axis. The purpose of this layer is to capture all of the energy in the calorimeter, minimizing leakage out the back of the calorimeter.

3.5 Triggers and Data Acquisition

The trigger system used at DØ is very important for this measurement. The trigger system can determine if an event is a possible multiple interaction. As discussed earlier, the energy due to multiple interactions effects the jet shape. The triggers also determine the energy and η regions over which we can explore. Jets can only be studied where the triggers are efficient and where sufficient statistics allow a measurement.

With an expected luminosity of $\sim 10^{30} cm^{-2} s^{-1}$ and an average cross section for inelastic scattering $\sigma_{inel} \approx 50$ mb, an interaction rate of 50 KHz is expected. To reduce this to a reasonable rate (1-2 Hz), three different levels of triggers are used, termed the level 0, level 1 and level 2 triggers. Figure 3.9 shows a schematic of the trigger structure.

3.5.1 Level 0

The level 0 trigger [16] is a hardware trigger consisting of two scintillator ho-

doscopes. The two hodoscopes are located on the front surfaces of the end calorimeters. Two planes of scintillator rotated by 90° make up each hodoscope. Each hodoscope has 20 short (7cm x 7cm) elements readout by single phototubes and 8 long (7cm x 65 cm) elements readout by phototubes at each end. These hodoscopes give partial coverage between $1.9 < |\eta| < 4.3$ and nearly full coverage for $2.3 < |\eta| < 3.9$. The luminosity is determined from the level 0 trigger by registering the presence of low angle particles produced in the interaction region. The luminosity is calculated by dividing the level 0 rate by the known inelastic cross section.

The level 0 trigger can also measure the z vertex in an event by measuring the arrival time difference between the two hodoscopes. The time resolution of each level 0 counter is less than 150ps giving a z vertex resolution of $\sim$3 cm [7]. If the time difference information between the two hodoscopes is ambiguous a flag is set identifying the event as a possible multiple interaction.

3.5.2 Level 1

The level 1 trigger[17], [18] is also a hardware trigger and triggers on interactions of interest by using the information from level 0 and the calorimeter. A total of 256 signals are sent into the level 1 trigger and 32 level 1 triggers are defined by taking and/or combinations of the signal. The calorimeter uses trigger towers ($\Delta\eta \times \Delta\phi = 0.2 \times 0.2$) that extend down to $|\eta| < 4$. Events are selected depending on whether a specified number of trigger towers pass transverse energy thresholds. The level 1 trigger reduces the rate from 10^5Hz to approximately 200 Hz in less than 3.5μs. If a

particular trigger is occurring at too high a rate, a prescale must be used at level 1. A prescale factor of n allows only 1 of every n events which passes the level 1 trigger to continue on to the level 2 trigger, thereby reducing the rate.

3.5.3 Level 2

The level 2 trigger is a software trigger and controls the final data to be written to tape. The level 2 trigger consists of a farm of 48 vax workstations which process each event with indepth computer algorithms. The processing time at level 2 is less than 200 ms, reducing the rate by a factor of 100, giving a final rate of $\sim$ 2 Hz written to tape.

Figure 3.9

Schematic of the trigger system.

4. Data Analysis

4.1 Experimental Definition of Jets

In 1990 at the Snowmass conference in Colorado, standardized jet algorithms were proposed to allow different experiments to directly compare experimental results. These jet algorithms are known as the Snowmass accord [19]. Later, it was discovered that the Snowmass accord created discrepancies between the direction of the parent parton and the direction of the reconstructed jet at high η. To remove these discrepancies, DØ introduced a different algorithm to define the reconstructed jet's center, (η_{jet},ϕ_{jet}).

The process of reconstructing jets consists of a series of iterative processes. First, towers containing 1.0 GeV or more are used as seed towers for finding preclusters, which are formed by adding neighboring towers within a radius of $R_{\eta\phi} = 0.3$ to seed towers. We define $R_{\eta\phi}$ as

$$\sqrt{(\eta_{jet} - \eta_t)^2 + (\phi_{jet} - \phi_t)^2} \leq R_{\eta\phi} \tag{4.1}$$

where (η_t,ϕ_t) is the center of a calorimeter tower. The η of each tower is calculated with respect to the interaction vertex, which is determined from the tracking system.

Next, a fixed cone radius $R_{\eta\phi}$ is drawn around each precluster centered at (η_{jet}, ϕ_{jet}). For historical reasons, a new jet center (η_{jet}, ϕ_{jet}) is then calculated using

the Snowmass accord.

$$\eta_{Snowmass} = \frac{\sum_i E_{Ti}\eta_i}{\sum_i E_{Ti}} \tag{4.2}$$

$$\phi_{Snowmass} = \frac{\sum_i E_{Ti}\phi_i}{\sum_i E_{Ti}} \tag{4.3}$$

where the sum over i is over all towers that are within the jet radius $R_{\eta\phi}$.

Using this new jet center, this process is then repeated until a stable jet center is found. After a stable jet center is found, η_{jet} and ϕ_{jet} are recalculated using the DØ algorithm for determining η_{jet} and ϕ_{jet}.

$$\eta_{jet} = -ln(tan(\theta_{jet}/2)) \tag{4.4}$$

$$\phi_{jet} = tan^{-1}\frac{\sum_i E_{yi}}{\sum_i E_{xi}} \tag{4.5}$$

where

$$\theta_{jet} = tan^{-1}\frac{\sqrt{(\sum_i E_{xi})^2 + (\sum_i E_{yi})^2}}{\sum_i E_{zi}}$$

$$E_{xi} = E_i sin(\theta_i) cos(\phi_i)$$

$$E_{yi} = E_i sin(\theta_i) sin(\phi_i)$$

$$E_{zi} = E_i cos(\theta_i)$$

The transverse energy of a jet is defined as the sum of the transverse energy within each calorimeter tower ($.1 \times .1 = \Delta\eta \times \Delta\phi$) which is located within the jet cone.

$$E_{Tjet} = \sum_i E_{Ti}$$

$$E_{Ti} = E_i sin(\theta_i)$$

After the preliminary set of pre-jets has been found, overlapping pre-jets can be merged into a single jet or the energy apportioned to two individual jets (~5% of jets are merged and ~30% are split). Two pre-jets are merged into one jet if more than 50% of the lower energy pre-jet's E_T is contained in the overlap region. The center of the new jet is defined as the vector sum of the original two pre-jet centers, and the energy of the merged jet is the sum of the energy of the original two pre-jets. If less than 50% of the lower energy pre-jet's E_T is contained in the overlap region, the jets are classified as split. In this case, the energy of each cell in the overlap region is assigned to the nearest jet, and the jet directions are recalculated.

4.2 Experimental Measurement of Jet Shape

Jets are found using the fixed cone algorithm described earlier with radius $R_{\eta\phi} = 1.0$. To study the internal structure of jets by measuring the transverse energy flow, the jet cone is divided into 10 subcones around the jet axis with sizes varying from r=0.1 to r=1.0 in Δr=0.1 increments.

There are many different possible definitions for the jet shape. One possible definition is the energy density in each subcone. However, the energy density changes by over two orders of magnitude, so small changes in the jet shape are difficult to measure. Another possible definition of the jet shape is the fraction of energy within each subcone. Other experiments have measured the jet shape, and have defined it to be the integrated fraction of transverse energy within each cone of radius r. In order to more easily compare results to previous measurements, we use this definition. The

jet shape, $\rho(r)$, is defined as the integrated fraction of the transverse energy within a cone of radius r.

$$\rho(r) = \frac{\sum_{x=0}^{r} E_T(x)}{\sum_{x=0}^{1} E_T(x)} \tag{4.6}$$

The transverse energy in each subcone is obtained by adding the transverse energy of all calorimeter cells whose center is located within the subcone boundary.

As discussed is chapter 3, the basic structure of the calorimeter is a projective tower containing 10-12 longitudinal layers of individual readout cells. The towers are projective from a vertex at z=0, the center of the interaction region. Any jet vertex away from the origin can have some cells within a tower be outside the jet cone, while others will be inside. Due to the large data sample available, the event vertex was restricted. This simplifies the analysis because if a tower is contained a jet, so are all of its cells. Figure 4.1 shows the E_T found using only those cells contained within a jet divided by the E_T found using towers as the basic measuring element. As can be seen in figure 4.1, there is at most a 1% difference in the measured energy. Due to pedestal subtraction, a calorimeter cell can contain negative energy, allowing figure 4.1 to have values greater than 1.

4.3 Triggers

Four different triggers were used for this analysis called Jet Low, Jet Medium, Jet High and Jet Max. The level 1 and level 2 trigger thresholds for each trigger are listed in Table 4.1. Also listed in the table is the range of E_T found using offline reconstruction, where each trigger is greater than 95% efficient. Both the level 2 E_T

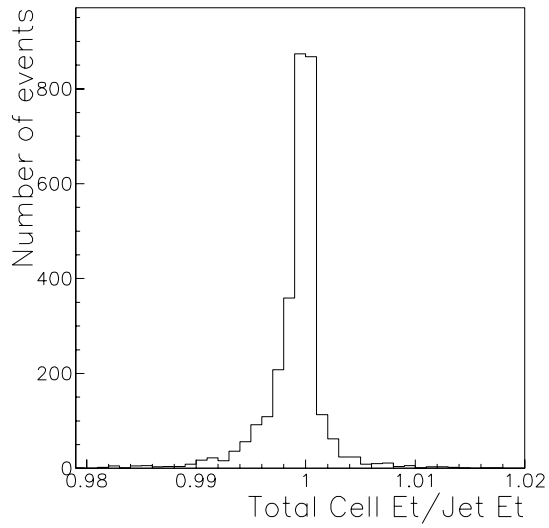

Figure 4.1

The transverse energy contained within the cells of a jet divided by the jet E_T for events within $\pm$ 30 cm of the detector's center.

threshold and the offline E_T are for jets reconstructed with a cone of $R_{\eta\phi} = 0.7$. For the level 1 thresholds column, the entry 2 towers $\times$ 7 GeV refers to the requirement of 2 trigger towers each with energy above 7 GeV. A trigger tower ($\Delta\eta \times \Delta\phi = 0.2 \times 0.2$) consists of any four adjacent standard calorimeter towers ($\Delta\eta \times \Delta\phi = 0.1 \times 0.1$).

4.4 Data Sample and Cuts

The data were taken during the 1992-1993 run of the Tevatron where approximately 14 pb^{-1} of data were accumulated. Approximately $3pb^{-1}$ of data provided adequate statistics for this study. Certain cuts were placed on the data which depended upon the general features of the event while others depended on the features

Table 4.1

Triggers Used in Jet Shape Analysis
(All triggers were prescaled except for Jet Max)

Trig Name	L1 threshold	L2 threshold GeV	Efficient at GeV	Energy Range GeV
Jet Low	1 tower $\times$ 7 GeV	30	45	45-70
Jet Medium	2 towers $\times$ 7 GeV	50	70	70-105
Jet High	3 towers $\times$ 7 GeV	80	105	105-140
Jet Max	4 towers $\times$ 5 GeV	115	140	140-

of the jets within the event.

4.4.1 Trigger Cuts

The first cuts, trigger cuts, placed on the data depend upon the global features of the event. In this study of jet shape, it is essential that the E_T distribution of the jets is not biased by the triggers used to accumulate the data. There are three possible biases that can arise from the trigger. The first is due to the trigger efficiency variation with E_T. If a trigger varies in E_T, the jets which trigger the event will typically be narrower, biasing the jet shape. The second possible bias is due to the number of trigger towers required for each trigger. For example, the Jet Medium trigger requires 2 trigger towers. It could be that extremely narrow jets, filling one trigger tower, fail the trigger. This would introduce a bias. The third possible bias is due to the fact that individual jets are being studied in this analysis while the triggers are dependent upon the topology of the entire event.

To remove these possible trigger biases, the offline measured E_T value of the leading jet in the event was required to be in the 95% efficiency range for one of the triggers which fired. The trigger efficiency was determined by analyzing the data offline with a jet cone size of $R_{\eta\phi}$=0.7. To verify that no trigger biases are present, the jet shape was measured with small samples in an overlapping E_T region with two separate triggers. Measuring the jet shape in the same E_T region with two different triggers allows us to determine if any trigger biases are present. A trigger dependence on the jet shape would indicate a trigger bias. The difference in the jet shape due to different triggers was found in each E_T region used in this analysis. Figure 4.2 shows the difference in jet shape for one particular E_T region. The differences in the jet shapes due to different triggers were all measured to be consistent with zero, indicating that no trigger biases were present for the energy and η regions used in this analysis.

Another trigger related bias which can occur arises due to prescaling the data. The jet cross section is a rapidly falling distribution, so many more low energy jets are produced than high energy jets. In order to collect a large sample of high energy jets, each of the three low energy jet triggers had a different prescale value. Simply allowing events from different triggers to populate a particular E_T interval without regard to their scaling factor would bias the jet shape. This bias is caused by an incorrect jet energy spectrum being used to populate the different E_T intervals. To remove this bias, events from a given trigger were allowed to populate only one E_T interval.

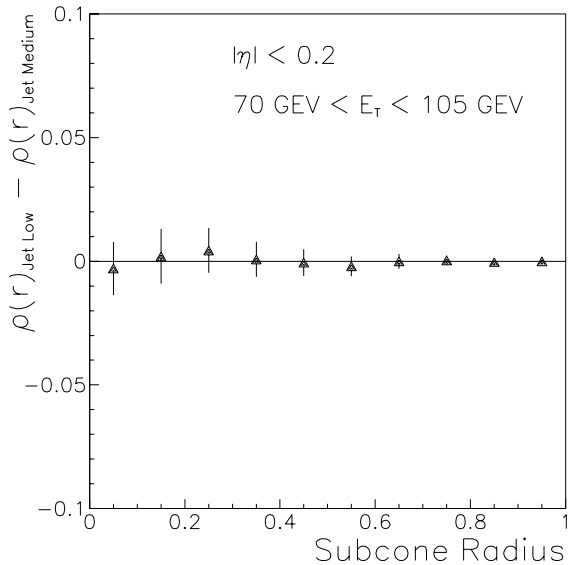

Figure 4.2

The difference $\rho(r)_{Jet\ Low} - \rho(r)_{Jet\ Medium}$

4.4.2 Vertex and Missing E_T cut

Two additional cuts were applied to the global event, a vertex cut and a missing E_T cut. The first, a vertex cut of $\pm$ 30 cm around z=0 was required in order to keep the calorimeter towers projective. The second is a missing E_T cut. Any missing E_T in the event is due to the energy resolution of the calorimeter, neutrinos or hot cells. In hadronic events, typically the missing E_T due to neutrinos is small. As can be seen from equation 3.3, the missing E_T due to jet energy resolution increases as the E_T of the leading jet in an event increases. Simply applying a cut on the missing E_T in an event would cause an inefficiency for good events containing jets with large E_T. Therefore, to remove hot cells and keep efficiency for high E_T jets, a cut requiring that the missing E_T in the event be less than $0.7 \times E_T$ of the leading jet was applied,

shown in Figure 4.3.

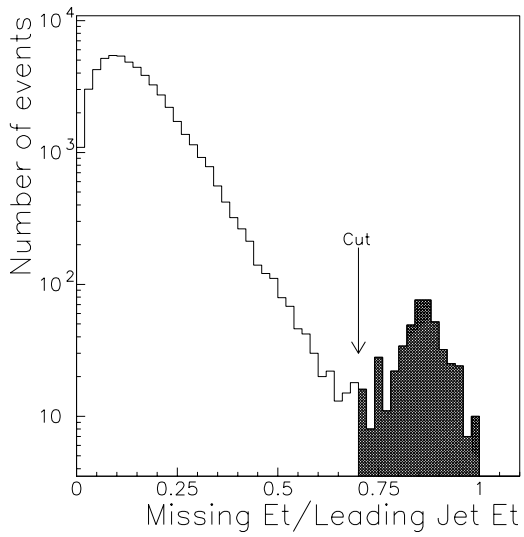

Figure 4.3

The missing E_T in an event divided the leading jet E_T. The shaded region is due to events with hot cells.

4.4.3 Jet Quality Cuts

Once an event was accepted as a candidate, additional quality cuts were placed on each individual jet [20]. The cuts designed to remove fake jets caused by hot cells and spent particles from the main ring are:

- $0.05 \leq$ EM Fraction ≤ 0.95
- Cell Ratio ≤ 10
- CH Fraction ≤ 0.4

Where the EM Fraction is the fraction of the jet energy contained in the electromag-

netic layers of the calorimeter. The Cell Ratio is the ratio of the most energetic cell in the jet cone to the second most energetic cell, and the CH Fraction is the fraction of the jet energy contained in the coarse hadronic layers of the calorimeter.

Hot cells typically are a single cell containing all of the jet energy. A cut on the EM fraction eliminated false jets due to a single hot cell containing all of the towers energy. If a hot cell is located in the electromagnetic sector, the EM fraction will be ~ 1, while if a hot cell is located in the hadronic layers, the EM fraction will be ~ 0. A single hot cell will also cause the Cell Ratio $>> 1$. The main ring at Fermi Lab passes directly through the coarse hadronic layer of the calorimeter. Energy depositions in the calorimeter due to spent particles from the main ring will be mostly hadronic, motivating the third jet quality cut.

4.4.4 η cuts

The region between the barrel calorimeter and the end calorimeters, known as the inter-cryostat region has a relatively poor resolution, so including this region in the analysis could affect the jet shape. Restrictive η cuts were designed to keep the edges of the jets away from the inter-cryostat region. The detector geometry was designed assuming the interaction point at z=0. Assuming this interaction point, the η for each jet is defined as $\eta_{detector}$. To obtain the true η of a jet, the true event vertex, which can vary by $\pm$ 30 cm, must be taken into account. In order to keep the edges of the jet from overlapping the inter-cryostat region ($\sim 1.3 \leq |\eta_{detector}| \leq 1.7$), it was simpler to choose a cut on $\eta_{detector}$ instead of η.

A cut using $\eta_{detector}$ was chosen because a jet centered at η of 0.2 with a vertex of z=30 cm corresponds to $\eta_{detector}$ of 0.5. A jet located at 0.5 $\eta_{detector}$ would overlap the inter-cryostat region. A more restrictive 10 cm vertex cut would remove much of this overlap but reduce statistics unacceptably.

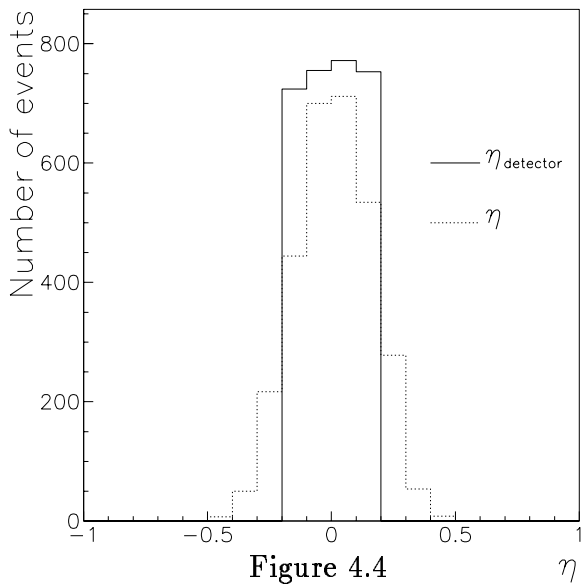

Figure 4.4

Comparing η and $\eta_{detector}$ for centrally located jets.

Because of the desire to avoid the inter-cryostat region, jets were analyzed in two different regions, a central region centered at $|\eta|$=0, and a forward region centered at $|\eta| \sim 2.7$. Figures 4.4 and 4.5 show both the η and $\eta_{detector}$ of jets used in this analysis.

Because of the restrictive vertex cut designed to take advantage of the calorimeter's projective geometry, there is only insignificant differences between measurements

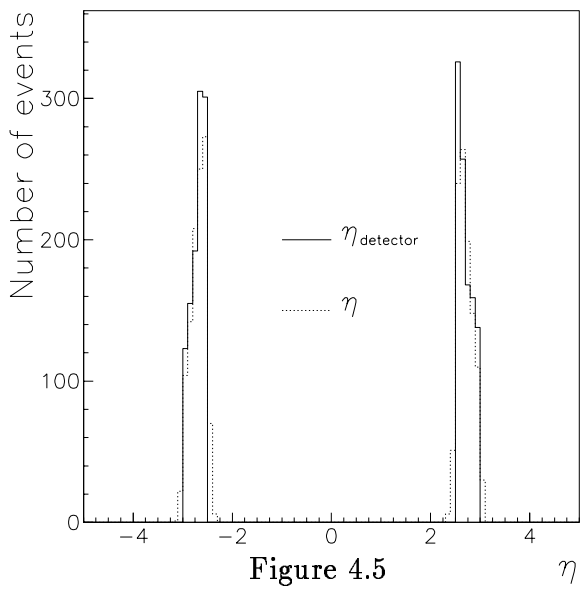

Figure 4.5

Comparing η and $\eta_{detector}$ for jets located in the forward region.

made using $\eta_{detector}$ and the true η of a jet. To show the difference of cutting on $\eta_{detector}$ instead of η, the jet shape was measured using $|\eta| \leq 0.2$ with a vertex cut of 10 cm and $|\eta_{detector}| \leq 0.2$ with a vertex cut of 30 cm. The difference in the two jet shapes, shown in figure 4.6, is consistent with zero, indicating no shape differences. The analysis was greatly simplified by working with the variable $\eta_{detector}$ instead of η.

4.5 Corrections to the Data

The jet energies must be corrected due to the effects of calorimeter response, the hardware pedestal cut, and spectator interactions. The calorimeter response correction was performed by using the standard DØ jet correction algorithm [21], which is composed of three related steps. First, the electromagnetic layers of the calorimeter are calibrated using $Z \rightarrow e^+e^-$ constrained by the measured LEP value

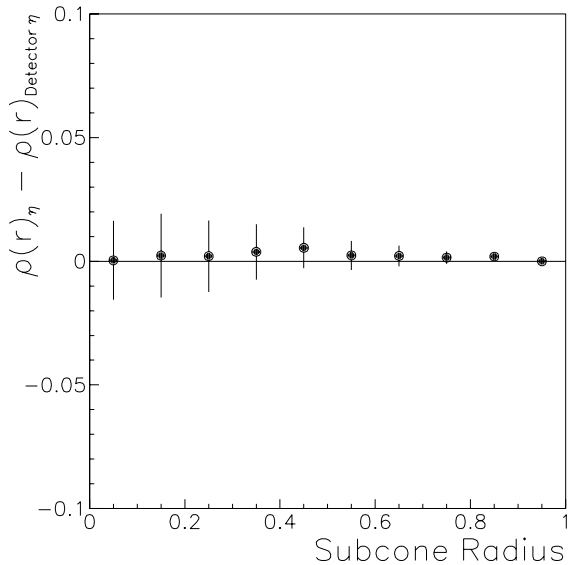

Figure 4.6

The difference in jet shape when cutting on $\eta_{detector}$ and η.

found for the Z mass. Second, after the electromagnetic layers are calibrated, the hadronic sections of the calorimeter are calibrated to the electromagnetic layers of the calorimeter using a process called the missing E_T projection fraction (F_{MPF}). This calibration assumes that the missing E_T in an event, $\not{E}_T$, is dominated by the mismeasurement of the jet energy. The hadronic section in the central calorimeter is compared to the electromagnetic layers. Events are studied which contain a hadronic jet balanced by a single isolated photon. The variable F_{MPF} is defined as

$$F_{MPF} = \frac{\not{E}_T \bullet \hat{n}_{photon}}{E_{T photon}} \tag{4.7}$$

where $\hat{n}_{photon}$ is the photon's direction unit vector. The total hadronic jet energy

must then be corrected by the calorimeters response R,

$$R = 1 + F_{MPF}. \tag{4.8}$$

Finally, after the central calorimeter has been calibrated, the forward regions are calibrated to the central region. This is performed through E_T balancing, by comparing boosted di-jet events in which one centrally located jet is balanced by a jet located in the end calorimeter. This calibration procedure was performed using jets with a cone radius of 0.7. However, the method is only weakly sensitive to cone size. A 1-2% systematic energy difference was found when varying the cone size between $0.7 < R_{\eta\phi} < 1.0$.

For this study, on an event by event basis the calorimeter towers were initially corrected uniformly as a function of energy which assumes a linear calorimeter response to particles within the jet. Assuming this linear response does not take into account the effects due the calorimeter's non-linearities. Test beam studies were only performed with particle energies greater than 2 GeV, so the response to particles with energy less than 2 GeV has not been measured. However, previous experiments have measured the response of similar type calorimeters to particles with energy less than 2 GeV [22]. These results indicate that the relative response to pions with energy less than 2 GeV decreases with decreasing pion energy. At very low energies, pions lose almost all of their energy through ionization, causing the relative response to become constant. To understand the size of possible systematic effects caused by the calorimeter's non-linearities different response curves were simulated in Monte Carlo.

Figure 4.7 shows the three different response curves studied, along with the measured calorimeter response for test beam pions and electrons [23].

Response curves A are fits to the measured pion and electron test beam responses. Response curve B is a curve between linearity and the measured response. Curve C assumes a linear response. Figure 4.8 shows a Monte Carlo study of the effects on the jet shape for the three different calorimeter response curves.

The response of the calorimeter depends upon the energy of the each individual particle within a jet. Because the energy of the individual particles within a jet is unknown, the response for each particle is unknown and assumed to be linear. This introduces an error since particles of varying energies comprise a jet. The difference in the jet shape using response curve C, and response curve A is an estimate of the correction required to remove the effects of the calorimeter's non-linear response to low energy particles. The difference in the jet shape between curve B and response curve A is a measure of the systematic error to be assigned due to uncertainty in the calorimeter's non-linear response. The total data is corrected for the calorimeter non-linear response using a full simulation Monte Carlo with hadronic showering modelled using a detector simulator. This will be discussed in detail later.

In addition to the jet energy deposited from the fragmentation of the hard scattered partons in collisions at DØ, there are two additional sources of energy which overlays an event. The first, due to the detector, occurs even in the absence of a particle flux, and is due to the decay of uranium atoms, the electronic shaping technique and the hardware pedestal cut. The second correction, known as the underlying event,

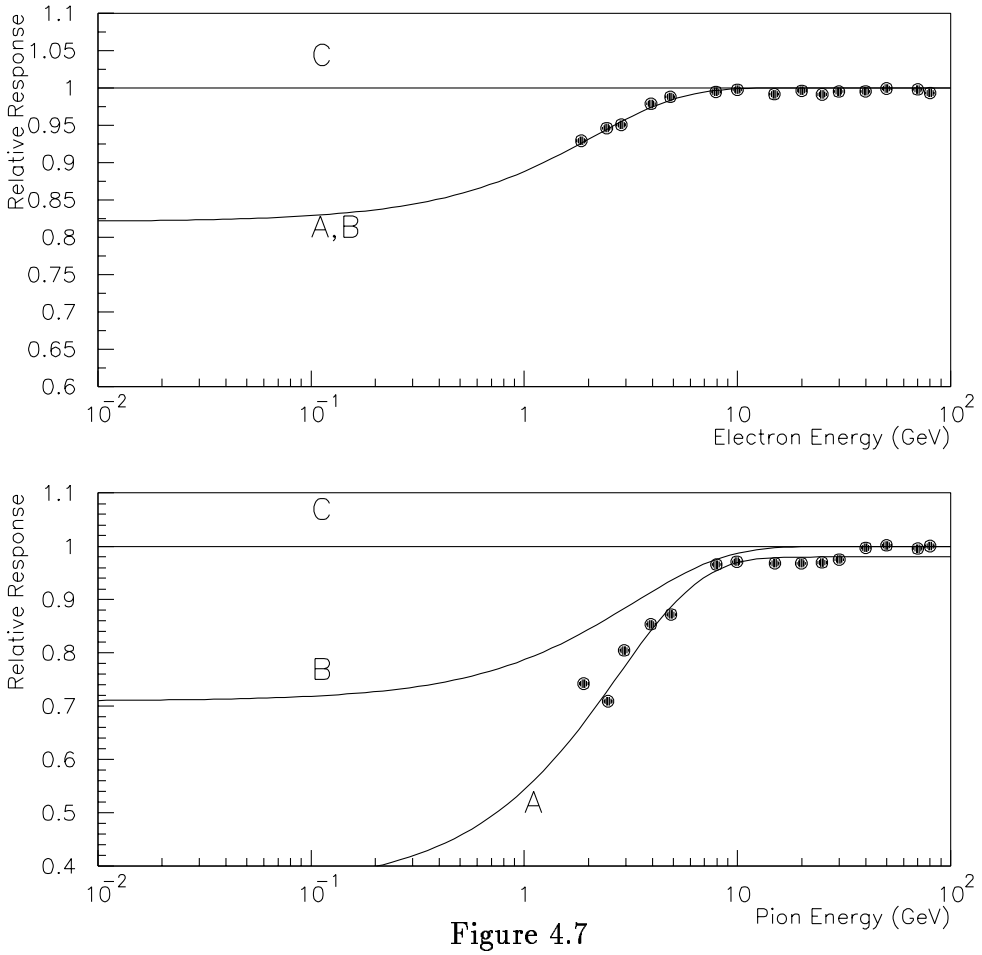

Figure 4.7

A, B and C represent the three different response curves studied within Herwig and the circles are the measured calorimeter response from test beam.

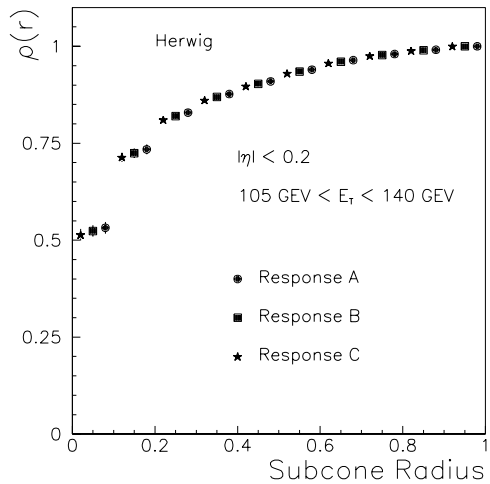

Figure 4.8

The effects on the jet shape for the three different response curves simulated in Herwig. The points are separated along the x-axis to allow the response effects to be seen.

is due to interactions amongst the spectator partons, those which do not participate in the hard scattering but scatter energy into the detector.

The energy contributions due to the underlying event and detector effects were measured using a single minimum bias run. The transverse energy due to the underlying event was found to be constant in η and ϕ with a measured value $\frac{dE_T}{d\eta d\phi} = 0.55\pm$ 0.1 GeV. The energy due to the detector effects was parameterized to be constant in η and ϕ with a value $\frac{dE}{d\eta d\phi} = 1.36\pm$ 0.2 GeV.

Since the energy due to the underlying event is constant in E_T, the amount of transverse energy in each subcone due to spectator interactions is simply the product: ($\frac{dE_T}{d\eta d\phi}\times$ subcone area). As the number of multiple interactions increases, the energy deposited in the calorimeter due to spectator interactions also increases. To remove

this extra energy, the underlying event correction was doubled if a multiple interaction occurred.

The energy due to the detector effects, however, must be treated differently because it is a constant in energy, not E_T. In order to determine the amount of transverse energy due to these effects an integration over η and ϕ within each subcone must be performed.

Because of the large number of cells in the calorimeter, the data is not readout unless the absolute value of the energy in each cell is greater than 2 $\times$ the pedestal width, σ. This means a cell can record a negative energy value because the average value of the pedestal has been defined as zero within the hardware. Mathematically, before data suppression the pedestal distribution is composed of three parts, whose sum on average is zero.

$$N_{-2\sigma}E_{-2\sigma} + N_{2\sigma}E_{2\sigma} + N_{+2\sigma}E_{+2\sigma} = 0 \tag{4.9}$$

Where $E_{-2\sigma}$, $E_{2\sigma}$, and $E_{+2\sigma}$ are the average energy of the calorimeter cells within each interval, and $N_{-2\sigma}$, $N_{2\sigma}$, and $N_{+2\sigma}$ are the average number of calorimeter cells within each interval for a sample of minimum bias events, see Figure 4.9.

Without the hardware suppression, the uranium noise on average would not contribute energy to the measurement. However, due to the decay of the uranium and the electronic shaping technique, the pedestal distribution is asymmetric about zero, so after each cell is hardware suppressed, on average there is a net positive signal remaining. The data must be corrected for this effect.

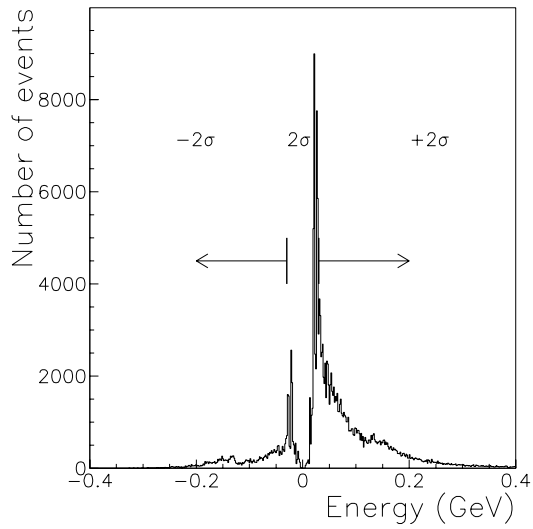

Figure 4.9

Energy distribution of calorimeter cells for a sample of minimum bias events. The 2σ region has been set to zero in hardware before being readout.

This hardware data suppression sets all calorimeter cells within $\pm 2\sigma$ of the pedestal to zero, forcing $E_{2\sigma} \equiv 0$ at readout. After suppression the pedestal distribution contributes on average a net energy to each cell. Equation 4.9 now becomes

$$N_{-2\sigma}E_{-2\sigma} + N_{+2\sigma}E_{+2\sigma} = \frac{dE}{d\eta d\phi} = -N_{2\sigma}E_{2\sigma}. \tag{4.10}$$

Before suppression it is found that $E_{2\sigma} < 0$, so in effect the zero suppression unphysically raises the jet's energy. One can think of zero suppression as artificially adding positive energy to each suppressed cell in order to increase each suppressed cell's energy to 0.

The amount of pedestal energy to be subtracted from a given jet depends upon the energy distribution of the cells within the jet. Consider a jet of energy E_{jet} in which all cells within the jet contain sufficient energy such that no cells are suppressed. The

measured jet energy, $E_{measured}$, is

$$E_{measured} = E_{jet} + N_{-2\sigma}E_{-2\sigma} + N_{2\sigma}E_{2\sigma} + N_{+2\sigma}E_{+2\sigma} \tag{4.11}$$

which by equation 4.9 yields

$$E_{measured} = E_{jet}. \tag{4.12}$$

In other words, no pedestal suppression has occurred so no correction is necessary for these cells.

On the other hand, if the jet contains $M_{2\sigma}$ cells which have been suppressed, the measured jet energy is

$$E_{measured} = E_{jet} - M_{2\sigma}E_{2\sigma}. \tag{4.13}$$

Which by equation 4.10 yields on average $E_{measured} > E_{jet}$, so energy must be removed.

Equation 4.10 shows that the average energy remaining after suppression depends upon the number of cells , $M_{2\sigma}$, that have been hardware suppressed. The number of suppressed cells must be taken into account when removing the energy caused by the hardware pedestal suppression. There are two methods available to remove the effects of the hardware suppression. The first is to correct each jet on an event by event basis. The number of suppressed cells within a jet can be measured and a correction can be applied to each jet.

A second method, and the technique used in this analysis, is to measure the average number of cells suppressed for a given sample as a function of E_T and η and then apply this average correction to each jet. For this method, the average number

of cells suppressed in both the hard scatter data and the minimum bias sample was compared.

The fraction of cells with energy outside the suppression value for a sample of minimum bias events is shown in Figure 4.10. The fraction of cells not suppressed in the minimum bias data is approximately 4% in the central region and 7% in the forward region.

The percentage of cells in a hard scatter event with energy outside the suppression value is shown in Figure 4.11. The fraction of cells not suppressed in hard scatter events is approximately 12% in the central region and approximately 15% in the forward region. The difference in the fraction of cells suppressed between the hard scatter data and the minimum bias sample is $\sim 8\%$.

The percentage of cells with energy outside the suppression value was also measured as a function of subcone. In the center of a jet, the percentage of cells with energy outside the suppression value can be greater than 80%, see Figure 4.12, so using the zero suppression value from the minimum bias sample introduces an error larger than the 15% error on the zero suppression value. Therefore, the zero suppression value was corrected for the percentage of cells suppressed within each subcone.

The transverse energy correction due the hardware data suppression can be written as:

$$\text{zero supp. correction} = \mathrm{A}(\eta, \mathrm{E_T}, \mathrm{r}) \int_{\text{subcone}} \frac{\mathrm{dE}}{\mathrm{d}\eta \mathrm{d}\phi} \frac{1}{\cosh\eta} \, \mathrm{d}\eta \, \mathrm{d}\phi \tag{4.14}$$

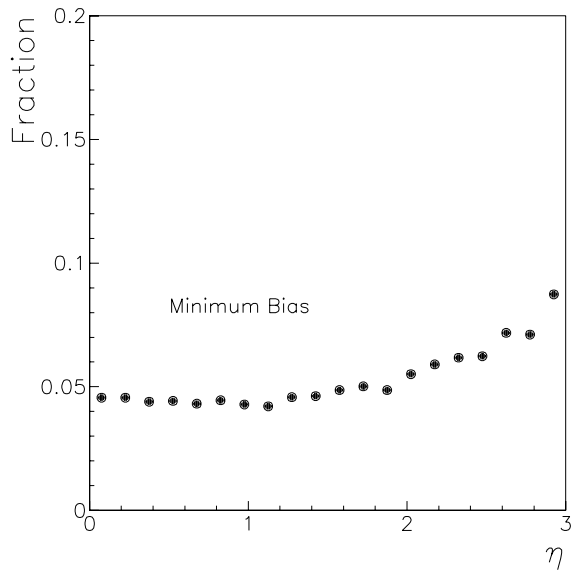

Figure 4.10

The fraction of cells within a cone radius $R_{\eta\phi} = 1.0$ with non-zero energy outside the hardware suppression value for a sample of minimum bias data vs η.

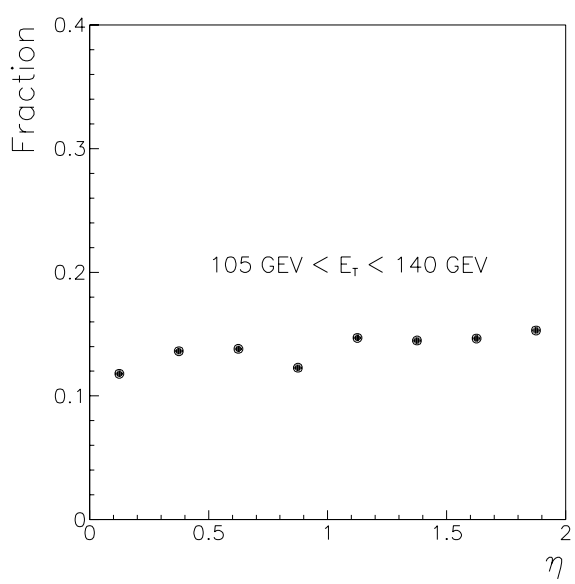

Figure 4.11

The fraction of cells within a cone radius $R_{\eta\phi} = 1.0$ with non-zero energy outside the hardware suppression value for jets between 105 and 140 GeV vs η.

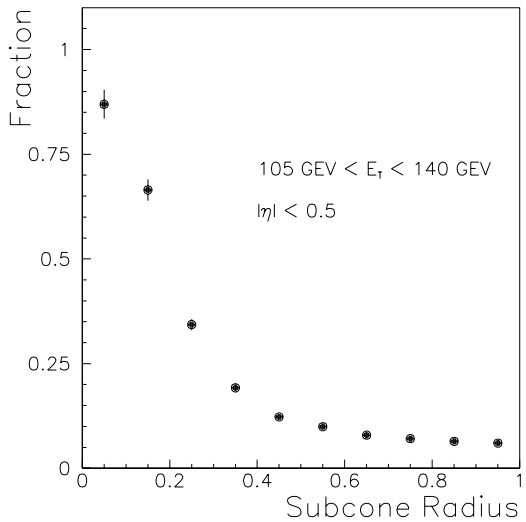

Figure 4.12

The fraction of cells with non-zero energy outside the hardware suppression value for jets between 105 and 140 GeV vs subcone radius.

where $A(\eta, E_T$,r) is a correction factor which takes into account the differences between the number of calorimeter cells suppressed between the minimum bias sample and the hard scatter data.

4.6 Systematic Errors

The systematic errors on the jet shape due to the underlying event, zero suppression and the jet energy scale corrections were found by varying each correction within their measured errors. The errors due to the uncertainty in the underlying event and zero suppression each give a maximum error, $\Delta\rho(r)$, of ~ 0.005 to any data point. A maximum error of $\Delta\rho(r) \sim 0.02$ to any data point, is due to the uncertainty in the jet energy scale. This error was determined by changing the jet energy within the

allowed errors of the jet energy correction. This error arises from jets moving from higher and lower energy regions into the region of interest.

The standard jet quality cuts are over 90% efficient[20], the exact value being a function of E_T and η. The $\sim$ 10% of jets which are removed by these cuts are primarily narrow jets, so applying the quality cuts biases the jet shape. To measure the effects on the jet shape due to applying the jet quality cuts, the jet shape was measured with a Monte Carlo simulation with and without the jet quality cuts. The quality cuts caused $\Delta\rho(r)$ to change by less than a 0.01 to any data point, so a maximum error of $\Delta\rho(r) = 0.01$ was assigned for using the jet quality cuts.

In the central region, the error due to the uncertainty in response to low energy particles is significant. This can cause a jet shape error $\Delta\rho(r)$ of $\sim$ 0.015 to any data point for jets with an energy between 45 and 70 GeV. As the energy of the jets increased, this error is reduced, causing a maximum error of $\Delta\rho(r) \sim 0.01$. This error is reduced to $\Delta\rho(r) \sim 0.005$ to any data point in the forward region. This error is smaller, because the energy of particles within the jets in this region is high, reducing the effects of the non-linear low energy calorimeter response.

These errors, due to the uncertainty in the underlying event, zero suppression, jet energy scale and the low energy response, along with the jet quality cuts biases, being independent of one another, were added in quadrature to the statistical errors to get the final total error on the jet shape.

4.6.1 Out of Cone Effects

Any jet energy not contained within the defined jet cone radius will bias our measurement of the jet shape, because the jet energy within each subcone is normalized to the total transverse energy contained within the defined radius of the jet. Energy outside the defined jet biases the jet shape narrow. Figures B.5 and B.9 show the energy density, $\frac{dE_T}{d\eta d\phi}$, for jets with transverse energy between 45 and 70 GeV as a function of the distance from the jet center for different η regions. Near a radius $R_{\eta\phi}$ = 1.0 the energy density is nearly constant, $\frac{dE_T}{d\eta d\phi} \sim 3$ GeV, and small compared to the energy density in the core, $\frac{dE_T}{d\eta d\phi} \sim 400$ GeV. Hence, very little jet energy is located outside the jet cone. Changing the jet radius $\Delta R_{\eta\phi} \sim 0.1$ caused a jet shape change of approximately $\frac{\partial \rho(r)}{\partial R_{\eta\phi}}|_{R_{\eta\phi}=1.0} < 0.8\%$.

Near a radius, $R_{\eta\phi} = 1.0$, the energy density in figure B.5 has a constant value of ~ 3 GeV. This energy has three sources. The first is the underlying event energy from the soft spectator interactions. The second is soft radiation from the hard scattering parton evolution process, and the third is from the hardware pedestal cut.

The energy underlying an event due to spectator interactions and the hardware pedestal cut can be measured using minimum bias events which are considered to be identical to the soft spectator processes. The measured value for the spectator interactions is $\frac{dE_T}{d\eta d\phi} \sim .55$ GeV, and the measured value for the hardware pedestal cut is $\frac{dE}{d\eta d\phi} \sim 1.36$ GeV. After subtracting this energy the remaining energy must be due to hard scatter processes and should not be removed when comparing to theoretical predictions. If this hard scatter energy was removed, the jet shape would change by

less than $\Delta\rho(r) < 0.03$.

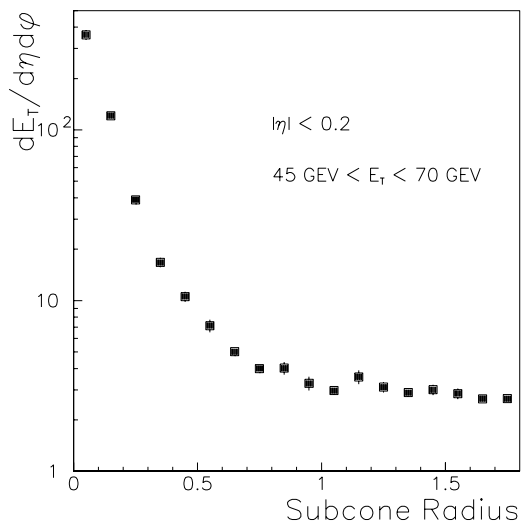

Figure 4.13

The transverse energy density, $\frac{dE_T}{d\eta d\phi}$, for central jets with transverse energy between 45 and 70 GeV.

4.7 Effects of the Calorimeter

The effects of the calorimeter on the jet shape must be removed in order to compare to theoretical predictions. Two properties of the calorimeter cause the jet shape to be biased.

The first is due to the calorimeter's non-linear response to low energy particles, shown in Figure 4.7, which will artificially narrow the jet shape. This narrowing occurs because the energies of particles within a jet decrease as the particles move further from the center of a jet, shown in Figure 4.15. As the energy of the particles

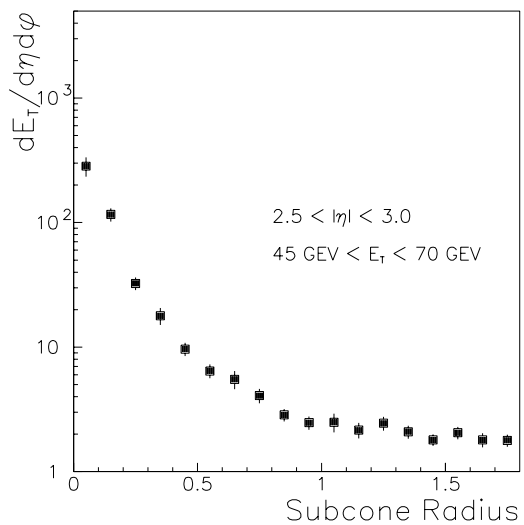

Figure 4.14

The transverse energy density, $\frac{dE_T}{d\eta d\phi}$, for forward jets with transverse energy between 45 and 70 GeV.

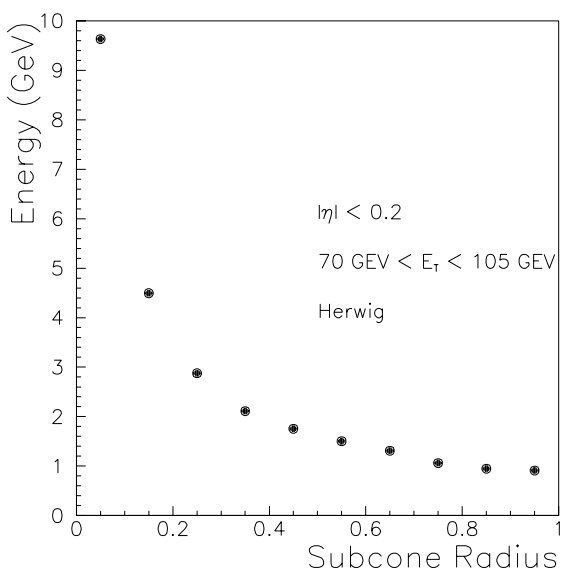

Figure 4.15

The average energy of particles within each subcone vs subcone radius.

decreases, the response is less linear, causing less energy to be measured at the edge of a jet. As less energy is measured at the edge of a jet, the jet shape will be biased narrow.

The second calorimeter bias is caused by the showering of particles within the calorimeter. Showering effects will widen the jet shape because the energy of a particle that strikes the calorimeter in a particular subcone will shower over many subcones. The effects due to showering should be much more pronounced in the forward region than in the central region because showering effects are not η invariant. The shower size within the calorimeter in physical space for two particles with the same energy is the same in both the central and forward regions. However, a calorimeter cell is a constant size in $\eta - \phi$ space, making the physical size of a calorimeter cell smaller in the forward region than in the central region. For this reason, a particle striking the calorimeter in the forward region will shower over many more calorimeter cells than a centrally located particle. The more calorimeter cells that are within the shower, the larger the correction needed due to showering.

To determine the showering correction of the calorimeter on the jet shape, an analysis was performed using Herwig[24], Isajet[25] and Pythia[26] Monte Carlo simulations with GEANT[27] calorimeter modelling. In the central region, Isajet(7.0), Herwig(4.6) and Pythia(5.6) were studied, while in the forward region, Isajet(7.06) and Herwig(5.6) were examined.

Three different Monte Carlo simulations were used in order to study the variation of the calorimeter corrections on the exact fragmentation scheme used by the various

Monte Carlos. Isajet uses a fragmentation scheme in which quarks and gluons are fragmented independent of one other. Herwig uses a clustering fragmentation scheme in which quarks are connected by color strings and intermediate colorless structures are formed between the quarks. These colorless clusters then emit partons which can then form new intermediate colorless structures. The main fragmentation option in Pythia is the Lund string scheme. Quarks are connected by a color string and this color string emits partons which can then connect to other colored objects.

In order to directly compare collider data and the Monte Carlo simulations, all of the same cuts and corrections were applied to the Monte Carlo simulations. However, the effects of the hardware pedestal suppression were not modelled.

It is important that the simulations reproduce the jet shape accurately, since the calorimeter effects depend on the distribution of energy within a jet. Figures 4.16-4.19 compare the jet shape measured for both collider data and the three different Monte Carlo simulations in the central region. The Herwig simulation contained the full spectrum of jet energies and describes the data well for all energies. Both the Isajet and Pythia events available* did not contain the full jet spectrum, but rather a specialized subset consisting of at least three jets with a leading jet between 90 and 180 GeV. Since the jet spectrum in Isajet and Pythia is not accurately represented, it is not expected that these simulations would describe the data accurately. However, having a disagreement between collider data and the Monte Carlo simulations allows

*It can take many months of computer time to generate a large sample of Monte Carlos events, so the Monte Carlos events available were studied.

us the determine how accurately the simulations must model the data, while at the same time it determines an estimate of the systematic error due to using the Monte Carlo to correct the data.

Figures 4.20 and 4.21 compare collider data to the Monte Carlos in the forward region. Both the Herwig and Isajet simulations contained the full jet spectrum in the forward region and both describe the data reasonably well. But, differences in the jet shapes occur between the two simulations which allow us to measure the importance of fragmentation models in determining the calorimeter corrections in the forward region.

Using these simulations, the calorimeter biases on the jet shape were determined by first measuring the jet energy flow using the fragmented particles. The jet effects of the calorimeter were then determined by using the detector simulator GEANT and measuring the energy flow using the calorimeter cells. The difference between the jet shape found using the particles directly and the shape found using the calorimeter cells was formed. These differences are the additive calorimeter correction factors necessary to remove the effects of the calorimeter on the experimental data. The calorimeter correction factors were chosen to be additive instead of multiplicative in order to minimize any shape and renormalization differences in the Monte Carlo simulations. After the effects of the calorimeter have been removed, the transverse energy flow is referred to as the "particle level" jet shape.

Figures 4.22 and 4.23 show the differences between the jet shape before and after simulation in the calorimeter. For central jets the effects of showering are small, and

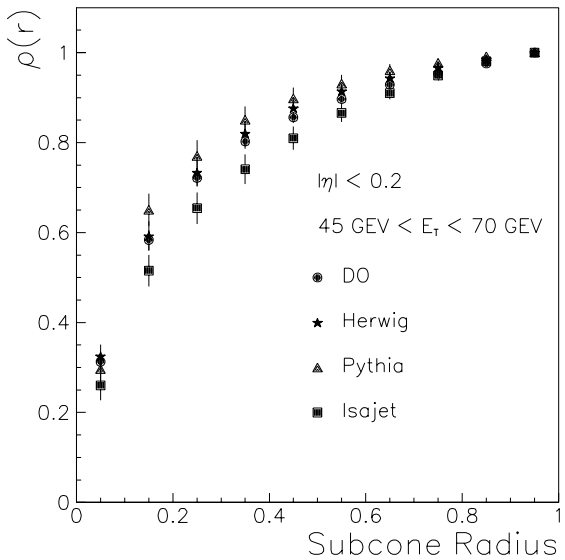

Figure 4.16

Comparing data to three different Monte Carlo simulations in the central region for jets with transverse energy between 45 and 70 GeV.

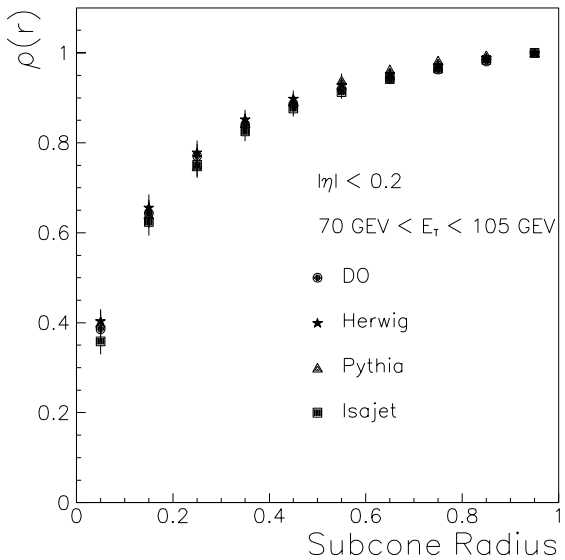

Figure 4.17

Comparing data to three different Monte Carlo simulations in the central region for jets with transverse energy between 70 and 105 GeV.

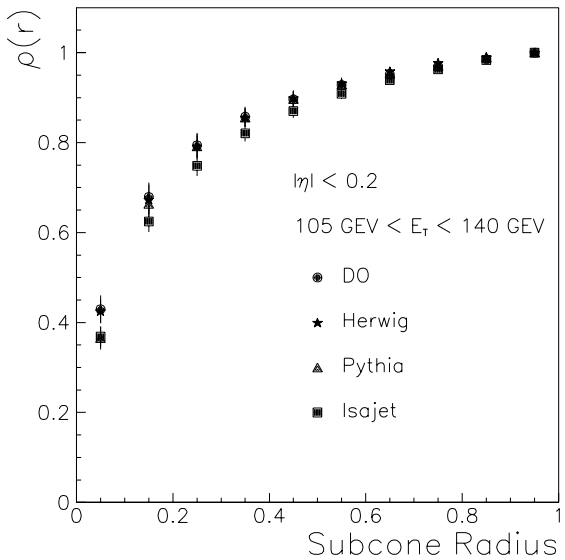

Figure 4.18

Comparing data to three different Monte Carlo simulations in the central region for jets with transverse energy between 105 and 140 GeV.

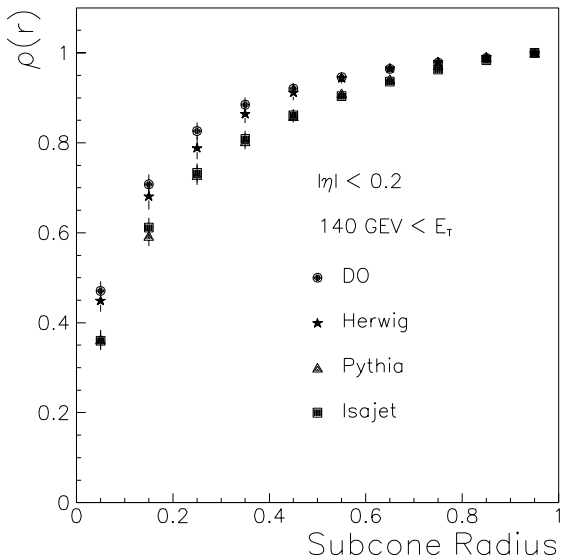

Figure 4.19

Comparing data to three different Monte Carlo simulations in the central region for jets with transverse energy greater than 300 GeV.

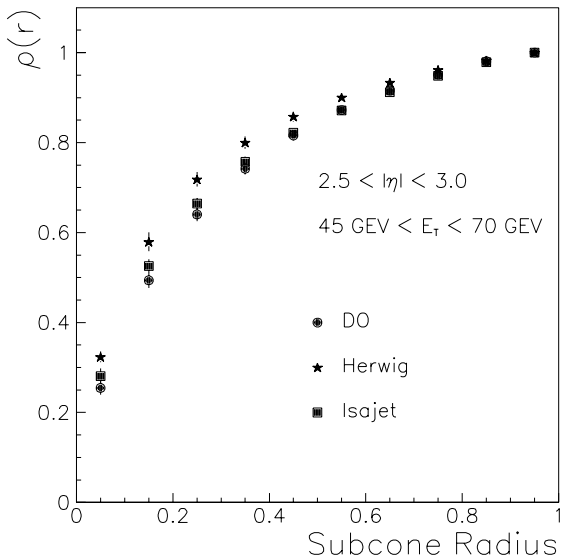

Figure 4.20

Comparing data to two different Monte Carlo simulations in the forward region for jets with transverse energy between 45 and 70 GeV.

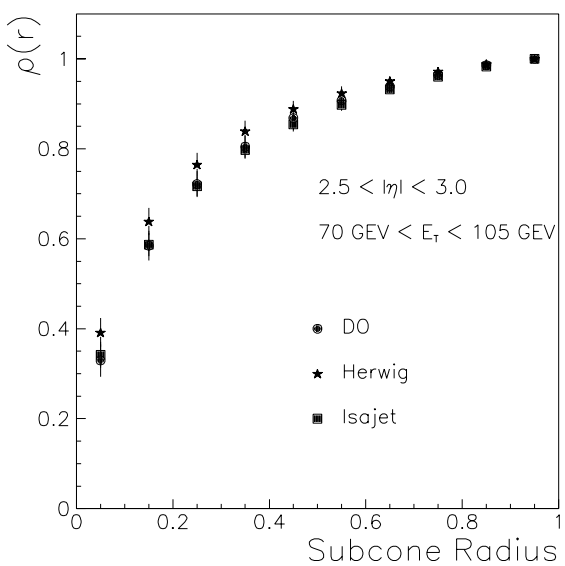

Figure 4.21

Comparing data to two different Monte Carlo simulations in the forward region for jets with transverse energy between 70 and 105 GeV.

only a small correction, typically $\Delta\rho(r) \sim 0.08$, was applied to the first subcone to remove calorimeter biases. In the forward region, the effects of showering require a large correction, typically $\Delta\rho(r) \sim 0.28$ to the first subcone.

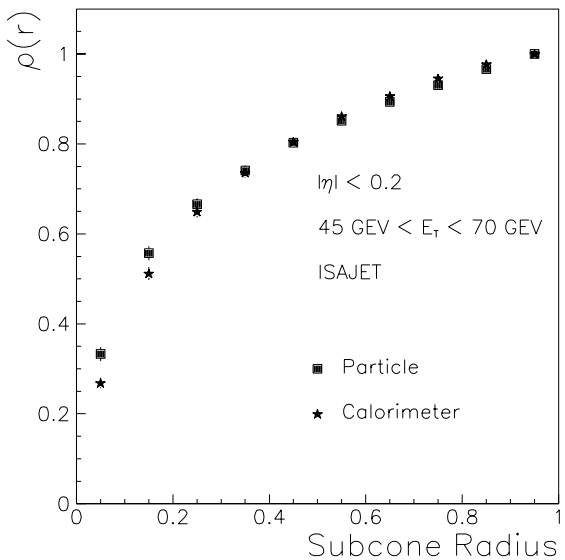

Figure 4.22

The particle level jet shape before and after calorimeter biases for central jets.

The accuracy of the calorimeter correction factors depend on two issues, how well the detector is simulated and the accuracy of the fragmentation models. To determine how well the detector is simulated two different calorimeter models were used. The first used the full plate level geometry which precisely simulates all the known material within the calorimeter. This approach has been shown to describe single pion showering accurately [28]. The second uses a mixture level geometry,

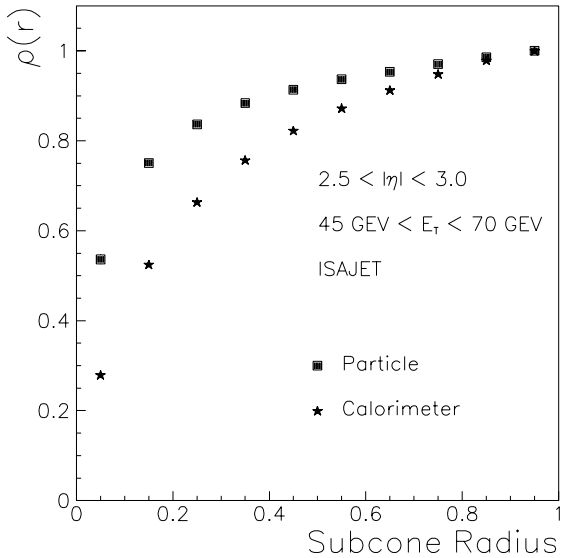

Figure 4.23

The particle level jet shape before and after calorimeter biases for forward jets.

which uses material densities averaged over different $\eta - \phi$ slices. Figure 4.24 shows the difference between the additive correction factors obtained for the central region for the two different calorimeter geometries. Both geometries gave similar results. In order to greatly reduce computational time, the second geometry was chosen.

The exact choice of fragmentation models on the jet shape is relatively small. The three Monte Carlo simulations each have different fragmentation schemes, yet the jet shape is affected only $\Delta\rho(r) \sim 0.03$. We take this to be the systematic error due to the Monte Carlo.

All of the corrections applied to the data for both the central and forward regions are shown in Appendix A.

Although the corrections due to hadron showering are large in the forward region,

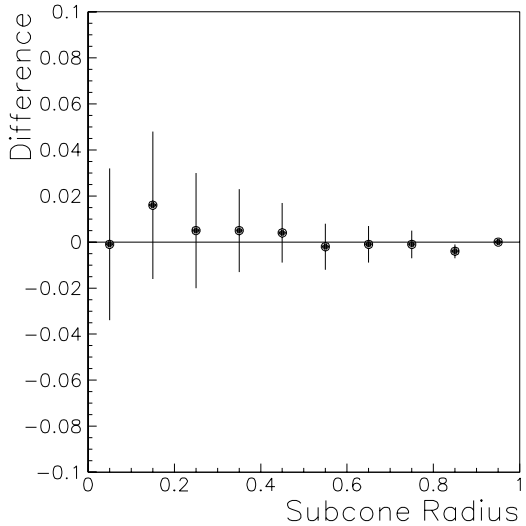

Figure 4.24

Difference in additive correction factors between modelling the calorimeter using the full plate level geometry and the mixture level geometry in GEANT.

we have confidence in them because they are derived from a series of well tested and verifiable elements. The combination of the Monte Carlo fragmentation and the mixture level GEANT have each been shown to describe the data well. The mixture level GEANT has been shown to agree with the full plate level GEANT, and the full plate level GEANT has been shown to describe pion showering well [28]. Also, the calorimeter correction to $\rho(r)$ are not strongly dependent on the exact fragmentation models chosen. While the different Monte Carlos have different fragmentation schemes, the effects on the jet shape are similar.

To build further confidence in the large effects caused by calorimeter showering in the forward region, the showering effects were studied using a second method. The shower profiles for both single pions and electrons in the central calorimeter are

known from test beam measurements. The transverse shower profiles of single pions and electrons of varying energies (2GeV-160GeV) were determined from the test beam results. A parameterization of the transverse energy profile was developed in order to determine the showering effects for pions and electrons of any energy. These test beam measurements were then used in place of the GEANT simulation of the calorimeter within the Isajet Monte Carlo. The simulation proceeded assuming all hadronic particles within the jet were charged pions and all others were electrons. To take into account that the shower profiles in the end calorimeters are not currently available, the shower profiles in the forward region were chosen to be the same as those used in the central region. This is a reasonable assumption since showers should develop in real space and not $\eta - \phi$ space. This second approach verified the large effects found using the GEANT shower simulation and were consistent within $\Delta\rho(r) = 0.01$.

5. Experimental Results and Comparisons to Theoretical Predictions

The measurement of the jet shape is important for many reasons. This measurement can provide necessary information in many experimental measurements, including jet energy scale corrections and trigger implementation. Comparing our measurement to phenomenological Monte Carlo simulations allows the simulations to be "tuned" to the experimentally measured jet shape. The theoretical partonic jet shape without fragmentation can be compared to our measurement. This can determine when fragmentation effects become necessary in theoretical calculations.

After all of the corrections described previously have been applied, the question of how the jet shape changes with energy and η can be answered. The effects of the neutral component within a jet can now be determined, and we are also able to answer the question, can NLO partonic processes describe jet shapes?

In order to measure how the jet shape changes with transverse energy and η, the jet shape is compared in different E_T and η regions. We compare our results to a previous jet shape measurement from CDF in order to determine the effects of the neutral component of a jet. We also compare our results to a next-to-leading order QCD theoretical prediction to determine if partonic processes alone can predict jet shapes.

5.1 Experimentally Measured Jet Shapes

After the corrections for the underlying event, hardware pedestal suppression, the jet energy scale, and calorimeter showering have been applied, the change in jet shape as a function of E_T can be measured. Other possible definitions of the jet shape such as $\frac{dE_T}{d\eta d\phi}$, $\frac{1}{E_T}\frac{dE_T}{d\eta d\phi}$, and $\frac{1}{E_T}dE_T$ are shown in Appendix B.

Figure 5.1 shows the jet shape for four different E_T regions. Jets are seen to narrow with increasing E_T. Jets with energy between 45 and 70 GeV have nearly 40% of their transverse energy located in the jet center. As the jet E_T increases, the fraction of energy contained in the jet center also increases, reaching approximately 56% for jets with transverse energy greater than 140 GeV.

All jets which passed the quality cuts were analyzed regardless of whether they were merged or split. As discussed in the jet reconstruction, overlapping jets were either merged into two separate jets or classified as split. The decision parameter used to merge or split pre-jets is not directly related between theory and experiment. However, the merge/split parameters directly affect our measured jet shape.

To measure the effects of merging and splitting on the jet shape, the jet shape was studied for the different merge/split classifications. Figure 5.2 shows the jet shape for different merge/split possibilities. As can be seen in figure 5.2, merged jets are much wider than non-merged jets. However, merging has little affect on the average jet shape since few jets are merged. The maximum effect on the average jet shape due to including or excluding merged jets is less than $\Delta\rho(r) \sim 0.02$. Appendix C shows the jet shape for the different merge/split classifications for all of the E_T and

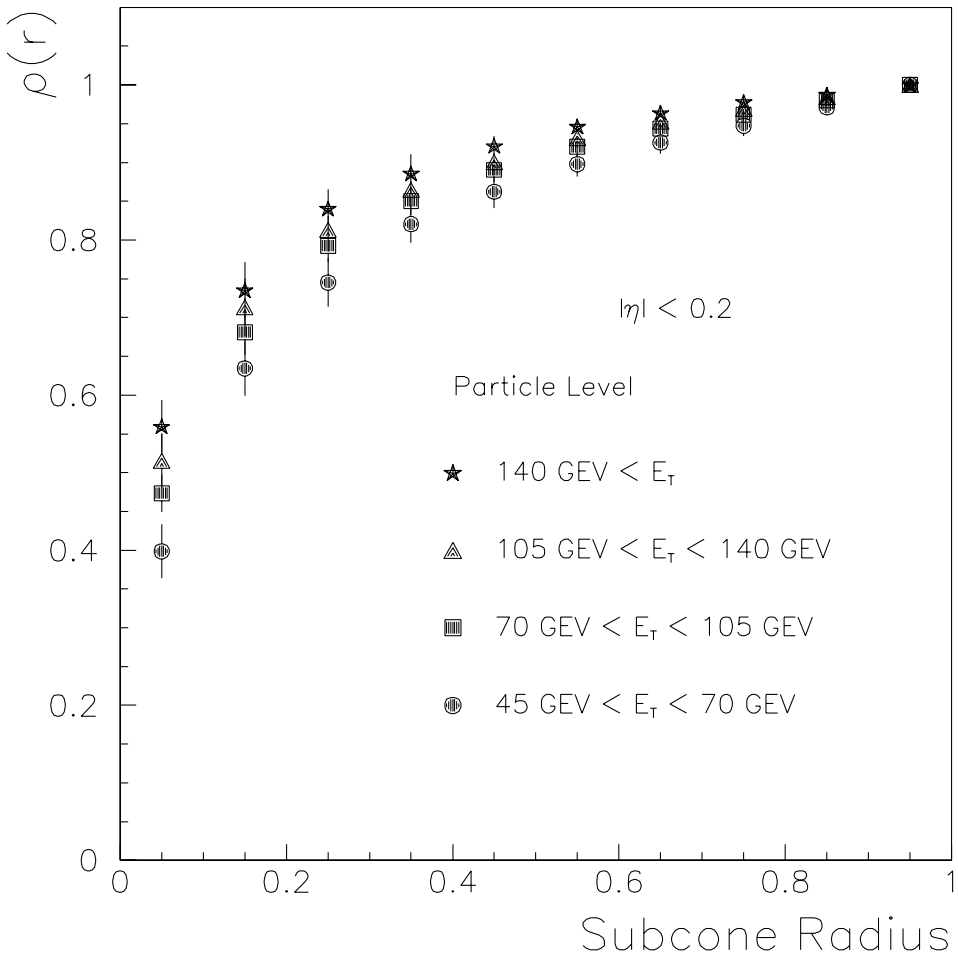

Figure 5.1

The jet shape in the central region for different E_T regions.

η regions studied in this analysis.

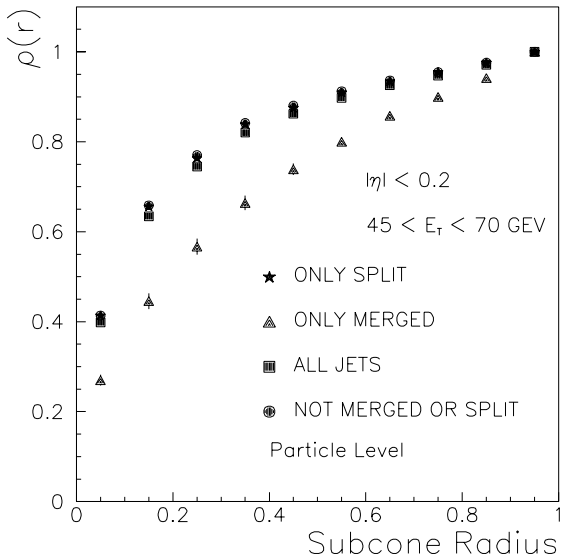

Figure 5.2

The jet shape in the central region for different merge/split classifications.

Another question that arises is the shape difference between leading and non-leading jets. The jet with the highest E_T in an event is defined to be the leading jet. All jets in an event with energy less than the leading jet are known as non-leading jets. Figure 5.3 shows the jet shape measured separately for leading jets and non-leading jets. The leading jets are much narrower than non-leading jets. This can be attributed to two separate effects. First, there is a uniform hadronic energy "glow" in the calorimeter which may increase as the hardness of the scatter increases. As discussed earlier, this underlying "glow" is a constant in a given E_T range and can be

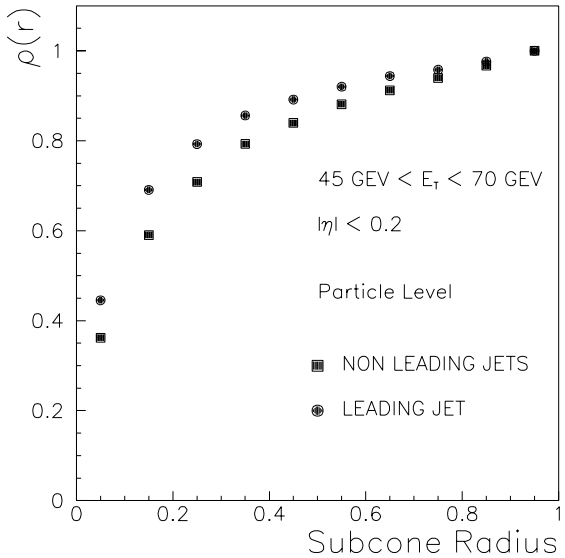

Figure 5.3

The jet shape in the central region for leading jets and non-leading jets.

measured at $R_{\eta\phi} > 1.0$. Approximately $\frac{dE_T}{d\eta d\phi} \sim 0.55$ GeV of this is due to the spectator interactions, measured using minimum bias events. The spectator interaction energy contribution is subtracted from the data. The remaining energy is due to the hard scatter. As the leading jet E_T increases, the hard scatter "glow" energy may also increase, causing more energy to be located at the edges of non-leading jets, widening their shape, see Table B.5.

Second, the fraction of gluon jets may be higher in non-leading jets, because they are more likely to arise from gluon bremsstrahlung from a hard scattered parton. As discussed in the introduction, as the percentage of gluon jets increases in a sample, the jet shape should widen. Gluon jets are expected to be wider than quark jets, because of the larger average color charge. Appendix D compares the leading jets

and non-leading jets for all of the E_T and η regions studied in this analysis.

Figure 5.4 compares the jet energy flow after the effects of the calorimeter have been removed to the published jet energy flow measured by CDF [4]. The effects of the calorimeter must be removed when comparing to CDF since CDF uses tracking chambers to determine the jet shape. Note the average energy of the jets in Figure 5.4 is lower for DØ than for CDF and the η regions are different. The two curves agree within errors, with DØ being slightly narrower. This shows that the jet shape is well measured by the charged particle content, the neutral component behaving similar to the charged particle component. We expect this result since the hadronic energy flow should be insensitive to electric charge with its much weaker coupling.

Figures 5.5 and 5.6 compare central jets to forward jets in the same E_T region. This is the first measurement of the jet shape at such high η. For both E_T regions the forward jets are substantially narrower than the central jets.

The experimentally measured jet shapes, with the calorimeter effects removed, are shown in both the central and forward regions in Tables 5.1 and 5.2

5.2 Comparison to Theoretical Predictions

After the effects of spectator processes and detector biases have been removed from the data, the jet shape can be directly compared to theoretical predictions. We compare our measurement to JETRAD [29], a computer generated exact Next-to-Leading Order (NLO) theoretical QCD prediction. In order to directly compare theoretical predictions to data, it is important that the theoretical jet clustering algo-

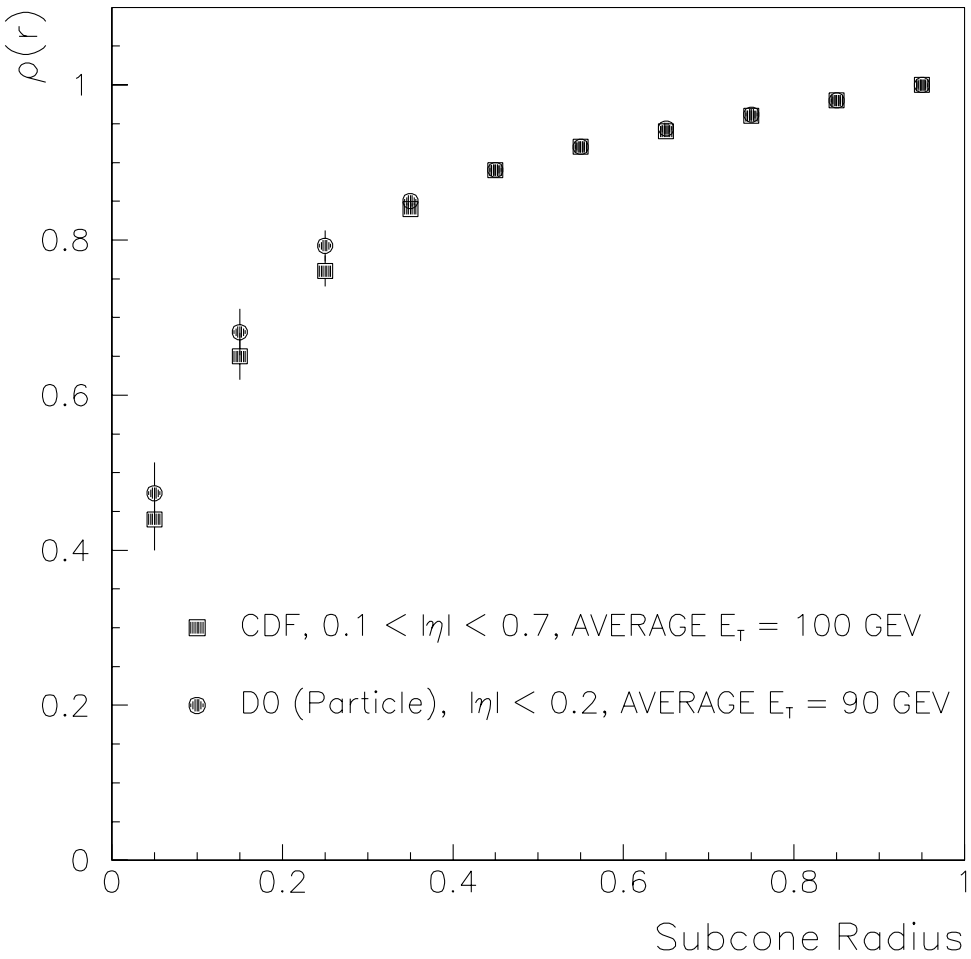

Figure 5.4

The jet shape at DØ and CDF.

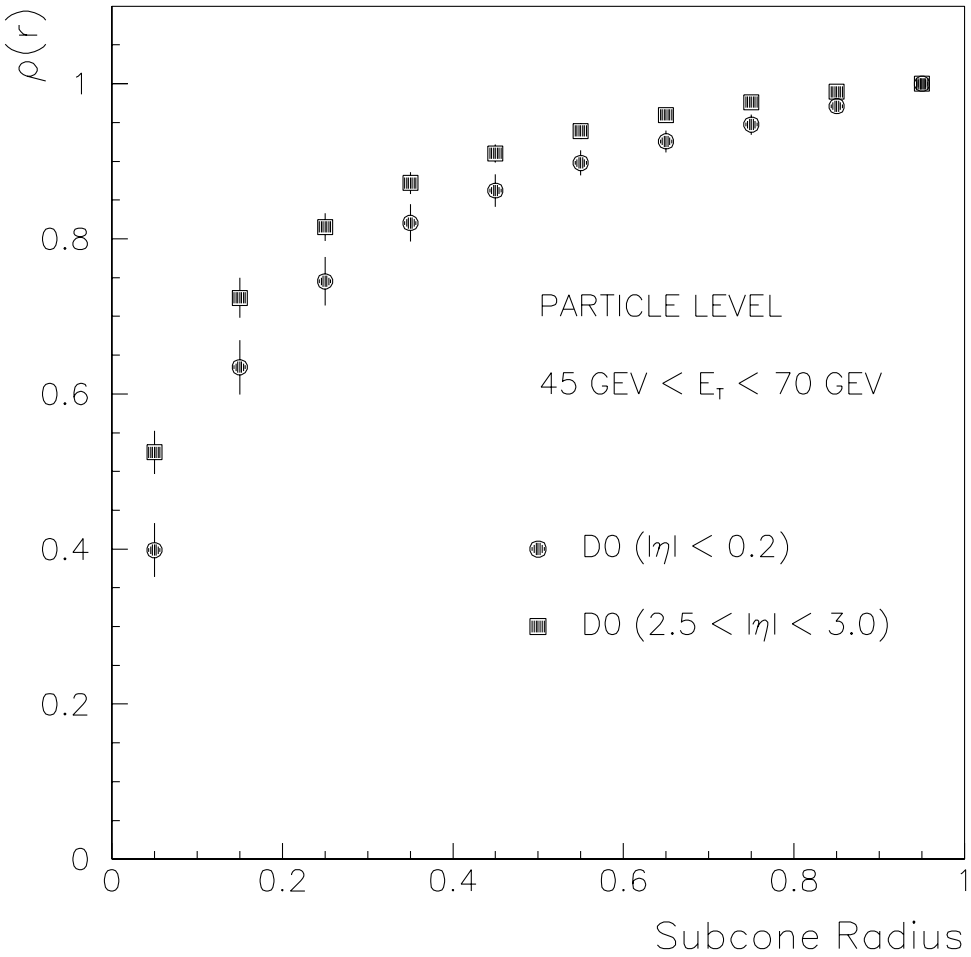

Figure 5.5

Comparing the jet shape in the central region and the forward region after the effects of the calorimeter have been removed for jets with transverse energy between 45 and 70 GeV.

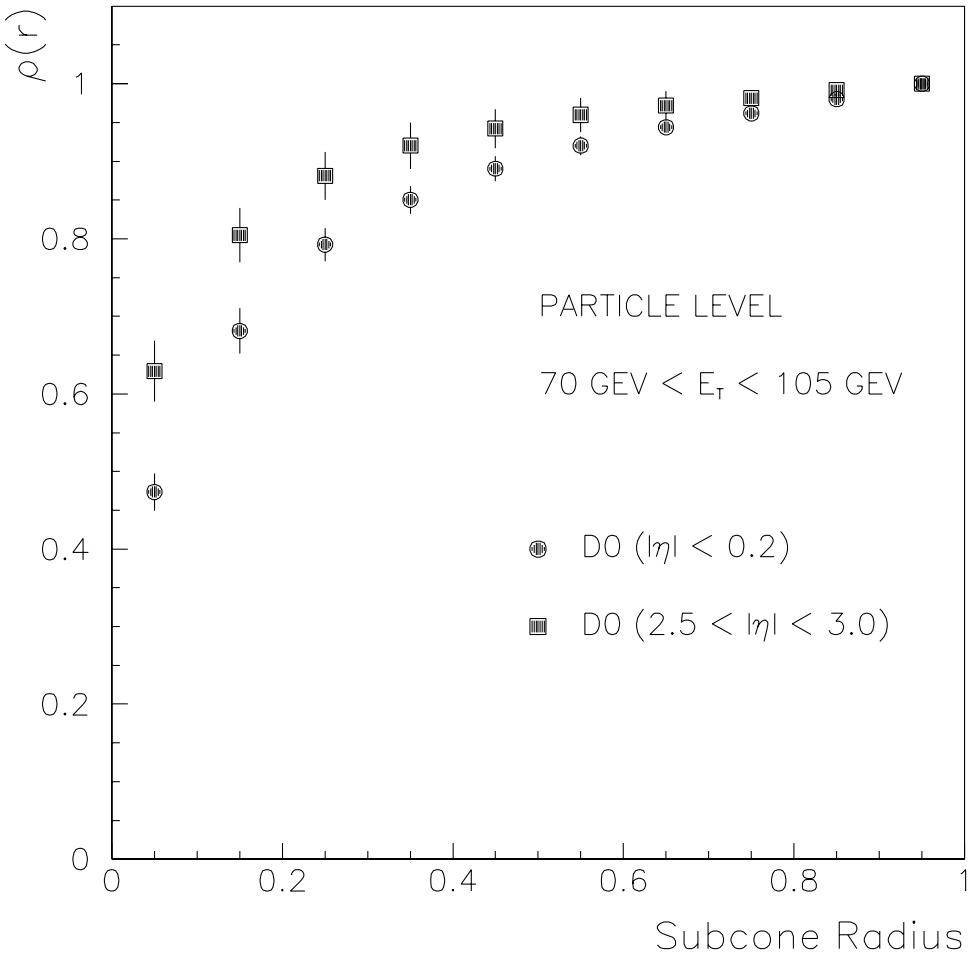

Figure 5.6

Comparing the jet shape in the central region and the forward region after the effects of the calorimeter have been removed for jets with transverse energy between 70 and 105 GeV.

Table 5.1

Energy Flow values at the particle level for jets located at $|\eta|$ <0.2

45-70 GeV $< E_T >$=59 GeV	70-105 GeV $< E_T >$=90 GeV	105-140 GeV $< E_T >$=128 GeV	140- GeV $< E_T >$=191 GeV
.40± .035	.47± .024	.52± .035	.56± .034
.63± .035	.68± .029	.71± .037	.74± .036
.75± .031	.79± .021	.81± .028	.84± .025
.82± .024	.85± .018	.87± .023	.89± .025
.86± .021	.89± .016	.90± .016	.92± .013
.90± .016	.92± .012	.93± .012	.95± .010
.93± .014	.94± .009	.95± .009	.96± .008
.95± .013	.96± .008	.97± .006	.98± .007
.97± .010	.98± .004	.98± .005	.99± .004
1.0± 0.0	1.0± 0.0	1.0± 0.0	1.0± 0.0

Table 5.2

Energy Flow values at the particle level for jets located at 2.5< $|\eta|$ <3.0

45-70 GeV $< E_T >$=59 GeV	70-105 GeV $< E_T >$=87 GeV
.52± .028	.63± .039
.72± .026	.80± .035
.82± .018	.88± .031
.87± .014	.92± .030
.91± .012	.94± .025
.94± .010	.96± .022
.96± .007	.97± .018
.98± .005	.98± .008
.99± .003	.99± .006
1.0± 0.0	1.0± 0.0

rithm be as similar as possible to the experimental jet algorithm. Identical algorithms cannot be used for both theory and data because JETRAD does not contain parton fragmentation. In JETRAD, two partons are clustered into one final state jet, using the same η and ϕ algorithms used in the data analysis. A single jet is formed if two partons are within a radius $R_{\eta\phi} < 1.0$ from their summed momentum vector. The energy of the jet is the sum of the energies of the two partons and the jet direction is the momentum vector sum of the original two partons.

As discussed in chapter 2, only a restricted band of renormalization parameters is allowed in perturbative QCD calculations. Because of the uncertainty in the choice of renormalization scale, the data is compared to the theoretical jet shape for three different renormalization scales, $\mu = 2E_T$, E_T, and $E_T/2$, where E_T refers to the E_T of the leading jet in the event.

To compare the data to the theoretical prediction, it is also necessary to input the proton parton distribution functions into the QCD calculations of the jet shape. The parton distribution functions we chose to use are parameterizations of empirical data obtained from deep inelastic electron and neutrino scattering off of nucleons. The parton distribution function parameterization in reference [30], called the CTEQ2M parton distribution functions were chosen for determining the theoretical jet shape for all energies and η regions. These parton distribution functions were chosen because they included the most recent experiments in their fits to the data. To determine if the jet shape is sensitive to the choice of parameterizations, a different set of recent parton distribution functions were chosen, called the MRSD- [31] parton distribution

functions. The jet shape was found to be insensitive to the choice of the CTEQ2M or the MRSD- parton distribution functions. When compared, the two jet shapes obtained were identical within statistical errors.

Figures 5.7 - 5.10 compare the experimentally measured jet shape in the central region, after all calorimeter biases and corrections have been removed, to the NLO theoretical prediction. The data fall within the theoretical uncertainty resulting from the choice of renormalization scale, however, no single renormalization scale accurately describes the data in all E_T regions. Qualitatively, NLO theory is able to describe the data in the central region. That is, the theoretically measured jet shapes narrow with increasing jet E_T similar to data, but the data narrows more quickly than the theory predicts.

Figures 5.11 and 5.12 compare the NLO theoretical prediction to the experimentally measured jet shape in the forward region after all corrections to the data have been applied. In the forward region, the theoretical predictions do not describe the data. The experimentally measured jet shapes do not fall within the uncertainty due to the choice in the renormalization scale. Even qualitatively, the theory is unable to describe the jet shape. The theory predicts the jets to broaden with increasing jet E_T, while the experimentally measured jet shape narrows.

Since there is no unique algorithm to determine the η_{jet} and ϕ_{jet} of the jet axis, the effects on the jet shape due to different algorithms were studied. Three different methods of finding η_{jet} and ϕ_{jet} were used in the various stages of the jet reconstruction. The first method of determining η_{jet} and ϕ_{jet} is the DØ jet reconstruction

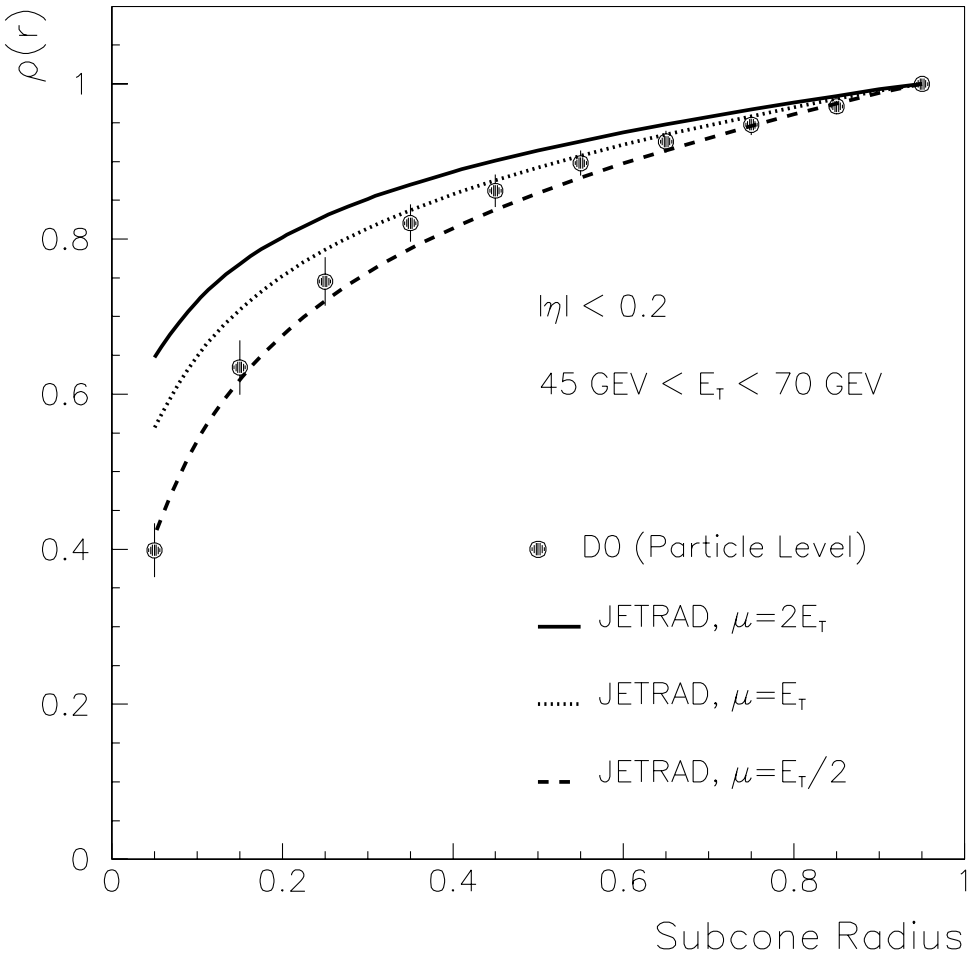

Figure 5.7

Comparing data to NLO theory in the central region for jets with transverse energy between 45 and 70 GeV.

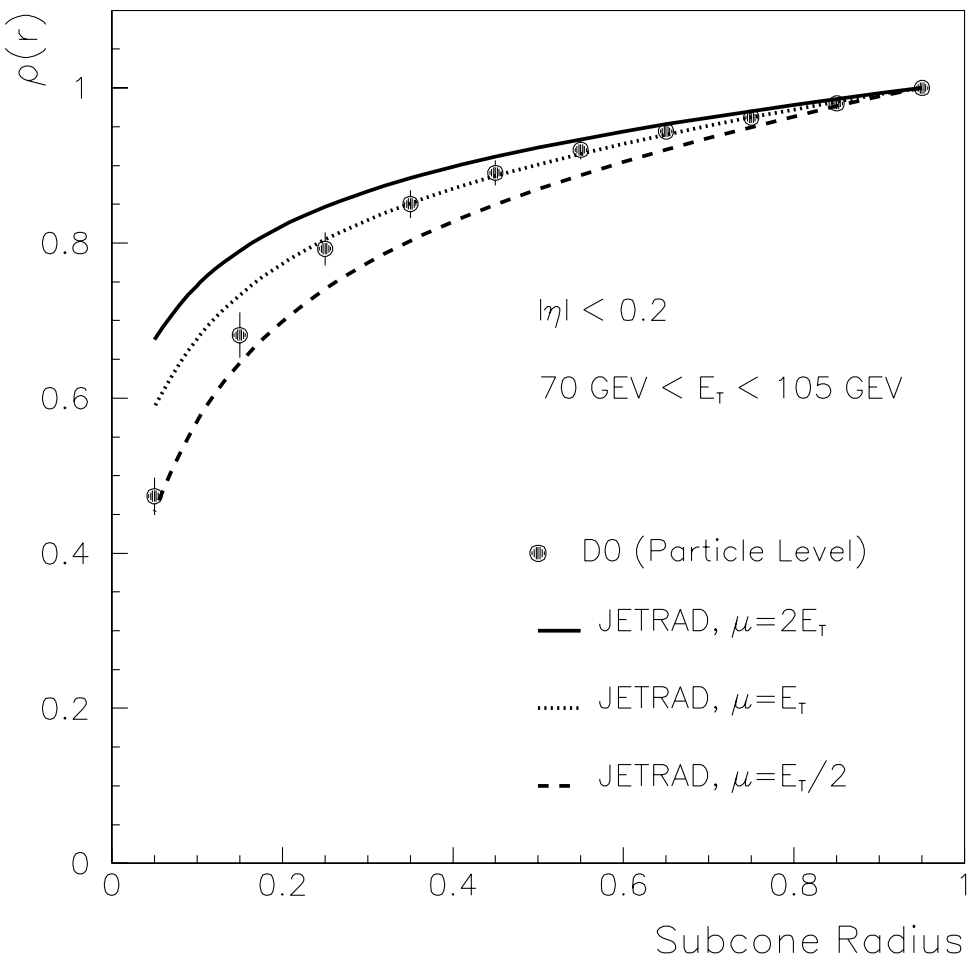

Figure 5.8

Comparing data to NLO theory in the central region for jets with transverse energy between 70 and 105 GeV.

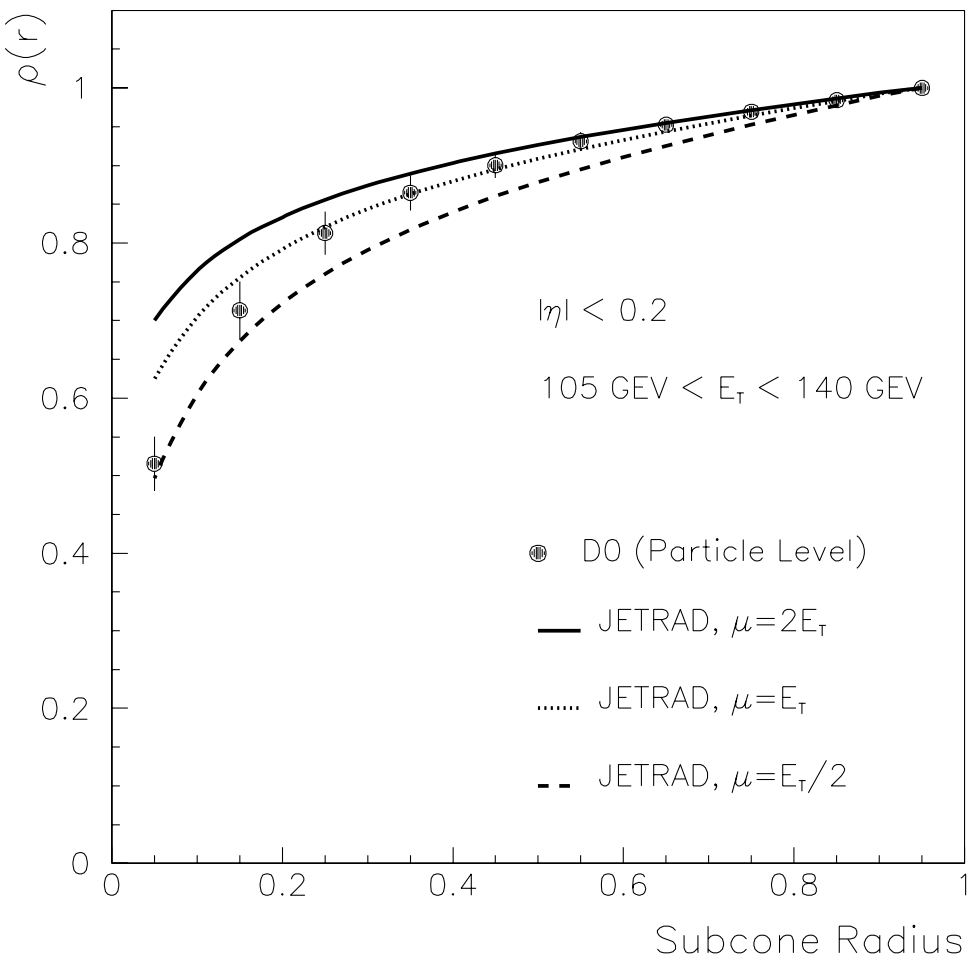

Figure 5.9

Comparing data to NLO theory in the central region for jets with transverse energy between 105 and 140 GeV.

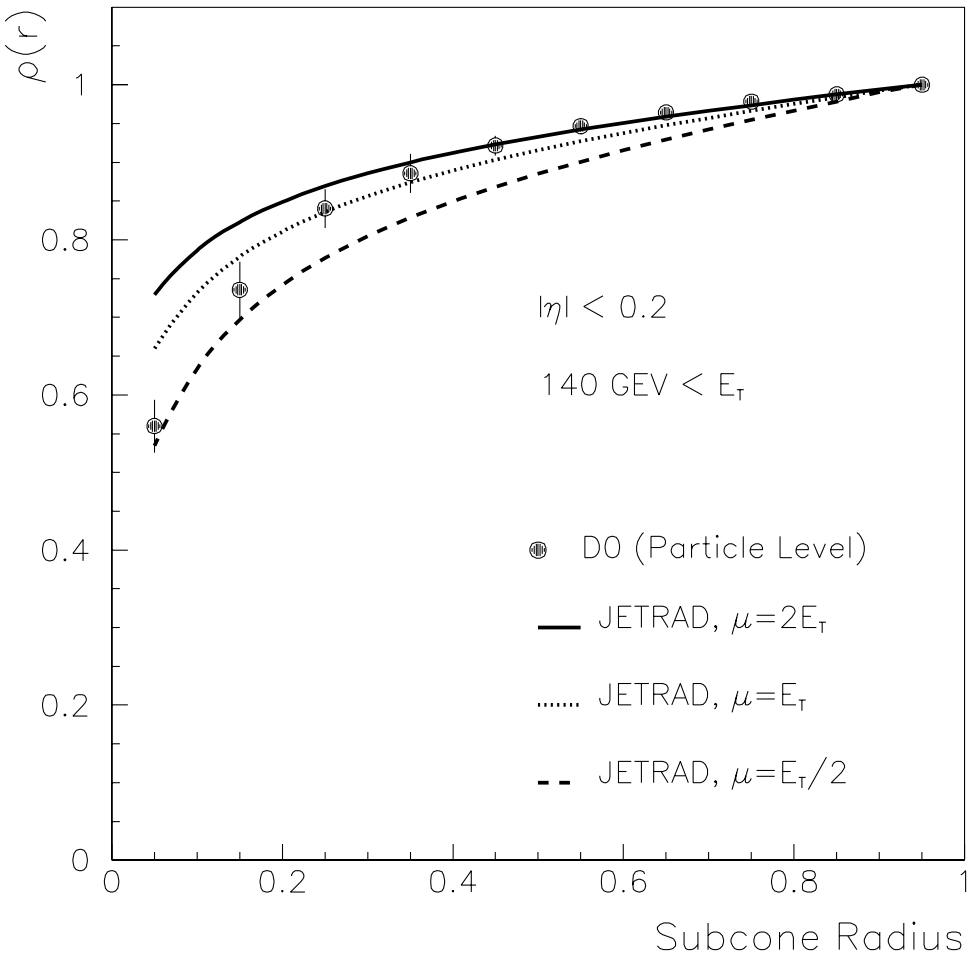

Figure 5.10

Comparing data to NLO theory in the central region for jets with transverse energy greater than 140 GeV.

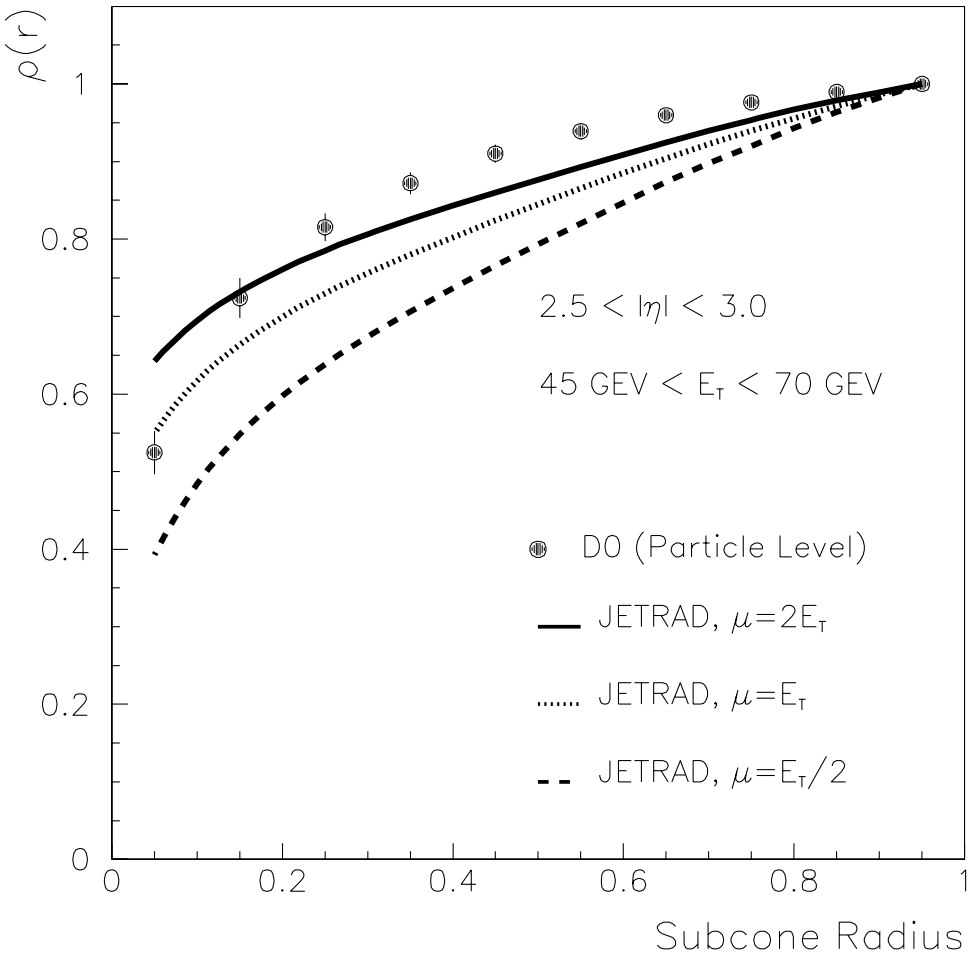

Figure 5.11

Comparing data to NLO theory in the forward region for jets with transverse energy between 45 and 70 GeV.

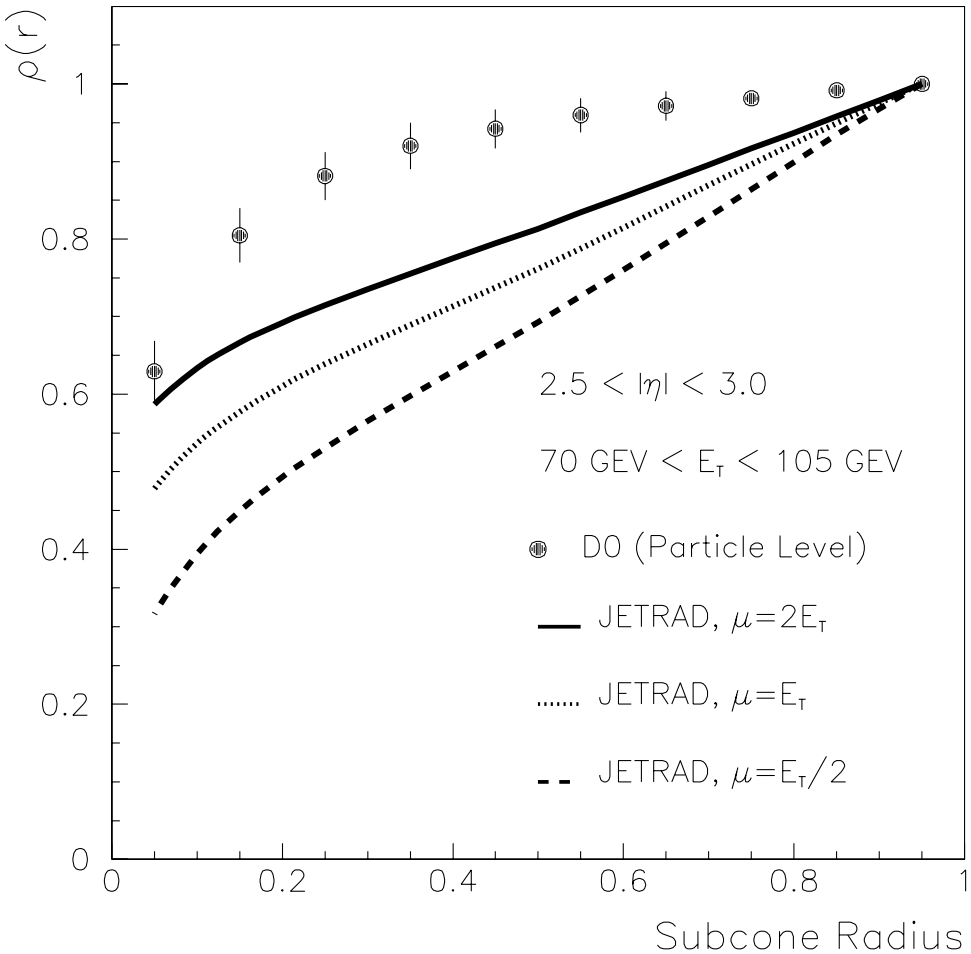

Figure 5.12

Comparing data to NLO theory in the forward region for jets with transverse energy between 70 and 105 GeV.

algorithm. The second algorithm reconstructs jets using the Snowmass accord, shown in equations 4.2 and 4.3, for all steps in the jet reconstruction. The last algorithm is a modified DØ method which uses the DØ technique, determined by equations 4.4 and 4.5, for all stages in the jet reconstruction.

Figure 5.13 shows the differences in the jet shape for the three different choices of algorithm in the central region for JETRAD. There is a noticeable change in the jet shape depending upon the choice of η_{jet} and ϕ_{jet} search method. The DØ modified algorithm and the DØ algorithm are almost identical, while the Snowmass algorithm broadens the jet shape by $\Delta\rho(r) \sim 0.03$.

Figure 5.14 shows the differences in jet shape for different methods of determining η_{jet} and ϕ_{jet} in the forward region. The effects on the jet shape due to changing the algorithm used to calculate η_{jet} and ϕ_{jet} is much more pronounced at high η. The narrowest jet shape is obtained by using the Snowmass algorithm. The DØ modified algorithm is wider than the Snowmass algorithm by $\Delta\rho(r) \sim 0.05$, and the broadest jet shape is obtained by using the DØ approach.

The algorithm used to determine η_{jet} and ϕ_{jet} also determine the change in the theoretical jet shape with η. Depending upon the choice of algorithm, the jet shape can either narrow or broaden with increasing η. The Snowmass algorithm causes the theoretical jet shape to narrow with increasing η, while both the DØ and the DØ modified algorithms cause the theoretical jet shapes to widen with increasing η.

To measure the effects of the η_{jet} and ϕ_{jet} algorithms in a Monte Carlo simulation, the same three algorithms were used to reconstruct jets in Herwig. Figure 5.15 shows

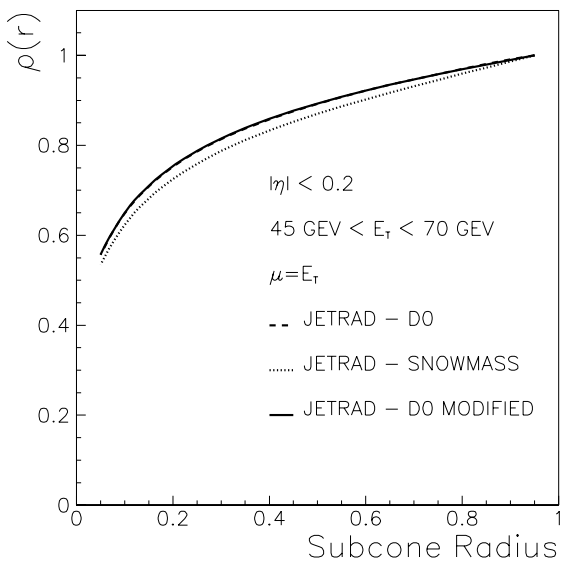

Figure 5.13

Effects on $\rho(r)$ due to changing the algorithm used to calculate η_{jet} and ϕ_{jet} in Jetrad for jets located at $|\eta| < 0.2$.

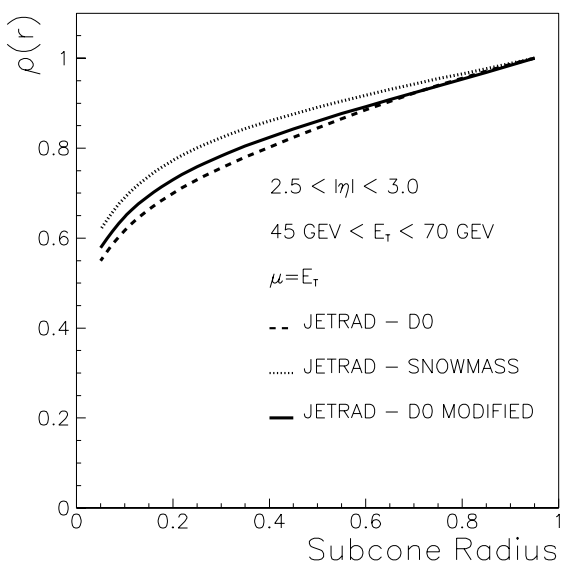

Figure 5.14

Effects on $\rho(r)$ due to the algorithm used to calculate η_{jet} and ϕ_{jet} in Jetrad for jets located at $2.5 < |\eta| < 3.0$.

the effect of changing the search technique of η and ϕ in Herwig in the central region. Different η_{jet} and ϕ_{jet} algorithms cause little change in the jet shape for centrally located jets.

The DØ algorithm used to calculate η_{jet} and ϕ_{jet} were introduced to remove discrepancies between the direction of the parent parton and the reconstructed jet in the forward region. Therefore, differences in the jet shape are expected due to the different algorithms at high η. Figure 5.16 shows the effects of different algorithms on the jet shape for Herwig in the forward region. Both the DØ algorithm and the modified DØ algorithm cause narrower jets than the Snowmass algorithm.

Qualitatively, JETRAD cannot predict the change in jet shape due to different η_{jet} and ϕ_{jet} algorithms. In Herwig the Snowmass algorithm produces the broadest jets, while in JETRAD the narrowest jets are produced using the Snowmass algorithm. There is little effect due to different η_{jet} and ϕ_{jet} algorithms on the jet shape in Herwig and large effects in the theoretical jet shape. This introduces another uncertainty in the theoretical jet shape caused by different η_{jet} and ϕ_{jet} algorithms.

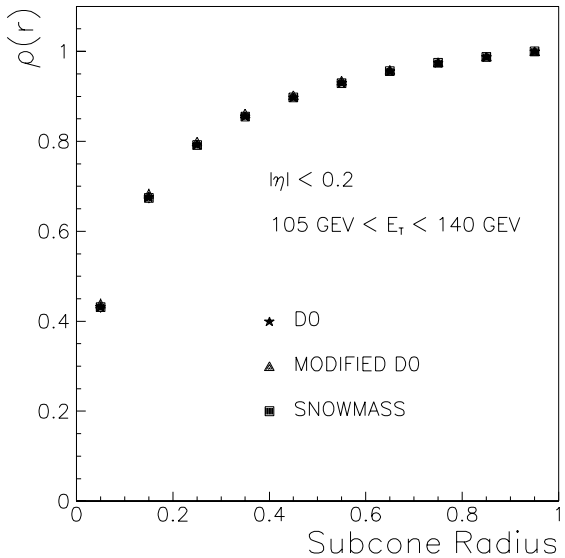

Figure 5.15

Effects on $\rho(r)$ due to changing the algorithm used to calculate η_{jet} and ϕ_{jet} in Herwig for jets located at $|\eta| < 0.2$.

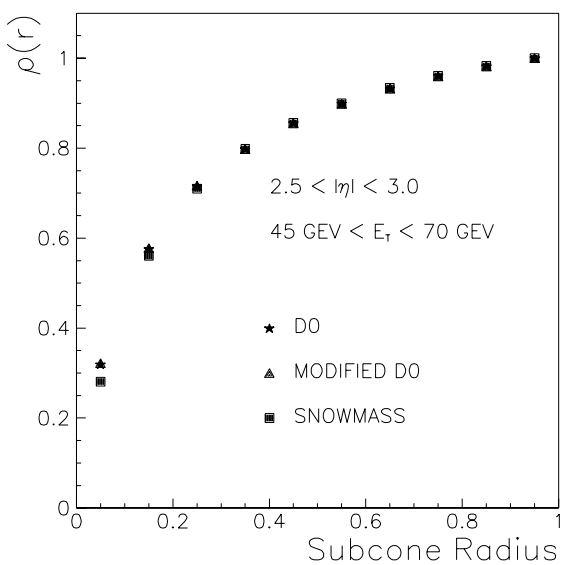

Figure 5.16

Effects on $\rho(r)$ due to changing the algorithm used to calculate η_{jet} and ϕ_{jet} in Herwig for jets located at $2.5 < |\eta| < 3.0$.

6. Conclusions

We have measured the transverse energy flow in a jet at a center of mass energy $\sqrt{s}$=1.8 TeV using the DØ detector. The jet shape was measured as a function of jet E_T in two different η regions. Comparisons to Monte Carlo simulations were performed and calorimeter biases were removed to allow comparisons to NLO theoretical QCD predictions.

The jet shape is found to narrow with increasing jet E_T. This is consistent with the transverse momentum of particles within the jet changing slowly with energy, while the parallel momentum of particles within the jet changes approximately with energy. The effects of merging and splitting on the average jet shape are small. The merged jet shape differs substantially from the average jet shape. However, few jets are merged so there is little effect on the average jet shape. In the same E_T region, leading jets are much narrower than non-leading jets. This is consistent with gluon jets contributing a higher fraction of non-leading jets and gluon jets being broader than quark jets.

The Herwig Monte Carlo, in which the entire jet energy spectrum is simulated, describes the data well at all E_T and η regions. The Isajet and Pythia Monte Carlos, in which the entire jet spectrum is not simulated, differ from the data, allowing us to

show that calorimeter biases have little effect due to fragmentation schemes or Monte Carlos jet shape differences.

Forward jets are much narrower then central jets in the same E_T region. This is consistent with a higher quark jet content at high η and quark jets being narrower than gluon jets.

Partonic theory at leading order, in which each jet is described by a single parton, cannot make a meaningful prediction of the jet shape. At NLO, two partons may reside in a jet, allowing a prediction of the jet shape. Therefore, the theoretical jet shape is a first order measurement at partonic NLO and large effects due to the renormalization scale are expected and seen.

In the central region, the data are within the theoretical uncertainty due to the choice of renormalization scale. NLO theoretical jet shapes qualitatively agree with the experimentally measured jet shapes. Theory correctly predicts the narrowing of jets as the E_T of the jets increase, but the data narrows more quickly than theoretical predictions.

In the forward region, NLO partonic theory does not describe the jet shape. The data are not within the theoretical uncertainty due to the choice of renormalization scale. Qualitatively, theory is unable to describe the data. The data narrows with increasing η while the theoretical jet shape broadens with increasing η. Also, the data narrows with increasing E_T while the theoretical jet shape broadens with increasing E_T.

The effects due to different η_{jet} and ϕ_{jet} algorithms in jet reconstruction have large

effects on the partonic theoretical jet shape. Monte Carlo simulations, in which fragmentation effects are included, change little due to changing η_{jet} and ϕ_{jet} algorithms. This introduces an additional theoretical error in the jet shape due to η_{jet} and ϕ_{jet} algorithms.

Partonic simplifications of the jet shape cannot describe the jet shape accurately at NLO. Fragmentation of the partons may be necessary in order to describe the experimentally measured jet shape. Fragmentation of the partons may cause the jet to widen, changing the jet shape. Fragmentation effects are low momentum transfer processes and cannot be calculated accurately, therefore they are modelled. The Monte Carlo simulations can provide an estimate of the fragmentation effects, but the effects cannot be directly added into JETRAD. Fragmentation effects are modelled at all orders and JETRAD is at NLO. If the Monte Carlo fragmentation effects are directly added into JETRAD, NLO contributions are double counted.

In order to correctly predict the jet shape, either higher orders must be added into theory or the effects of fragmentation are not negligible and must be included when calculating jet shapes.

BIBLIOGRAPHY

BIBLIOGRAPHY

1. Physical Review D, Review of Particle Properties, Volume 45, Number 11, (1992)

2. DØ Collaboration, S. Abachi *et al.*, Phys. Rev. Lett. 72, 2138 (1994)

3. The Two-Jet Differential Cross Section at $O(\alpha_s^3)$ in Hadron Collisions. W.T. Giele *et al.*, Fermilab-Pub-94/070-T

4. Measurement of Jet Shapes in $p\bar{p}$ Collisions at $\sqrt{s}$=1.8 TeV. F. Abe *et al.*, Phys. Rev. Lett., Vol 70, Number 6, 713 (1993)

5. R.K. Ellis and W.J. Stirling "QCD and Collider Physics", Fermilab-Conf-90/164-T, August 1990

6. Particles and Forces: At the Heart of the Matter. R. Carrigan and W. Trower

7. The DØ Collaboration, "The DØ Detector", Nucl. Inst and Methods **A338** 185 (1994)

8. J.F. Detoeuf *et al.*, (DØ collaboration), Nucl. Inst and Methods, **A279**, 310 (1989)

9. C. Brown *et al.*, (DØ collaboration), Nucl. Inst and Methods, **A279**, 331 (1989)

10. A. Clark *et al.*, (DØ collaboration), Nucl. Inst and Methods, **A279**, 243 (1989)

11. A. Clark *et al.*, (DØ collaboration), Nucl. Inst and Methods, **A315**, 193 (1992)

12. M. Abolins *et al.*, (DØ collaboration), Nucl. Inst and Methods, **A280**, 36 (1989)

13. S. Aronson *et al.*, (DØ collaboration), Nucl. Inst and Methods, **A269**, 492 (1987)

14. S. Abachi *et al.*, (DØ collaboration), Nucl. Inst and Methods, **A324**, 53 (1993)

15. H. Aihara *et al.*, (DØ collaboration), Nucl. Inst and Methods, **A325**, 393 (1993)

16. K. McFarland, DØ internal note #840, 1989 (Unpublished)

17. M. Abolins *et al.*, (DØ collaboration), Nucl. Inst and Methods, **A289**, 543 (1990)

18. M. Abolins *et al.*, (DØ collaboration), IEEE Trans. Nucl. Sci., **A36**, 384 (1990)

19. *Toward a Standardization of Jet Definition*, S.D Ellis, J. Huth, N. Wainer, K. Meier, N. Hadley, S. Soper and M. Greco, Proceedings of *Research Directions For The Decade, Snowmass 1990*, Snowmass, July 1990, ed. E.L. Berger, p.134, (World Scientific, Singapore, 1992)

20. V. Elvira *et al.*, DØ internal note #1763

21. B. Kehoe, DØ internal note #2052

22. The ZEUS Calorimeter Group, *Response of a Uranium-Scintillator Calorimeter to Electrons, Pions and Protons in the Momentum Range 0.5-10 GeV/c* DESY 89-149, November 1989, ISSN 0418-9833

23. Bob Hirosky, Ph. D. Thesis, University of Rochester, Rochester, NY, 1992

24. G. Marchesini and B.R. Webber, Nucl. Phys. **B310** (1988) 461.

25. F. Paige and S.D. Protopopescu, BNL Report No. BNL 38034, 1986 (unpublished).

26. H.U. Bengtsson, T. Sjostrand, Computer Phys. Comm. 46 (1987) 43; T. Sjostrand, Computer Phys. Comm. 39 (1986) 347.

27. Geant 3.14, R. Brun, *et al.*, CERN

28. J. Womersley, Fermilab/Conf-92/306 (unpublished)

29. JETRAD authors W.T. Giele, E.W.N. Glover, D.A. Kosower

30. J. Botts, *et al.*, (CTEQ Collaboration), *CTEQ Parton Distributions and Flavor Dependence of Sea Quarks*, Phys. Lett. **B304**, 159-166, (1993).

31. A. D. Martin, W. J. Stirling, R. G. Roberts, Phys. Lett. **B306**, 145 (1993): Erratum-*ibid* **B309**, 492 (1993).

APPENDICES

Appendix A: Correction Factors

This appendix lists all of the corrections applied to the data. The underlying event correction removes the energy caused by spectator interactions. The zero suppression correction is required because of the hardware pedestal cut. The energy scale correction was applied to calibrate jets. The calorimeter effects refer to correcting the jet shape for the non-linear calorimeter response and calorimeter showering. Each table lists the corrections applied to the jet shape corresponding to the same E_T and η region shown in Tables 5.1 and 5.2.

Table A.1

Additive corrections for jets located at $|\eta| < 0.2$ with transverse energy between 45 and 70 GeV.

Subcone Radius	Underlying Event	Zero Suppression	Energy Scale	Calorimeter Effects
0.1	.014 ± .003	.024 ± .004	-.016 ± .004	.086 ± .032
0.2	.024 ± .004	.041 ± .006	-.017 ± .006	.051 ± .029
0.3	.025 ± .004	.044 ± .006	-.014 ± .004	.024 ± .024
0.4	.022 ± .004	.041 ± .005	-.010 ± .003	.018 ± .017
0.5	.018 ± .002	.035 ± .003	-.007 ± .002	.006 ± .016
0.6	.014 ± .002	.028 ± .002	-.005 ± .002	.001 ± .012
0.7	.010 ± .001	.020 ± .002	-.003 ± .001	-.003 ± .012
0.8	.006 ± .001	.011 ± .001	-.003 ± .001	-.006 ± .012
0.9	.002 ± .001	.004 ± .001	-.001 ± .001	-.005 ± .010
1.0	0.0 ± 0.0	0.0 ± 0.0	0.0 ± 0.0	0.0 ± 0.0

Table A.2

Additive corrections for jets located at $|\eta| < 0.2$ with transverse energy between 70 and 105 GeV.

Subcone Radius	Underlying Event	Zero Suppression	Energy Scale	Calorimeter Effects
0.1	.013 ± .003	.019 ± .004	-.018 ± .01	.088 ± .014
0.2	.018 ± .003	.029 ± .004	-.019 ± .01	.038 ± .020
0.3	.019 ± .003	.032 ± .004	-.013 ± .008	.022 ± .010
0.4	.015 ± .002	.028 ± .002	-.009 ± .005	.010 ± .011
0.5	.012 ± .002	.024 ± .002	-.006 ± .004	.004 ± .010
0.6	.010 ± .001	.019 ± .001	-.005 ± .003	.001 ± .007
0.7	.006 ± .001	.012 ± .001	-.004 ± .002	.001 ± .005
0.8	.003 ± .001	.007 ± .001	-.003 ± .001	-.001 ± .005
0.9	.001 ± .001	.002 ± .001	-.001 ± .001	-.001 ± .003
1.0	0.0 ± 0.0	0.0 ± 0.0	0.0 ± 0.0	0.0 ± 0.0

Table A.3

Additive corrections for jets located at $|\eta| < 0.2$ with transverse energy between 105 and 140 GeV.

Subcone Radius	Underlying Event	Zero Suppression	Energy Scale	Calorimeter Effects
0.1	.010 ± .002	.015 ± .002	-.045 ± .02	.086 ± .022
0.2	.015 ± .003	.023 ± .003	-.039 ± .02	.034 ± .026
0.3	.014 ± .003	.023 ± .003	-.033 ± .014	.019 ± .018
0.4	.012 ± .002	.019 ± .003	-.023 ± .011	.007 ± .015
0.5	.006 ± .001	.013 ± .002	-.017 ± .008	.004 ± .010
0.6	.006 ± .001	.011 ± .001	-.012 ± .005	.003 ± .007
0.7	.004 ± .001	.008 ± .001	-.008 ± .004	.001 ± .006
0.8	.002 ± .001	.005 ± .001	-.005 ± .002	0.00 ± .004
0.9	.001 ± .001	.002 ± .001	-.001 ± .001	-.001 ± .003
1.0	0.0 ± 0.0	0.0 ± 0.0	0.0 ± 0.0	0.0 ± 0.0

Table A.4

Additive corrections for jets located at $|\eta| < 0.2$ with transverse energy greater than 140 GeV.

Subcone Radius	Underlying Event	Zero Suppression	Energy Scale	Calorimeter Effects
0.1	.007 ± .001	.010 ± .002	-.014 ± .002	.089 ± .030
0.2	.010 ± .002	.016 ± .002	-.010 ± .004	.028 ± .032
0.3	.011 ± .002	.017 ± .002	-.008 ± .004	.014 ± .020
0.4	.007 ± .001	.013 ± .001	-.004 ± .003	.001 ± .022
0.5	.005 ± .001	.010 ± .001	-.002 ± .002	.001 ± .010
0.6	.005 ± .001	.008 ± .001	-.001 ± .001	.001 ± .008
0.7	.003 ± .001	.005 ± .001	-.001 ± .001	0.0 ± .007
0.8	.001 ± .001	.004 ± .001	-.001 ± .001	0.0 ± .006
0.9	.001 ± .001	.001 ± .001	-.001 ± .001	-.001 ± .003
1.0	0.0 ± 0.00	0.00 ± 0.00	0.0± 0.0	0.0 ± 0.0

Table A.5

Additive corrections for jets located at $2.5 < |\eta| < 3.0$ with transverse energy between 45 and 70 GeV.

Subcone Radius	Underlying Event	Zero Suppression	Energy Scale	Calorimeter Effects
0.1	.012 ± .002	.003 ± .001	-.043 ± .006	.27 ± .024
0.2	.023 ± .004	.006 ± .001	-.048 ± .008	.23 ± .020
0.3	.029 ± .005	.007 ± .001	-.041 ± .006	.175 ± .010
0.4	.030 ± .004	.008 ± .001	-.031 ± .004	.13 ± .006
0.5	.029 ± .004	.007 ± .001	-.022 ± .003	.094 ± .005
0.6	.025 ± .004	.006 ± .001	-.016 ± .002	.067 ± .004
0.7	.019 ± .003	.005 ± .001	-.011 ± .001	.044 ± .003
0.8	.012 ± .001	.003 ± .001	-.006 ± .001	.025 ± .002
0.9	.006 ± .001	.001 ± .001	-.003 ± .001	.009 ± .002
1.0	0.0 ± 0.0	0.0 ± 0.0	0.0 ± 0.0	0.0 ± 0.0

Table A.6

Additive corrections for jets located at $2.5 < |\eta| < 3.0$ with transverse energy between 70 and 105 GeV.

Subcone Radius	Underlying Event	Zero Suppression	Energy Scale	Calorimeter Effects
0.1	.013 ± .002	.003 ± .001	-.036 ± .010	.30 ± .016
0.2	.023 ± .004	.006 ± .001	-.002 ± .008	.22 ± .013
0.3	.026 ± .005	.007 ± .001	.007 ± .008	.16 ± .010
0.4	.027 ± .005	.007 ± .001	.015 ± .010	.115 ± .015
0.5	.026 ± .004	.007 ± .001	.022 ± .010	.074 ± .014
0.6	.023 ± .004	.006 ± .001	.013 ± .010	.052 ± .013
0.7	.016 ± .001	.002 ± .001	.009 ± .009	.033 ± .012
0.8	.019 ± .001	.001 ± .001	.001 ± .004	.017 ± .005
0.9	.005 ± .001	.001 ± .001	.001 ± .001	.006 ± .005
1.0	0.0 ± 0.0	0.0 ± 0.0	0.0 ± 0.0	0.0 ± 0.0

Appendix B: Alternative Definitions of the Jet Shape

The definition of the jet shape $\rho(r)$ is not the only possible definition. This appendix shows alternate definitions of the jet shape. Figures and Tables B.1 and B.2 show the jet shape defined as the fraction of transverse energy within each subcone, $\frac{dE_T}{E_T}$. Figures and Tables B.3 and B.4 show the jet shape defined as $\frac{1}{E_T}\frac{dE_T}{d\eta d\phi}$. Figures and Tables B.5 and B.6 show the jet shape defined as $\frac{dE_T}{d\eta d\phi}$.

Table B.1

The jet shape defined as $\frac{dE_T}{E_T}$ for jets located at $|\eta| < 0.2$.

Subcone Radius	45-70	70-105	105-140	140-
0.1	.400± .035	.470± .024	.520± .035	.560± .034
0.2	.230± .035	.207± .029	.200± .037	.177± .036
0.3	.110± .030	.110± .021	.100± .028	.104± .025
0.4	.075± .024	.058± .018	.052± .023	.046± .025
0.5	.042± .021	.040± .016	.035± .016	.035± .013
0.6	.035± .016	.030± .012	.031± .012	.026± .010
0.7	.029± .014	.024± .009	.021± .009	.017± .008
0.8	.021± .013	.018± .008	.017± .006	.014± .007
0.9	.024± .010	.017± .004	.015± .005	.010± .004
1.0	.029± .010	.020± .004	.012± .005	.010± .004

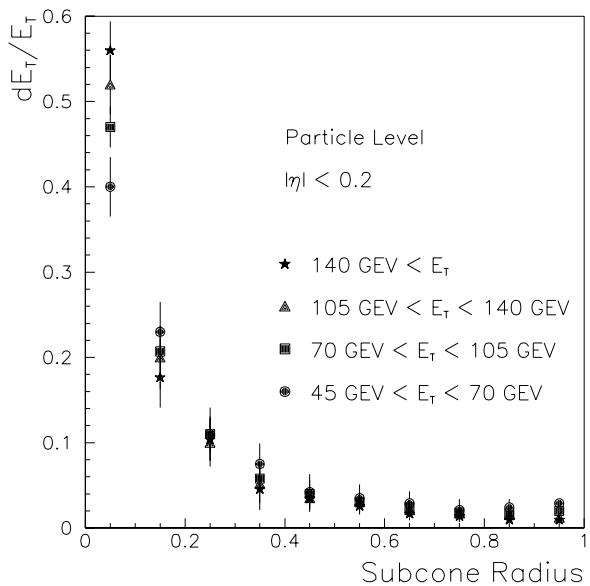

Figure B.1

The jet shape defined as $\frac{dE_T}{E_T}$ for jets located at $|\eta| < 0.2$.

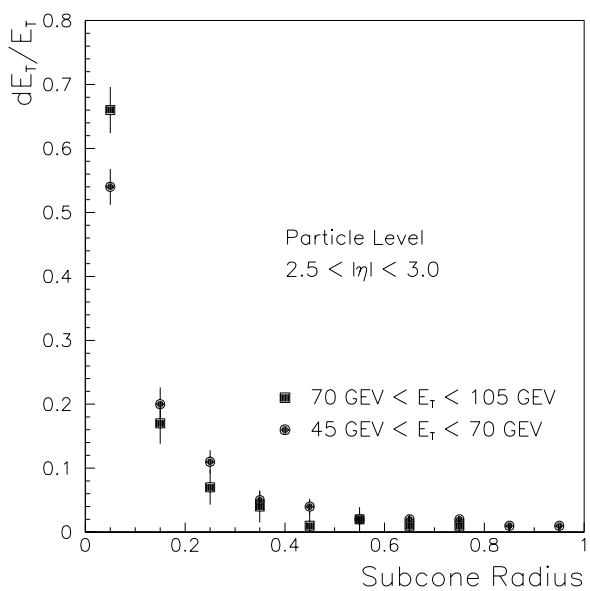

Figure B.2

The jet shape defined as $\frac{dE_T}{E_T}$ for jets located at $2.5 < |\eta| < 3.0$.

Table B.2

The jet shape defined as $\frac{dE_T}{E_T}$ for jets located at $2.5 < |\eta| < 3.0$.

Subcone Radius	45-70	70-105
0.1	.540± .028	.660± .036
0.2	.200± .026	.170± .032
0.3	.110± .018	.070± .027
0.4	.050± .014	.040± .025
0.5	.040± .012	.010± .022
0.6	.020± .010	.020± .019
0.7	.020± .007	.010± .017
0.8	.020± .005	.010± .008
0.9	.010± .003	.005± .006
1.0	.010± .003	.005± .006

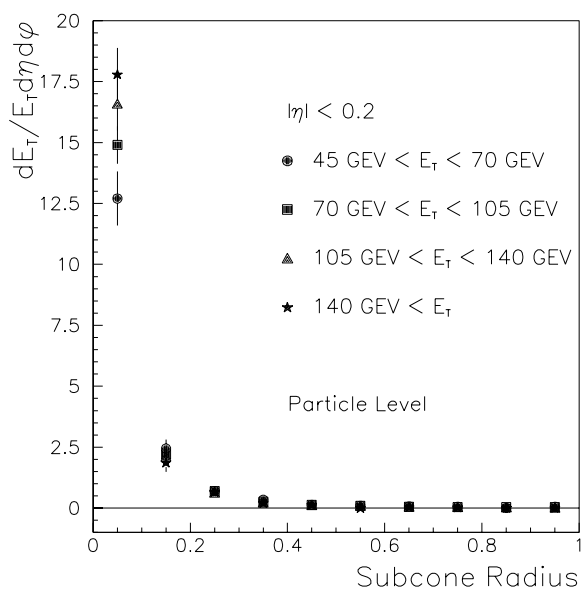

Figure B.3

The jet shape defined as $\frac{1}{E_T}\frac{dE_T}{d\eta d\phi}$ for jets located at $|\eta| < 0.2$.

Table B.3

The jet shape defined as $\frac{1}{E_T}\frac{dE_T}{d\eta d\phi}$ for jets located at $|\eta| < 0.2$.

Subcone Radius	45-70	70-105	105-140	140-
0.1	12.7± 1.11	14.9± .764	16.6± 1.11	17.8± 1.08
0.2	2.44± .372	2.20± .310	2.12± .390	1.87± .382
0.3	0.70± .197	0.70± .134	0.63± .180	0.66± .160
0.4	0.34± .110	0.26± .082	0.23± .100	0.21± .114
0.5	0.14± .074	0.14± .056	0.12± .056	0.13± .046
0.6	0.10± .046	0.09± .034	0.09± .034	0.08± .029
0.7	0.07± .034	0.06± .022	0.05± .022	0.04± .020
0.8	0.05± .027	0.04± .017	0.04± .013	0.03± .015
0.9	0.05± .019	0.04± .008	0.03± .009	0.02± .007
1.0	0.05± .010	0.04± .004	0.02± .005	0.02± .004

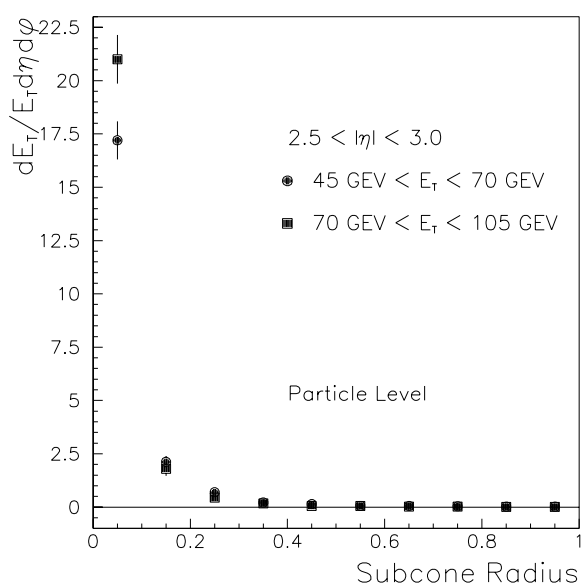

Figure B.4

The jet shape defined as $\frac{1}{E_T}\frac{dE_T}{d\eta d\phi}$ for jets located at $2.5 < |\eta| < 3.0$.

Table B.4

The jet shape defined as $\frac{1}{E_T}\frac{dE_T}{d\eta d\phi}$ for jets located at $2.5 < |\eta| < 3.0$.

Subcone Radius	45-70	70-105
0.1	17.2± .890	21.0± 1.14
0.2	2.12± .270	1.80± .340
0.3	0.70± .110	0.44± .170
0.4	0.22± .060	0.18± .110
0.5	0.14± .042	0.06± .078
0.6	0.06± .028	0.05± .055
0.7	0.05± .017	0.03± .041
0.8	0.04± .010	0.02± .017
0.9	0.02± .005	0.01± .011
1.0	0.02± .004	0.01± .010

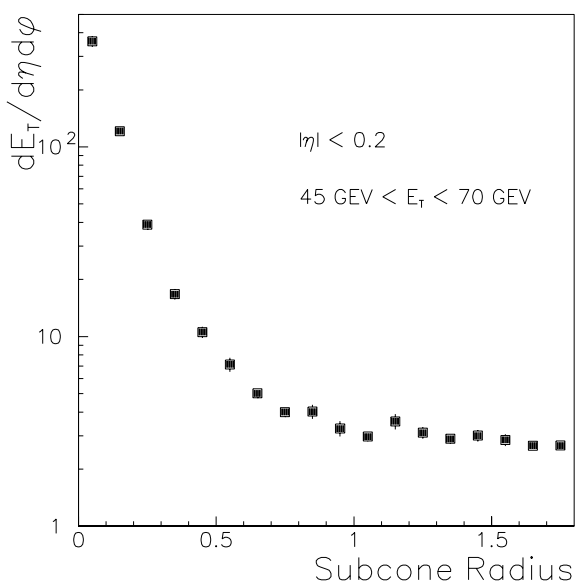

Figure B.5

The jet shape defined as $\frac{dE_T}{d\eta d\phi}$ for jets located at $|\eta| < 0.2$ with transverse energy between 45 and 70 GeV.

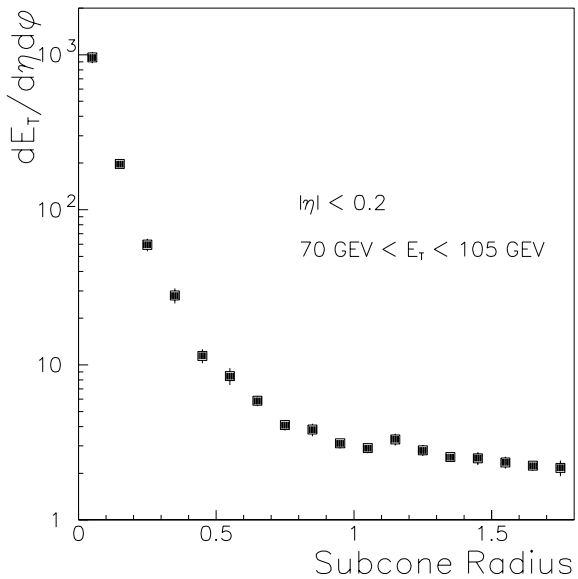

Figure B.6

The jet shape defined as $\frac{dE_T}{d\eta d\phi}$ for jets located at $|\eta| < 0.2$ with transverse energy between 70 and 105 GeV.

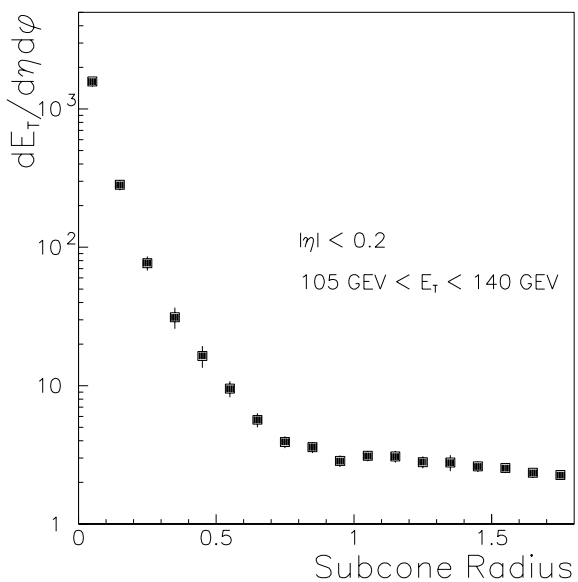

Figure B.7

The jet shape defined as $\frac{dE_T}{d\eta d\phi}$ for jets located at $|\eta| < 0.2$ with transverse energy between 105 and 140 GeV.

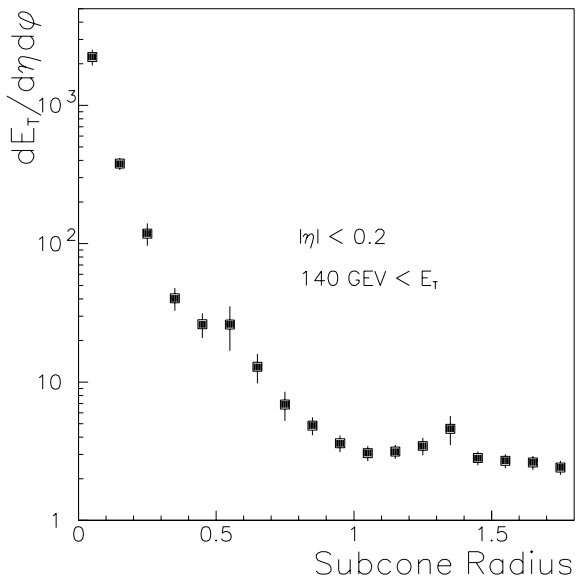

Figure B.8

The jet shape defined as $\frac{dE_T}{d\eta d\phi}$ for jets located at $|\eta| < 0.2$ with transverse energy greater than 140 GeV.

Table B.5

The jet shape defined as $\frac{dE_T}{d\eta d\phi}$ for jets located at $|\eta| < 0.2$.

Subcone Radius	45-70	70-105	105-140	140-
0.1	360± 23	960± 79	1580± 126	2236± 291
0.2	121± 5	197± 11	283± 24	379± 37
0.3	39 ± 2.1	60 ± 5.5	77 ± 8.9	118± 22
0.4	17 ± 1.1	28 ± 3.1	31 ± 5.4	40 ± 7.5
0.5	11 ± .72	11 ± 1.1	16 ± 2.9	26 ± 5.2
0.6	7.1± .61	8.5± 1.1	9.5± 1.2	13 ± 3.1
0.7	5.0± .27	5.9± .44	5.7± .66	6.8± 1.6
0.8	3.9± .21	4.1± .31	3.4± .39	4.8± .71
0.9	4.0± .34	3.8± .35	3.6± .32	3.6± .49
1.0	3.3± .30	3.1± .23	2.9± .27	3.0± .38
1.1	3.3± .36	2.9± .27	3.1± .26	3.1± .36
1.2	3.1± .33	3.3± .29	3.0± .29	3.4± .50
1.3	2.9± .21	2.8± .22	2.8± .28	4.6± 1.1
1.4	3.0± .21	2.5± .17	2.8± .36	2.8± .33
1.5	2.9± .25	2.5± .23	2.8± .21	2.7± .30

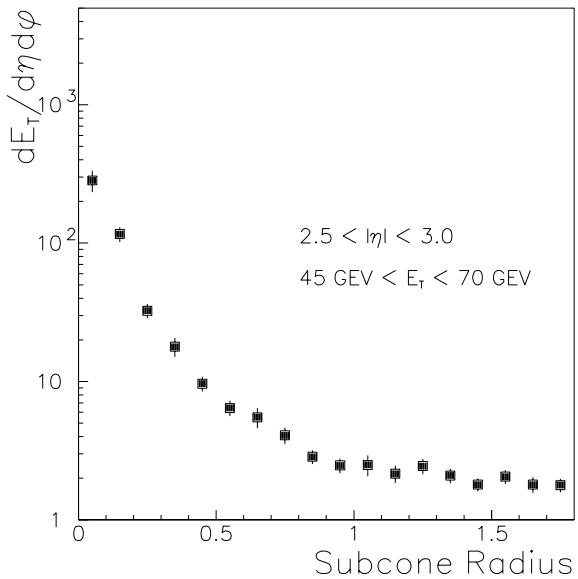

Figure B.9

The jet shape defined as $\frac{dE_T}{d\eta d\phi}$ for jets located at $2.5 < |\eta| < 3.0$ with transverse energy between 45 and 70 GeV.

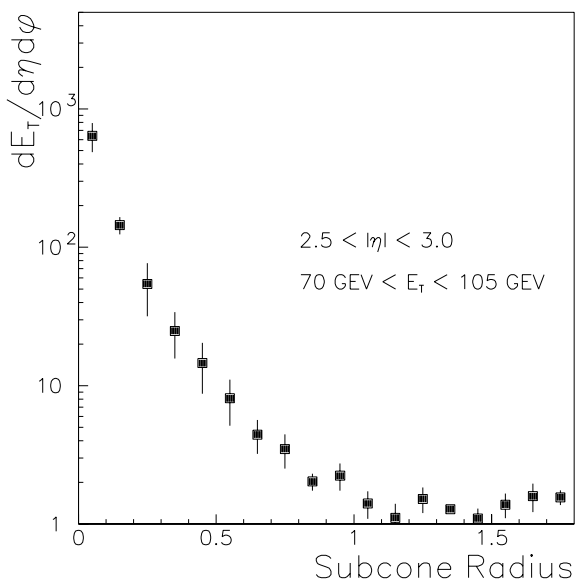

Figure B.10

The jet shape defined as $\frac{dE_T}{d\eta d\phi}$ for jets located at $2.5 < |\eta| < 3.0$ with transverse energy between 70 and 105 GeV.

Table B.6

The jet shape defined as $\frac{dE_T}{d\eta d\phi}$ for jets located at $2.5 < |\eta| < 3.0$.

Subcone Radius	45-70	70-105
0.1	283± 50	639± 152
0.2	116± 14	145± 21
0.3	33± 3.8	54± 23
0.4	18± 2.7	25± 9.1
0.5	9.6± 2.1	15± 5.8
0.6	6.4± .82	8.1± 3.0
0.7	5.5± .92	4.4± 1.2
0.8	4.0± .54	3.5± .97
0.9	2.9± .33	2.0± .28
1.0	2.5± .30	1.2± .49
1.1	2.5± .42	1.4± .32
1.2	2.1± .31	1.1± .29
1.3	2.4± .31	1.5± .32
1.4	2.1± .25	1.2± .31
1.5	2.1± .19	1.1± .27

Appendix C: Merged and Split Jets

The decision parameter used to merge and split jets is not directly related between theory and experiment. However, the merge/split parameters directly affect our measured jet shape. This appendix shows the jet shape for the different merge/split classifications for all of the E_T and η region used in this analysis.

Table C.1

Energy Flow values for different merge/split parameters for jets with transverse energy between 45 and 70 GeV located at $|\eta| < 0.2$. Errors are statistical only.

Subcone Radius	Not Merged or Split	Only Merged	Only Split	All
0.1	.41± .006	.27± .012	.41± .008	.40± .004
0.2	.66± .006	.45± .018	.66± .008	.63± .004
0.3	.77± .005	.57± .018	.76± .007	.75± .004
0.4	.84± .004	.66± .016	.84± .005	.82± .003
0.5	.88± .003	.74± .013	.88± .004	.86± .002
0.6	.91± .002	.80± .010	.91± .003	.90± .002
0.7	.94± .002	.86± .006	.93± .002	.93± .001
0.8	.95± .001	.90± .005	.96± .001	.95± .001
0.9	.98± .001	.94± .003	.98± .001	.97± .001
1.0	1.0± 0.0	1.0± 0.0	1.0± 0.0	1.0± 0.0

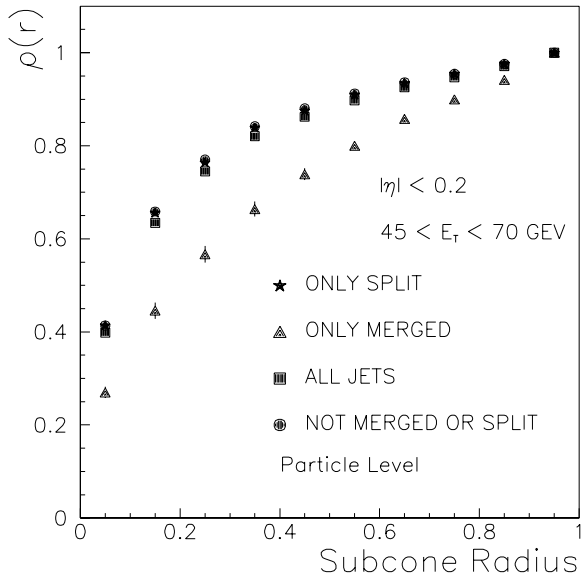

Figure C.1

The jet shape for different merge/split parameters for jets with transverse energy between 45 and 70 GeV located at $|\eta| < 0.2$. Errors are statistical only.

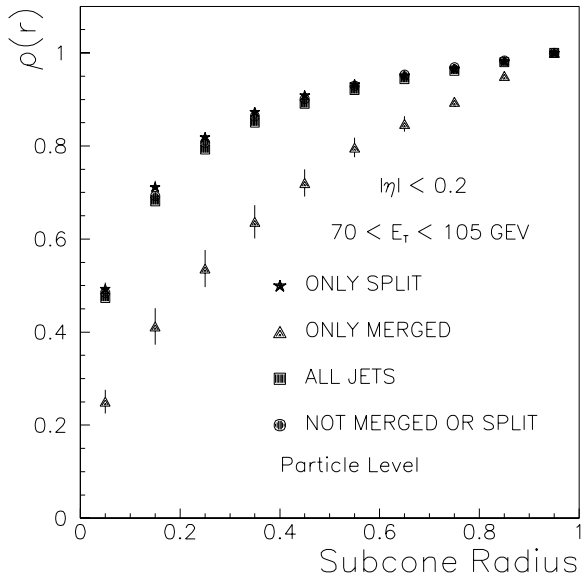

Figure C.2

The jet shape for different merge/split parameters for jets with transverse energy between 70 and 105 GeV located at $|\eta| < 0.2$. Errors are statistical only.

Table C.2

Energy Flow values for different merge/split parameters for jets with transverse energy between 70 and 105 GeV located at $|\eta| < 0.2$. Errors are statistical only.

Subcone Radius	Not Merged or Split	Only Merged	Only Split	All
0.1	.48± .010	.25± .026	.49± .013	.47± .008
0.2	.69± .010	.41± .039	.71± .012	.68± .008
0.3	.81± .007	.54± .039	.82± .010	.79± .006
0.4	.86± .005	.64± .036	.87± .007	.85± .005
0.5	.90± .004	.72± .019	.91± .005	.89± .004
0.6	.93± .003	.80± .017	.93± .003	.92± .003
0.7	.95± .002	.85± .016	.95± .002	.94± .002
0.8	.97± .001	.89± .010	.97± .001	.96± .001
0.9	.98± .001	.95± .005	.98± .001	.98± .001
1.0	1.0± 0.0	1.0± 0.0	1.0± 0.0	1.0± 0.0

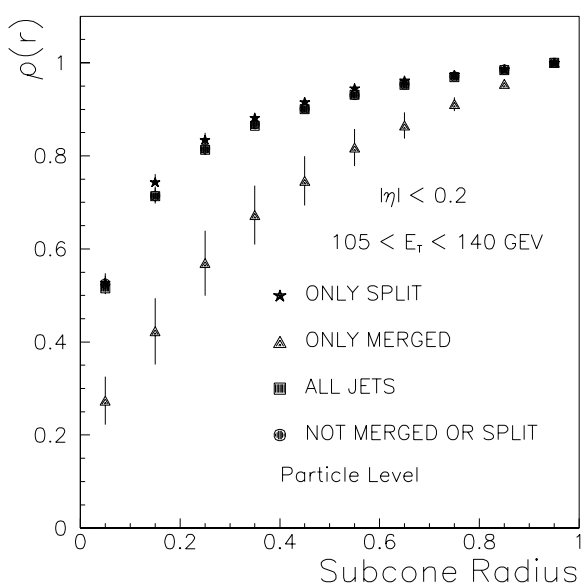

Figure C.3

The jet shape for different merge/split parameters for jets with transverse energy between 105 and 140 GeV located at $|\eta| < 0.2$. Errors are statistical only.

Table C.3

Energy Flow values for different merge/split parameters for jets with transverse energy between 105 and 140 GeV located at $|\eta| < 0.2$. Errors are statistical only.

Subcone Radius	Not Merged or Split	Only Merged	Only Split	All
0.1	.53± .017	.27± .051	.53± .019	.52± .012
0.2	.71± .017	.42± .071	.74± .018	.71± .012
0.3	.82± .013	.57± .069	.83± .014	.81± .010
0.4	.87± .010	.67± .063	.88± .011	.86± .008
0.5	.90± .007	.75± .052	.92± .008	.90± .006
0.6	.93± .005	.82± .039	.95± .006	.93± .004
0.7	.95± .003	.87± .028	.96± .004	.95± .003
0.8	.97± .002	.91± .015	.97± .003	.97± .002
0.9	.99± .001	.95± .007	.99± .001	.98± .001
1.0	1.0± 0.0	1.0± 0.0	1.0± 0.0	1.0± 0.0

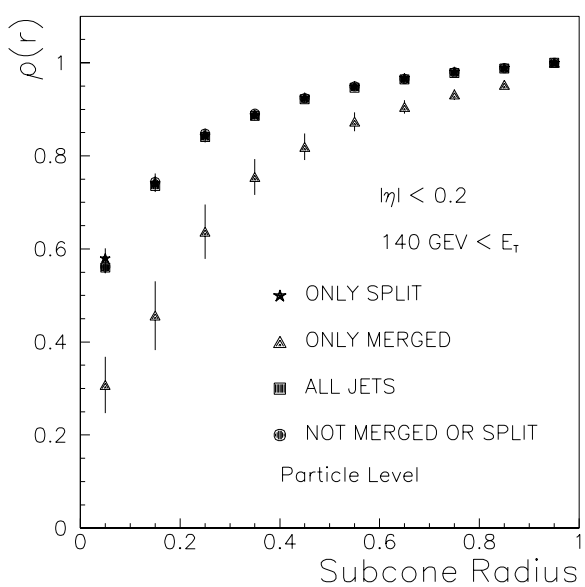

Figure C.4

The jet shape for different merge/split parameters for jets with transverse energy greater than 140 located at $|\eta| < 0.2$. Errors are statistical only.

Table C.4

Energy Flow values for different merge/split parameters for jets with transverse energy greater than 140 GeV located at $|\eta| < 0.2$. Errors are statistical only.

Subcone Radius	Not Merged or Split	Only Merged	Only Split	All
0.1	.56± .014	.31± .061	.58± .020	.56± .020
0.2	.74± .013	.46± .074	.74± .019	.74± .019
0.3	.85± .009	.64± .059	.84± .015	.84± .015
0.4	.89± .006	.75± .039	.89± .012	.89± .012
0.5	.92± .005	.82± .029	.93± .009	.93± .009
0.6	.95± .003	.87± .020	.95± .006	.95± .006
0.7	.97± .002	.91± .014	.97± .003	.97± .003
0.8	.98± .001	.93± .011	.98± .001	.98± .001
0.9	.99± .001	.95± .007	.99± .001	.99± .001
1.0	1.0± 0.0	1.0± 0.0	1.0± 0.0	1.0± 0.0

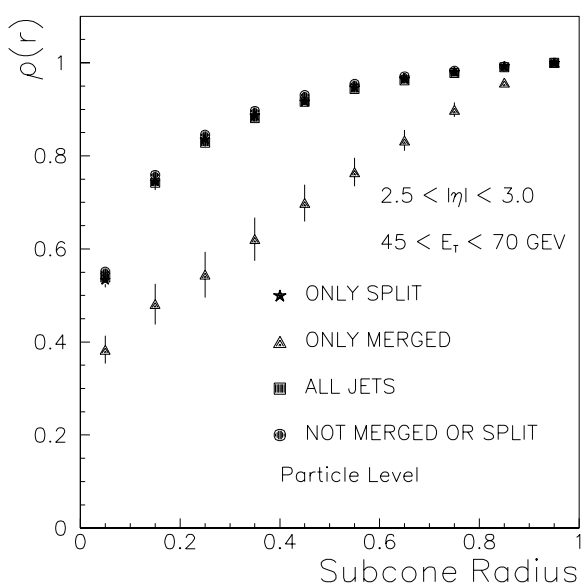

Figure C.5

The jet shape for different merge/split parameters for jets with transverse energy between 45 and 70 GeV located at $2.5 < |\eta| < 3.0$. Errors are statistical only.

Table C.5

Energy Flow values for different merge/split parameters for jets with transverse energy between 45 and 70 GeV located at $2.5 < |\eta| < 3.0$. Errors are statistical only.

Subcone Radius	Not Merged or Split	Only Merged	Only Split	All
0.1	.55± .007	.38± .029	.53± .016	.54± .007
0.2	.76± .009	.48± .044	.75± .019	.74± .008
0.3	.85± .008	.54± .049	.84± .016	.83± .007
0.4	.90± .006	.62± .046	.89± .012	.88± .006
0.5	.93± .004	.70± .039	.92± .010	.92± .004
0.6	.95± .003	.77± .031	.95± .007	.94± .003
0.7	.97± .002	.83± .022	.97± .005	.96± .002
0.8	.98± .001	.90± .016	.98± .003	.98± .001
0.9	.99± .001	.96± .006	.99± .001	.99± .001
1.0	1.0± 0.0	1.0± 0.0	1.0± 0.0	1.0± 0.0

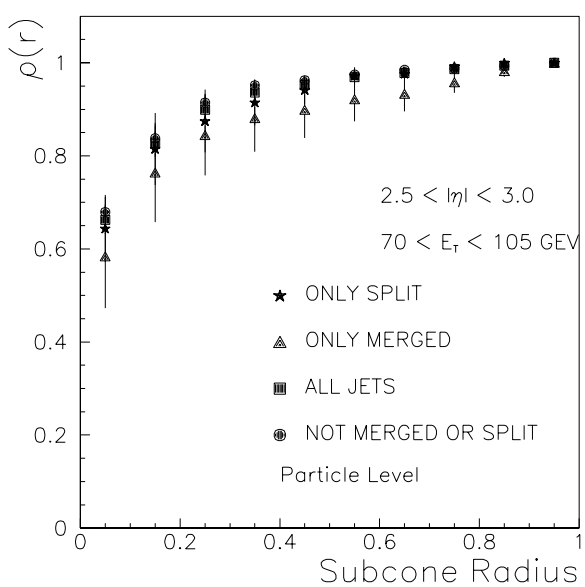

Figure C.6

The jet shape for different merge/split parameters for jets with transverse energy between 70 and 105 GeV located at $2.5 < |\eta| < 3.0$. Errors are statistical only.

Table C.6

Energy Flow values for different merge/split parameters for jets with transverse energy between 70 and 105 GeV located at $2.5 < |\eta| < 3.0$. Errors are statistical only.

Subcone Radius	Not Merged or Split	Only Merged	Only Split	All
0.1	.68± .033	.58± .111	.64± .072	.66± .029
0.2	.84± .028	.76± .106	.81± .077	.83± .028
0.3	.91± .019	.84± .086	.87± .067	.90± .022
0.4	.95± .012	.88± .073	.91± .049	.94± .026
0.5	.96± .009	.90± .060	.94± .031	.95± .011
0.6	.97± .007	.92± .047	.97± .018	.97± .007
0.7	.98± .005	.93± .038	.98± .011	.98± .006
0.8	.99± .003	.96± .023	.99± .005	.99± .003
0.9	.99± .001	.98± .012	.99± .002	.99± .002
1.0	1.0± 0.0	1.0± 0.0	1.0± 0.0	1.0± 0.0

Appendix D: Leading and Non-Leading Jets

This appendix shows the jet shape for leading jets and non-leading jets separately for all of the E_T and η regions studied.

Table D.1

The jet shape for leading and non-leading jets for jets located at $\eta < 0.2$ with transverse energy between 45 and 70 GeV. Errors are statistical only.

Subcone Radius	Leading Jets $< E_T >$=62 GeV	Non-Leading Jets $< E_T >$=56 GeV
0.1	.45± .007	.36± .006
0.2	.69± .007	.59± .007
0.3	.79± .005	.71± .006
0.4	.86± .004	.79± .005
0.5	.89± .003	.84± .004
0.6	.92± .002	.88± .003
0.7	.94± .002	.91± .003
0.8	.96± .001	.94± .002
0.9	.98± .001	.97± .001
1.0	1.0± 0.0	1.0± 0.0

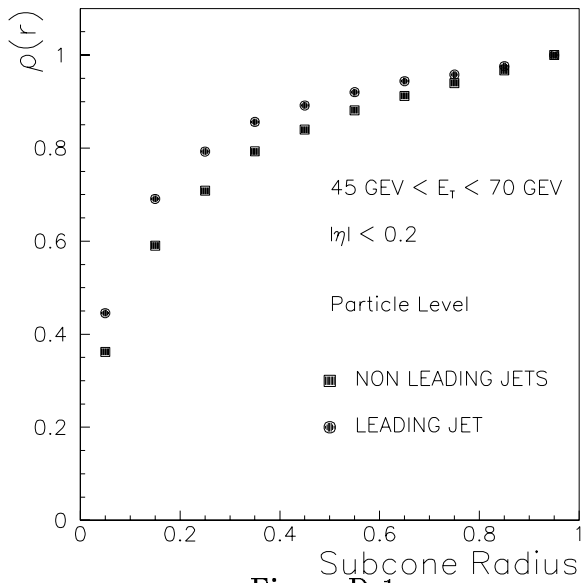

Figure D.1

The jet shape for leading and non-leading jets for jets located at $\eta < 0.2$ with transverse energy between 45 and 70 GeV. Errors are statistical only.

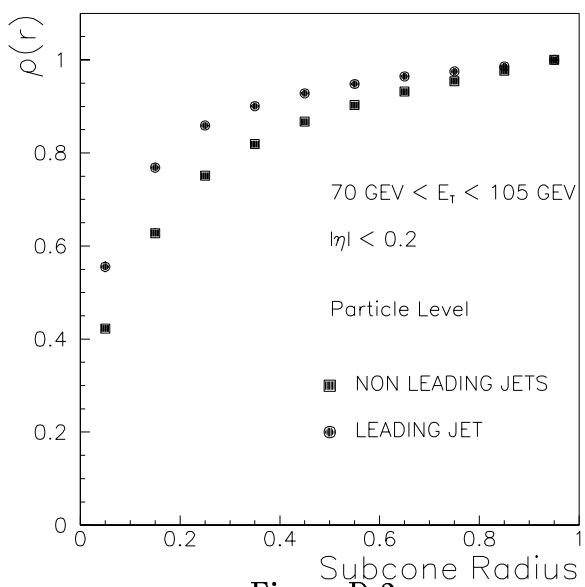

Figure D.2

The jet shape for leading and non-leading jets for jets located at $\eta < 0.2$ with transverse energy between 70 and 105 GeV. Errors are statistical only.

Table D.2

The jet shape for leading and non-leading jets for jets located at $\eta < 0.2$ with transverse energy between 70 and 105 GeV. Errors are statistical only.

Subcone Radius	Leading Jets $< E_T >$=96 GeV	Non-Leading Jets $< E_T >$=87 GeV
0.1	.56± .012	.42± .006
0.2	.77± .011	.63± .007
0.3	.86± .008	.75± .006
0.4	.90± .006	.82± .005
0.5	.93± .004	.87± .004
0.6	.95± .003	.90± .003
0.7	.96± .002	.93± .003
0.8	.98± .001	.95± .002
0.9	.99± .001	.98± .001
1.0	1.0± 0.0	1.0± 0.0

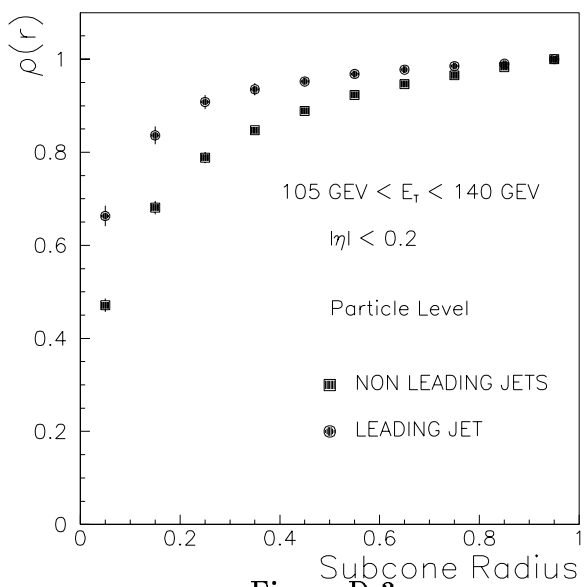

Figure D.3

The jet shape for leading and non-leading jets for jets located at $\eta < 0.2$ with transverse energy between 105 and 140 GeV. Errors are statistical only.

Table D.3

The jet shape for leading and non-leading jets for jets located at $\eta < 0.2$ with transverse energy between 105 and 140 GeV. Errors are statistical only.

Subcone Radius	Leading Jets $< E_T >$=136 GeV	Non-Leading Jets $< E_T >$=125 GeV
0.1	.66± .022	.47± .014
0.2	.84± .019	.68± .014
0.3	.91± .015	.79± .012
0.4	.94± .013	.85± .009
0.5	.95± .010	.89± .007
0.6	.97± .009	.92± .005
0.7	.98± .008	.95± .004
0.8	.99± .004	.97± .002
0.9	.99± .002	.98± .001
1.0	1.0± 0.0	1.0± 0.0

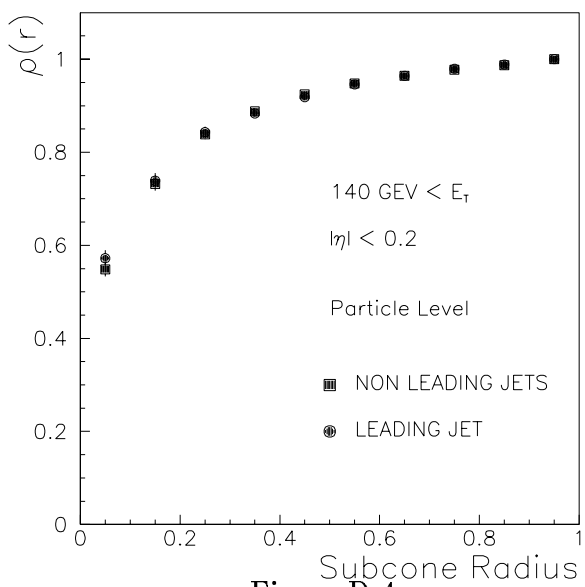

Figure D.4

The jet shape for leading and non-leading jets for jets located at $\eta < 0.2$ with transverse energy greater than 140 GeV. Errors are statistical only.

Table D.4

The jet shape for leading and non-leading jets for jets located at $\eta < 0.2$ with transverse energy greater than 140 GeV. Errors are statistical only.

Subcone Radius	Leading Jets $< E_T >$=205 GeV	Non-Leading Jets $< E_T >$=184 GeV
0.1	.58± .017	.55± .015
0.2	.74± .016	.73± .014
0.3	.84± .012	.84± .010
0.4	.88± .010	.89± .007
0.5	.92± .008	.92± .005
0.6	.95± .005	.95± .004
0.7	.96± .003	.96± .003
0.8	.98± .002	.98± .002
0.9	.99± .001	.99± .001
1.0	1.0± 0.0	1.0± 0.0

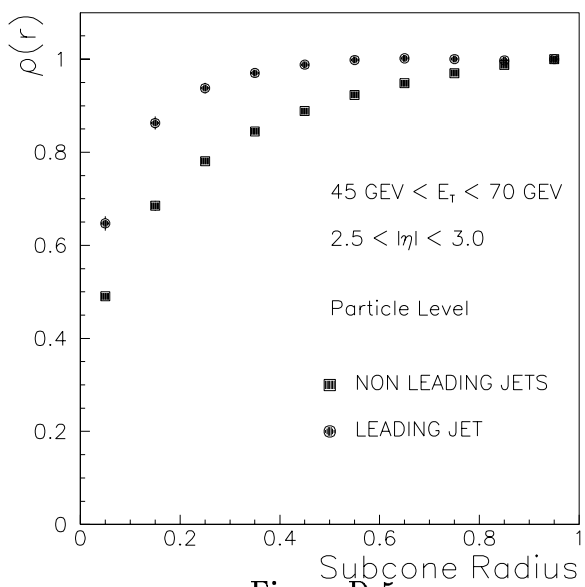

Figure D.5

The jet shape for leading and non-leading jets for jets located at $2.5 < \eta < 3.0$ with transverse energy between 45 and 70 GeV. Errors are statistical only.

Table D.5

The jet shape for leading and non-leading jets for jets located at $2.5 < \eta < 3.0$ with transverse energy between 45 and 70 GeV. Errors are statistical only.

Subcone Radius	Leading Jets $< E_T >$=66 GeV	Non-Leading Jets $< E_T >$=58 GeV
0.1	.65± .016	.49± .010
0.2	.86± .014	.68± .010
0.3	.94± .011	.78± .010
0.4	.97± .008	.84± .008
0.5	.99± .005	.89± .006
0.6	.99± .004	.92± .005
0.7	1.0± .003	.95± .003
0.8	1.0± .002	.97± .002
0.9	1.0± .001	.99± .001
1.0	1.0± 0.0	1.0± 0.0

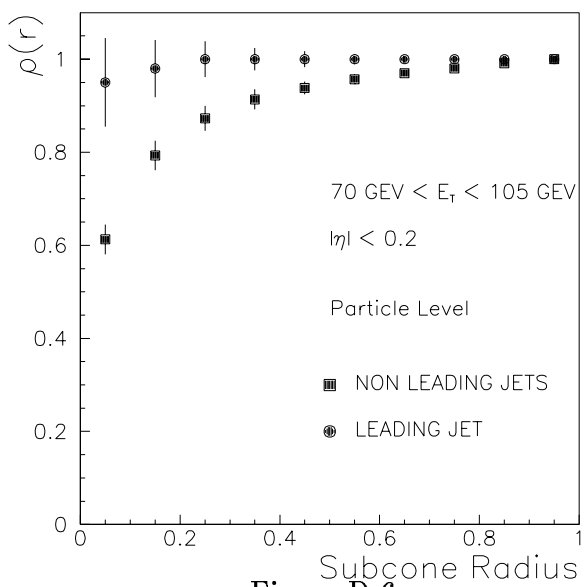

Figure D.6

The jet shape for leading and non-leading jets for jets located at $2.5 < \eta < 3.0$ with transverse energy between 70 and 105 GeV. Errors are statistical only.

Table D.6

The jet shape for leading and non-leading jets for jets located at $2.5 < \eta < 3.0$ with transverse energy between 70 and 105 GeV. Errors are statistical only. (Note only two jets comprise the leading jet measurement.)

Subcone Radius	Leading Jets $< E_T >$=100 GeV	Non-Leading Jets $< E_T >$=85 GeV
0.1	.95± .095	.61± .010
0.2	.98± .061	.79± .010
0.3	1.0± .039	.87± .010
0.4	1.0± .024	.91± .008
0.5	1.0± .017	.94± .006
0.6	1.0± .011	.96± .005
0.7	1.0± .009	.97± .003
0.8	1.0± .005	.98± .002
0.9	1.0± .003	.99± .001
1.0	1.0± 0.0	1.0± 0.0

VITA

VITA

Braden K. Abbott was born in Morris, Mn on March 16, 1967. He grew up in Morris where he attended public school. He enrolled as an undergraduate at the University of Minnesota, Morris in 1985, where he majored in physics and mathematics. He was accepted into the graduate physics program at Purdue University in 1989, where he pursued research in High Energy Physics. Under the direction of Dr. David Koltick, he received the Doctor of Philosophy degree in 1994.